Effect on flow conditions of floating debris accumulation at bridges

Auteur : Dütz, Florence
Promoteur(s) : Erpicum, Sebastien; Pirotton, Michel
Faculté : Faculté des Sciences appliquées
Diplôme : Master en ingénieur civil des constructions, à finalité spécialisée en "civil engineering"
Année académique : 2022-2023
URI/URL : http://hdl.handle.net/2268.2/17400

Université de Liège - Faculté des Sciences Appliquées

Effect on flow conditions of floating debris accumulation at bridges

Master thesis for the degree of Civil Engineering by

DÜTZ Florence

Supervisors:
Erpicum, Sébastien
Pirotton, Michel

Jury members:
Andrianne, Thomas
Englebert, Benjamin

Academic year 2022-2023

Remerciements

Je voudrais tout d'abord remercier mon promoteur M. Sébastien Erpicum de m'avoir permis de d'inclure une composante expérimentale au sein du laboratoire d'hydraulique dans mon travail. Ses conseils et suggestions m'ont permis de pousser ce mémoire plus loin que ce que je ne l'imaginais. Je le remercie également de m'avoir permis de participer aux réunions et d'interagir avec les partenaires du projet EMfloodResilience.

Je voudrais également remercier les membres de mon jury pour le temps qu'ils ont consacré à la lecture et à l'évaluation de ce travail.

Ensuite, un grand merci à Loïc Benet pour son aide tout au long de mon travail ainsi que ses précieux conseils au labo.
Je remercie également les techniciens du laboratoire d'hydraulique (Grégory Thonard et Maxime Mathieu) pour tout le support technique qu'ils m'ont apporté et pour leurs encouragements.

Merci à mes relecteurs, Antoine C., Antoine d. et Antoine M. .

Enfin, un merci tout particulier à ma Maman, pour ses relectures, ses conseils et son soutien sans faille durant toutes mes études, à mon Papa, ma sœur et Romin pour leur présence, leur écoute et leurs encouragements pendant cette période intense. Pour finir, merci à Salto et Lola pour m'avoir tenu compagnie pendant chaque blocus depuis 5 ans.

Summary

This work is related to the EMfloodResilience project of the Interreg Euregio Meuse-Rhine project. The main goal is to study the effect of flow conditions on the consequences of floating debris accumulation at bridges.

Therefore, an experimental campaign was carried out in the Engineering Hydraulics Laboratory of the University of Liège. Two bridge geometries are investigated as well as two different mixtures of debris and 10 flow conditions characterized by an initial water depth h_0 and an initial Froude number Fr_0.

The observed accumulation formation process are in agreement with those described in the literature (Schmocker and Hager, 2013). The accumulation process takes place in 2 phases. The initial debris accumulation during which the debris accumulate vertically along the pier(s) and the formation of a debris carpet, during which floating debris accumulates horizontally on the surface.

The experiments have shown that water depth increases with the volume of debris accumulated at the bridge. Once a certain volume of debris is reached, the water depth barely rises at all.

The number of bridge piers does not have a big impact on the flow conditions nor on the debris accumulation. Indeed, although a two pier bridge causes a longer accumulation than a one pier bridge, the effect on the backwater rise could not be distinguished between the two geometries. As for the debris composition, it has a significant impact on the accumulation formation and the backwater rise. The initial Froude number Fr_0 of the flow has a significant effect on both the accumulation structure and the flow conditions. The larger the Froude number, the shorter the accumulation. As a result, the accumulation is more compact and blocks more water, leading to a greater backwater rise.

The relative carpet length and the relative flow depth at the end of the test are linked to the Froude number with some fit equations The effect of Froude number on accumulation length differs according to initial water depth and debris mixtures, whereas the effect of Froude on water height depends very little on debris composition (if at all). The influence of the initial water depth depends on the position of the bridge deck in relation to the water surface. For a h_0 under the deck, it could be concluded that the higher water depth generated higher backwater rise.

The evolution of water depth as a function of accumulation volume can be approximated by a power law. To obtain a law that does not depend on scale, the normalization proposed by Schalko et al., 2019a (21) was adapted to the present case. From this law, a characteristic volume, responsible for the primary backwater rise, can be deduced. For each Froude, bridge geometry and debris composition, a characteristic volume was determined independently of the water level.

Résumé

Ce travail est lié au projet EMfloodResilience financé par Interreg Euregio Meuse-Rhin. L'objectif principal est d'étudier l'effet des conditions d'écoulement sur les conséquences d'accumulation de débris flottants au droit des ponts.

Une campagne expérimentale a donc été menée dans le laboratoire d'ingénierie hydraulique de l'Université de Liège. Deux géométries de ponts sont étudiées ainsi que deux mélanges différents de débris et 10 conditions d'écoulement caractérisées par une profondeur d'eau initiale h_0 et un nombre de Froude initial Fr_0.

Les processus de formation d'accumulation observés sont en accord avec ceux décrits dans la littérature (Schmocker and Hager, 2013). Le processus d'accumulation se déroule en 2 phases. L'accumulation initiale des débris durant laquelle les débris s'accumulent verticalement le long de la (des) pile(s) et la formation d'un tapis de débris, au cours de laquelle les débris flottants s'accumulent horizontalement à la surface.

Les expériences ont montré que la hauteur d'eau augmente avec le volume de débris accumulés au droit du pont. À partir d'un certain volume de débris, la hauteur de l'eau n'augmente presque plus.

Le nombre de piliers du pont n'a pas un grand impact sur les conditions d'écoulement ni sur l'accumulation de débris. En effet, bien qu'un pont à deux piles provoque une accumulation plus longue qu'un pont à une seule pile, l'effet sur la hauteur d'eau n'a pas pu être distingué entre les deux géométries. Quant à la composition des débris, elle a un impact significatif sur la formation de l'accumulation et l'augmentation du niveau d'eau. Le nombre de Froude initial Fr_0 de l'écoulement a un effet significatif à la fois sur la structure de l'accumulation et sur l'augmentation du niveau d'eau. Plus le nombre de Froude est grand, plus l'accumulation est courte. Par conséquent, l'accumulation est plus compacte et bloque plus d'eau, ce qui entraîne une plus grande augmentation du niveau d'eau.

La longueur relative du tapis et la profondeur relative de l'écoulement à la fin de l'essai ont été liées au nombre de Froude par des équations d'ajustement. L'effet du nombre de Froude sur la longueur de l'accumulation diffère en fonction de la hauteur initiale de l'eau et la composition des débris, alors que l'effet du nombre de Froude sur la hauteur d'eau dépend très peu de la composition des débris (voire pas du tout). L'influence de la hauteur d'eau initiale dépend de la position du tablier du pont par rapport à la surface de l'écoulement. Pour un h_0 sous le tablier, on peut conclure que plus la hauteur d'eau est élevée, plus l'augmentation du niveau d'eau est importante.

L'évolution de la profondeur d'eau en fonction du volume d'accumulation peut être approximée par une loi en puissance. Pour obtenir une loi qui ne dépend pas de l'échelle, la normalisation proposée par Schalko et al., 2019a a été adaptée au cas présent. À partir de cette loi, un volume caractéristique, responsable de l'élévation primaire du niveau d'eau, peut être déduit. Pour chaque Froude, chaque géométrie du pont et chaque composition de débris, un volume caractéristique a été déterminé indépendamment du niveau d'eau.

Contents

Part I
Introduction

1 Literature review

1.1 Drifts in rivers

Drifts are defined as "any type of wood floating in a river". They fall in rivers as a result of bank erosion or climatic event (Schmocker and Hager, 2011). During flood events, the amount of drifts in the river is very abundant because the water reaches wood on the riverbanks it doesn't usually reach and because the driving power of the flow increases.

The transport of wood during a flood event has been studied in mountain rivers (Ruiz-Villanueva et al., 2016) and in other rivers (Davidson et al., 2015). In particular, this research studied the effect of the dimensions of the drifts and the characteristics of the flow.

These drifts are likely to accumulate at natural obstacles such as rocks, meanders, or narrow and shallow sections (Schmocker and Hager, 2011). Anthropogenic obstacles, such as bridge piers, weirs, or retention racks, can also cause blockage.

The probability of blockage for individual drifts has been studied for bridge deck (Schmocker and Hager, 2011), bridge pier (Schalko et al., 2020), and for the combination of both of them (Gschnitzer et al., 2014).

Schmocker and Hager, 2011 and Schalko et al., 2020 each derived equations to characterize the probability of blockage, with variations based on the specific types of blocking structures investigated in their respective studies.

Schmocker & Hager probability equations (eq.1, 2 and 3) describe the probability of drift blockage at bridge decks. They distinguish logs (approximately cylindrical pieces of wood) from rootstocks (tree stumps with several roots) (see fig. 1). In this document, only the equations for logs are presented.

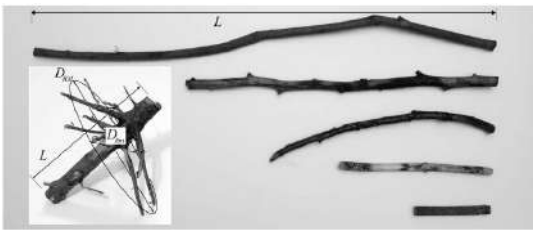

Figure 1: Schmocker and Hager, 2011, fig. 4, Examples of logs and rootstock used, notations: L is the length of the logs or the rootstock and D_R is the external diameter of the rootstock.

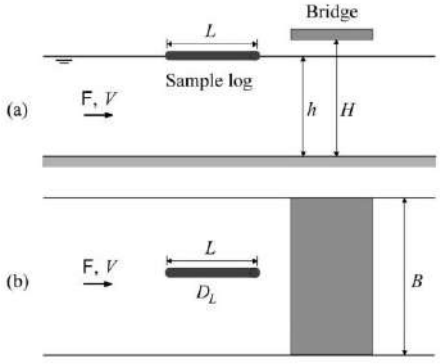

Figure 2: Schmocker and Hager, 2011, fig. 3, Sketch of experimental setup with log drifts: (a) side view; (b) plan, notations: L and D_L are the length and the diameter of the logs, F and V are the Froude number and the velocity of the flow, h is the water depth and H is the height of the bridge from the river bottom, B is the width of the flume.

They include the influence of the drifts dimensions with a log parameter (λ, eq. 1), the flow characteristics (F and h), the freeboard ($H - h$) and the bridge's characteristics. Four bridge types were investigated, namely a reference bridge consisting only of the bridge roadway, a truss bridge, a railing bridge and a baffle bridge (see fig. 3) (Schmocker and Hager, 2011).

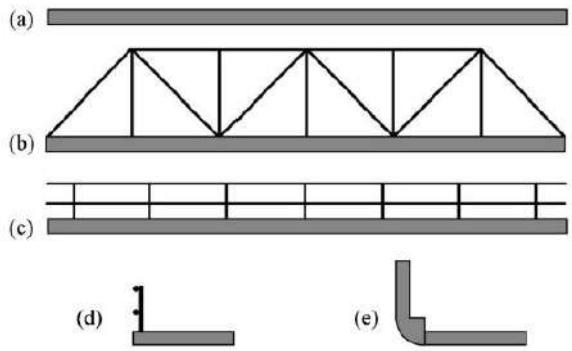

Figure 3: Schmocker and Hager, 2011, fig. 2, Investigated bridge types: Frontal view of (a) reference bridge; (b) truss bridge; (c) railing bridge; and cross-sections of (d) railing bridge and (e) baffle bridge.

Schmocker & Hager probability equations are the followings:

$$\lambda = L/B[h + D_L/2)]/H(\text{Log parameter}) \tag{1}$$

For logs, the fitted equation for blockage probability, P_L, depends on the bridge type:

$$P_L/P_{LM} = -0.074 + 0.88\lambda \quad \text{for reference, railing, and truss bridges} \tag{2a}$$
$$P_L/P_{LM} = -0.21 + 0.81(L/B) \quad \text{for baffle bridges} \tag{2b}$$

where P_{LM} is the maximum blockage probability which depends on the ratio between the water and the bridge heights, h/H:

$$P_{LM} = 0 \quad \text{for } h/H \leq 0.90 \tag{3a}$$
$$P_{LM} = 0.25z + (4 - z)(F - 0.8)^2 \quad \text{for } h/H = 1 \tag{3b}$$
$$P_{LM} = 1 - z(F - 0.3)^2 \quad \text{for } h/H = 1.07 \tag{3c}$$

in which $z = 2$ and 1 for the reference, truss, and railing bridge types in eq. 3 and $z = 0$ and 2.5 for the baffle bridge type, respectively, in eq. 3.

Gschnitzer et al., 2014 conduct similar tests as Schmocker and Hager, 2011. They studied the impact of a single pier on the probability of clogging for a predetermined deck design. Additionally, they investigated how the channel slope, the Froude number, the depth of the flow, and the presence of branches on logs affect the clogging probability.

The investigated water depths were similar to the ones investigated by Schmocker and Hager, 2011. Indeed, keeping the notations h/H where h is the water depth and H the bridge height, the water depth tested have the ratio $h/H = 1$, $h/H = 1.125$ and $h/H = 1.25$.

Gschnitzer et al., 2014 confirmed that higher water depths are associated to higher clogging probabilities. Similarly, logs with branches resulted in higher probabilities of clogging compared to those without branches. As for the channel slope, the results depend on the water depth. For a ratio $h/H = 1$, the clogging probability decreases for increasing slope. On the contrary, for ratios of $h/H = 1.125$ and $h/H = 1.25$, the clogging probability increases for increasing slope.

According to Schmocker and Hager, 2011, the higher the Froude number, the lower the clogging probability when $h/H = 1.07$. This could not be reproduced by Gschnitzer et al., 2014. Generally speaking, the clogging probability observed by Gschnitzer et al., 2014 were lower than the ones of Schmocker and Hager, 2011. One explanation is the presence of the pile that could affect the log parameter (eq. 1).

Probability equations proposed by Schalko et al., 2020 (eq. 4) describe the probability of drift blockage at bridge piers.

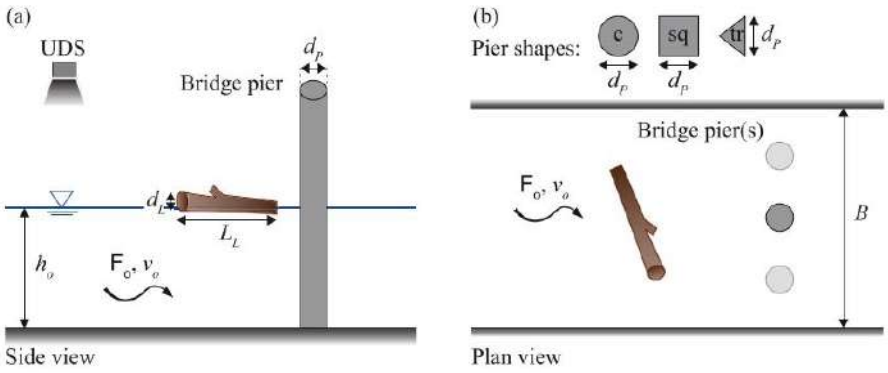

Figure 4: Schalko et al., 2020, fig. 5, Experimental set-up with notation of model tests on LW accumulation probability with (a) side and (b) plan view;
notations: L_L and d_L are the length and the diameter of the logs, F_0 and v_0 are the initial Froude number and velocity of the flow, h_0 is the initial water depth, B is the width of the flume and d_P is the bridge pier diameter or maximum width of pier, c = circular, sq = square, tr = triangular bridge pier.

They include the log length (L_L) and diameter (d_L) as well as their characteristics (presence of branches or not, wood density), the flow characteristics (v_0) and the number and the geometry of the piers (d_p). They also introduce a parameter,x_n, related to the congestion degree of the drift transport. An uncongested Large Wood (LW) transport signifies that the logs occupy less than 10% of the channel area and move without interactions with one another. In congested transport, the logs occupy more than 33 % of the channel area and move together as a single mass. Semi-congested transport is intermediate between these two transport regimes (Braudrick et al., 1997). $x_n = 1.00$ for uncongested LW transport and $x_n = 0.65$ for semi-congested and continuous LW transport (Schalko et al., 2020).

The blockage probability, p, is given by the equation:

$$p = e^{-12.7LW_p} \tag{4a}$$

$$\text{where } LW_p = x_n \left(\frac{v_0^2}{2gL_L}\right)^{0.43} \left(\frac{d_p}{L_L}\right)^{0.60} \tag{4b}$$

is the normalized Large wood accumulation probability parameter.

Field study were conduct to confirm these experimental studies and results (Wyss et al., 2021). Wyss reproduced Schalko's experiment in a natural river for one circular bridge pier. They observed no scale effect and a good applicability of Schalko's equation.

From this study, it could be concluded that the accumulation process of a single log is divided in 3 phases:

1. The impact with the pier
2. The rotation around the pier
3. The separation from the pier

The shape of the log and its orientation at the impact influence the duration of these phases (Wyss et al., 2021).

A synthesis of the contents and results from the different previously cited references (Schmocker and Hager, 2011, Gschnitzer et al., 2014, Schalko et al., 2020 and Wyss et al., 2021) is presented in the table 1.

Table 1: Comparison of the different studies about blockage probability of logs at bridges infrastructures.

Autors Year	Study type	Study object	Studied parameters	Formula?	Parameter influencing the probability	Blockage structure	Observations
Schmocker & Hager 2011	Exp.	Blockage probability	Initial flow conditions (F) Freeboard Drift dimensions and shape Bridge deck type	yes	Drift dimension Froude number Freeboard Deck type	Bridge deck	
Gschnitzer et al. 2014	Exp.	Blockage probability	Initial flow conditions (F0,h0) Channel slope Logs dimensions and shape Bridge geometry	no	Froude number Channel slope Water level	Bridge piers Bridge deck	Clogging probability tend to be lower than the predicted formula (Schmocker & Hager) 2011
Schalko et al. 2020	Exp.	Blockage probability	Initial flow conditions Logs dimensions and shape Transport type Pier shape and number Scour	yes	Initial flow velocity Logs dimensions Transport type Pier shape and number	Bridge piers	
Wyss et al. 2021	Field	Validation of Schalko's probability equations	Scale effect	no	/	Circular bridge piers	no scale effect, good applicability of Schalko's equation The log orientation at the impact point influence whether a log remains accumulated or separates from the pier

1.2 Large Wood Accumulation

When one drift get stuck, the free cross-section of the river decreases, which increases the probability of other woods to get blocked as well. More and more wood accumulates and what is called a Large Wood accumulation or jam is created. Large woods (LW) are defined as logs with length $< 1m$ and diameter $> 0.10m$ (Keller and Swanson, 1979). These accumulations modify the initial flow conditions by increasing the water level and decreasing the flow velocity. The increment of water level upstream of the bridge is called backwater rise.

LW accumulations and their effects were studied at different river infrastructures like retention racks (Schmocker and Hager, 2013, Schalko et al., 2018, Schalko et al., 2019a, Schalko et al., 2019b and Follett et al., 2020), or slit-check dams (fig. 5b)(Wang et al., 2022).

Retention racks (fig. 5a) are screens that are placed upstream of turbines or pumps to prevent debris from blocking the pumps or turbines. Slit-check dams (fig. 5b) are dams with an opening used in debris flow hazard mitigation to reduce the energy level of a debris flow and the total transported volume and to stop the largest stones during the debris flow process.

(a) Schalko, 2020, fig.1(a), Wood retention racks in Switzerland in River Chiene.

(b) Wang et al., 2022, fig.1(c), Slit-check dam in channel.

Figure 5: Studied river infrastructures.

Follet and Schalko studies focus on the effect of predefined accumulation between 2 racks (fig. 6) (Schalko et al., 2018, Follett et al., 2020).

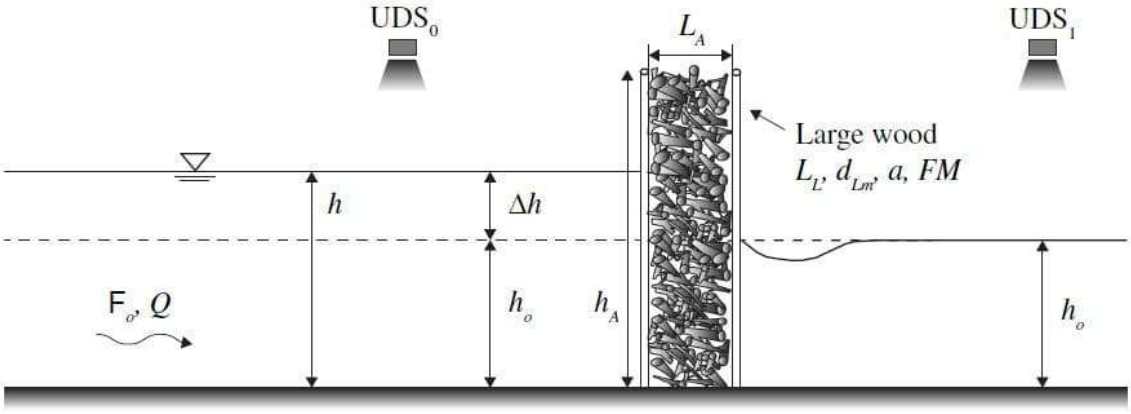

Figure 6: Schalko et al., 2018, fig. 2, Test setup and notations, UDS = ultrasonic distance sensors.

They tested the influence of numerous parameters on the resulting backwater rise, referred as $\Delta h = h - h_0$:

- The LW accumulation characteristics with:
  - the accumulation length L_A and height h_A
  - the log length L_L and mean log diameter d_{Lm},
  - the compactness of the accumulation with the bulk factor $a = \frac{V_L}{V_S}$, where V_L = loose large wood volume and V_S = solid large wood volume.
  - the presence of fine materials with the parameter FM which is a percentage of V_S, varying from 2 to 17%.
- The initial approach flow conditions, measured without LW accumulation:
  - the initial water depth h_0,
  - the initial Froude number F_0,
  - the discharge Q

These laboratory experiments led to the derivation of an equation for backwater rise (eq. 5). The backwater rise depends on the initial approach flow conditions, the dimensions of the LW, the characteristics of the accumulation and the presence of fine materials likes leaves or branches in the accumulation.

$$\frac{\Delta h}{h_0} = 5.4 LW_A = 5.4 \frac{F_0 u^{1/3}(9FM + 1)}{a^{4/3}} \tag{5}$$

where $u = L_A/d_{Lm}$ is a nondimensional parameter called the flow diversion factor.

But in natural environment, LW accumulations are not box-shaped. LW accumulations at single retention rack were investigated by Schalko and Schmocker and Hager (Schalko et al., 2019a, Schalko et al., 2019b, Schmocker and Hager, 2013).

Schmocker and Hager conducted a large laboratory experiment campaign to reduce the laboratory efforts when studying LW blockage at single racks (fig. 7) (Schmocker and Hager, 2013).

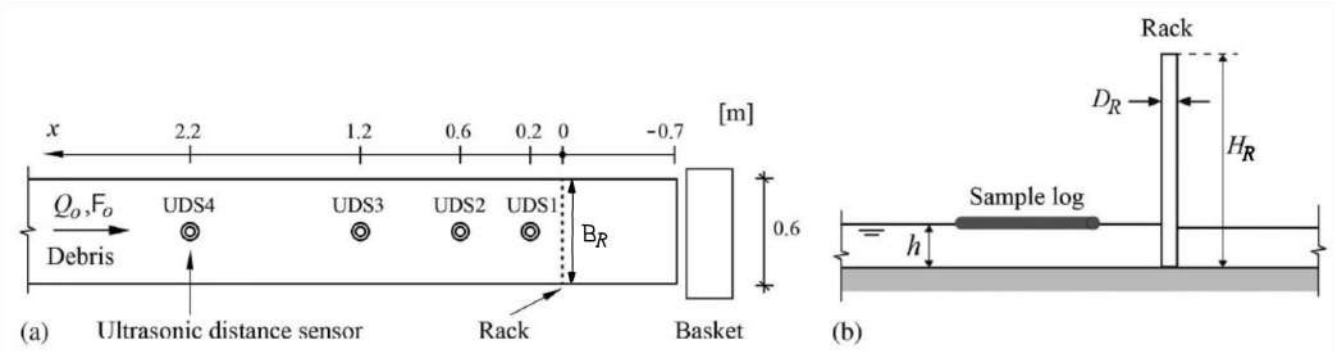

Figure 7: Schmocker and Hager, 2013, fig. 1, (a) Plan view of test setup for frontal approach flow to debris rack and arrangement of UDS_s; (b) side view of debris rack.
notations: H_R and D_R are the height and the diameter of the poles of the rack, B_R is the width of the rack and h is the water depth.

They observed that the formation process of a natural LW accumulation can be divided into two phases:

1. The initial debris accumulation at the rack, during which the major backwater rise takes place (fig.8a),
2. The debris carpet formation, during which only a minor backwater rise occurs (fig.8b).

(a) Schmocker and Hager, 2013, fig.3, Initial debris accumulation.

(b) Schmocker and Hager, 2013, fig.3, Debris carpet formation.

Figure 8: Formation process of a natural LW accumulation.

They investigated 6 parameters and determined which of them had significant effects on the LW jam formation and the backwater rise, thus were worth modeling at the lab scale.
The studied parameters are

- the pole diameter D_R,
- the water content of the wood,
- the test duration,
- the debris mixture,
- the volume of the debris,
- and the Froude number.

The pole diameter had no effect, neither does the water content of the debris, as long as they were floating. The test duration has only small effect. Indeed, a minimum test duration is required to guarantee the compaction of the debris rack, but past this time, the final backwater rise is independent of the test duration. No effect of the debris mixture could be deduced from these experiments.

The volume of debris significantly influences the rise of backwater during the initial phase of the accumulation process. However, once this phase is completed and the entire cross-section of the flume is blocked, additional debris primarily contributes to the length of the debris carpet rather than causing a substantial increase in the backwater rise.

The Froude number is the most impactful parameter. The relative water depth h/h_0 increases linearly with the initial Froude number F_0 while relative carpet length L_A/B_R (L_A is the carpet length, B_R is the rack width) decreases linearly with increasing F_0.
The fit equations are expressed for $0.5 < F_0 < 1.5$ (eq. 6 and 7).

$$\frac{h}{h_0} = 1.4 + 1.9F_0 \tag{6}$$

$$\frac{L_A}{B_R} = 6.6 - 2.6F_0 \tag{7}$$

The higher the F_0, the higher is the flow velocity. The logs are then carried further under the existing carpet, which reduces the cross-section of the flume. The backwater rise increases, along with the compactness of the accumulation and the debris carpet. (Schmocker and Hager, 2013).

Schmocker and Hager thus concluded that the parameters with a significant effect on backwater rise are the Froude number of the approach flow and the debris volume (Schmocker and Hager, 2013).

Following this study, Schalko conducted a series of experiments, including some analyzing the effect of organic fine materials and movable bed. Two different model scales with the scale factors $\lambda = 6$ and $\lambda = 30$ were investigated with a fixed bed. Movable bed were included in the study to identify the effect on scour (Schalko et al., 2019b).

The setups for these experimental studies are presented in figure 9. Series A correspond to tests performed with a fixed bed, while series B includes tests with a movable bed.

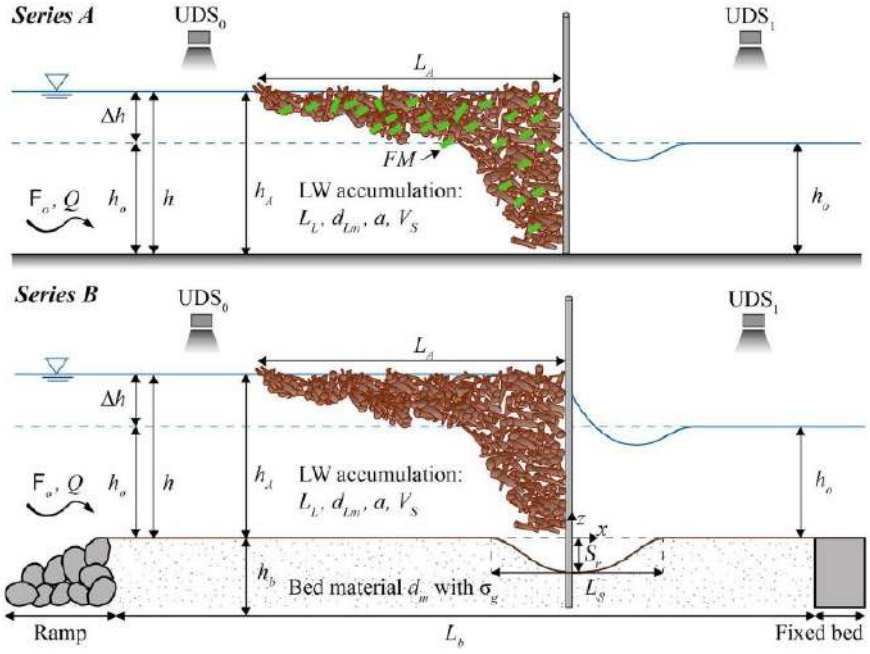

Figure 9: Schalko et al., 2019a, fig. 2, Test setups and notations for test series A (fixed bed) and B (movable bed).

For test series A, all the notations were introduced previously. For test series B, notations relative to the movable bed are added. Bed material characteristics are bed material height h_b, length L_b, mean grain size diameter d_m, geometric standard deviation of grain size distribution σ_g, scour length L_S, and scour depth at rack S_r (Schalko et al., 2019b).

This study shows that natural accumulation leads to a lower backwater rise than a predefined accumulation (reduction of approximately 40%), and that local scour also leads to a 67% decrease of the backwater rise.

A parameter f_A to account for the shape of the accumulation (predefined or natural) and the material of the bed (movable or fixed) was determined in this study. It can take 3 different values:

- $f_A = 1$ for a predefined accumulation
- $f_A = 0.55$ for a natural accumulation and a fixed bed
- $f_A = 0,3$ for a natural accumulation and a movable bed

This parameter, called the accumulation type factor, extends the equation 5 to better fit the data (eq.8):

$$\frac{\Delta h}{h_0} = 5.4 f_A L W_A = 5.4 f_A \frac{F_0 u^{1/3}(9FM+1)}{a^{4/3}} \tag{8}$$

Schalko et al. defined a characteristic volume of debris V_c, responsible for the main backwater rise Δh_c occurring during the first phase of the accumulation process.

By scaling this characteristic volume by Bh_0^2, where B is the width of the flume and h_0 the initial water depth, a relative debris volume is obtained. This is made under the assumption that V_c has the same volume as a box-shaped accumulation of Bh_0^2.

In its normalized form, V_c is a function of the initial flow Froude number for fixed bed, and of the initial flow Froude number, flow depth and mean grain size diameter for movable bed (equations 9 and 10).

$$\frac{V_c}{Bh_0^2} = 3.1 F_0 \quad \text{Fixed bed} \tag{9}$$

$$\frac{V_c}{Bh_0^2} = 3.1 F_0 (\frac{h_0}{d_m})^{-0.2} \quad \text{Movable bed} \tag{10}$$

Wang et al. also studied the LW accumulation and the resulting backwater rise, but at slit-check dams in rivers with high sediment transportation. Their study focuses on the influence of sediment concentration. The parameters tested were the LW length L, number N, the total volume V_d, the initial flow Froude number F_0, the sediment concentration C_V, the density of the debris flow ρ_f, and the relative density ρ_f/ρ_d with ρ_d, the density of the LW.

They identified four phases during the backwater rise (fig. 10):

1. Slight variation phase ① – ②;
2. Rapidly growing phase ② – ③;
3. Slow growth phase ③ – ④;
4. Almost constant value phase ④ – ⑤.

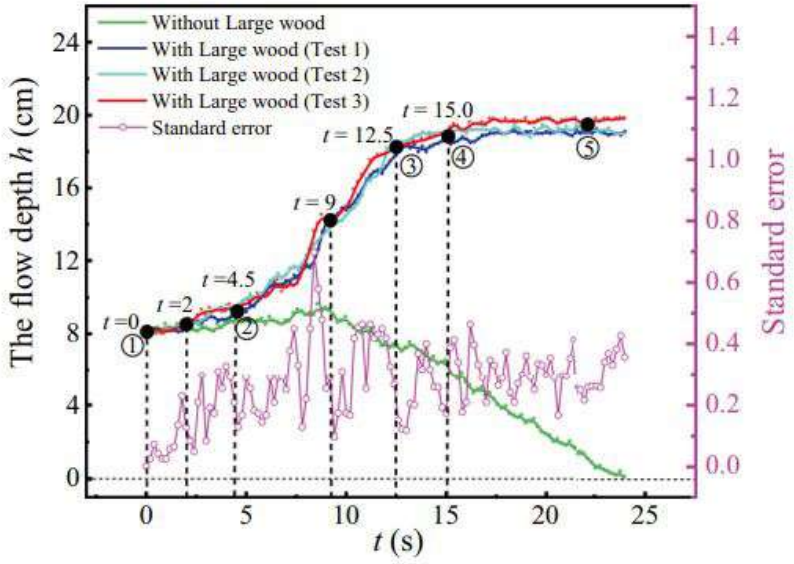

Figure 10: Wang et al., 2022, fig. 6, The temporal development of the flow depth.

The characteristic wood volume generating the primary backwater rise defined by Schalko et al. (eq. 9 and 10) was extended to debris flow. In its normalized form, this volume depends on the initial Froude number F_0, the initial of flow depth h_0 and the dimensionless sediment concentration C_V (eq. 11):

$$\frac{V_c}{Bh_0^2} = aF_0 + b \tag{11}$$

with

$$a = 1.46C_V^{-0.82} \text{and } b = 2.10C_V^{1.47}$$

They found out that the relative backwater rise increases with the sediment concentration and with the initial Froude number.

Schalko's equation for backwater rise (eq. 8) can be expressed in another form (eq. 12):

$$\frac{\Delta h}{h_0} = 1.62\frac{F_0(V_d/h_0Bd_m)^{1/3}}{a} \tag{12}$$

Wang proposed a revised version of this equation to account for the debris flow (eq. 13):

$$\frac{\Delta h}{h_0} = \alpha\frac{F_0(V_d/h_0Bd_m)^{1/3}}{a} + \beta \tag{13}$$

where

$$\alpha = 0.42(\frac{\rho_f}{\rho_d})^{2.5} \text{and } \beta = -1.50(\frac{\rho_f}{\rho_d})^{0.6}$$

A synthesis of the contents and results from the different previously cited references (Schmocker and Hager, 2013, Schalko et al., 2018, Schalko et al., 2019a, Schalko et al., 2019b and Wang et al., 2022) is presented in the table 2.

Table 2: Comparison of the different studies about large wood accumulation at different blockage structures.

Autors Year	Study type	Study object	Studied parameters	Formula ?	Parameter influencing the LWblockage or the backwater rise	Blockage structure	Extra informations
Schmocker & Hager 2013	Exp.	Reduce the laboratory effort when studying LW blockage at single rack and resulting backwater rise	Froude number Pole diameter Water content of the wood test duration Debris mixture Debris volume	no	Froude number Debris volume	Single retention rack	
Schalko et al. 2018	Exp.	Effect of predefined accumulation between 2 racks on backwater rise	Accumulation characteristics (L_A, h_A, a) Log characteristics (L_L, d_{Lm}) Presence of fine materials (FM) Initial approach flow conditions (h_0, F_0, Q)	yes	Accumulation characteristics (L_A, a) Log characteristics (d_{Lm}) Presence of fine materials (FM) Initial approach flow conditions (h_0, F_0)	Double retention rack	
Schalko et al. 2019a	Exp.	Effect of accumulation at single rack on backwater rise, including the effect of fine materials and movable bed	Presence of fine materials (FM) Movable bed	yes	Presence of fine materials (FM) Movable bed	Single retention rack	Determination of a characteristic volume responsible for the main backwater rise
Schalko et al. 2019b	Exp.	Effect of accumulation at single rack on local scour, including the effect of fine materials and movable bed	Presence of fine materials (FM) Movable bed	yes	Presence of fine materials (FM) Movable bed	Single retention rack	
Wang et al. 2022	Exp.	Effect of accumulation at slit-check dam on backwater rise, including the effect of sediment concentration	Debris characteristics (L, N, Vd) Initial approach flow conditions (F_a) Sediment concentration (Cv) Density and relative density of the debris flow ($\rho_{\mathrm{l}}$and $\rho_{\mathrm{l}}/\rho_{\mathrm{d}}$) Density of the$LW$	yes	Initial approach flow conditions ($\mathrm{F_o}$) Sediment concentration (Cv) Relative density of the debris flow $(\rho_{\mathrm{r}}/\rho_{\mathrm{d}})$	Slit-check dam	Adaption of the characteristic volume of Schalko

2 Context of the present work

2.1 Recent events

In July 2021, Belgium, Germany, and the Netherlands experienced extreme flood. Huge damages (fig. 11) were observed, especially in the Vesdre and Ourthe Valley in Belgium, and in the Ahr Valley in Germany.

In Wallonia (Belgium), 209 municipalities (out of 262) were hit by torrential rains. 100 000 people have been affected, and 39 of them unfortunately died. The cost of the floods in July 2021 for the Walloon Region is close to 3 billion euros.

(a) (b) (c)

Figure 11: Images of the Vesdre Valley during and after the flood.

Many bridges have been clogged with floating debris. These LW accumulations resulted in a backwater rise, further increasing the water level, which was already much higher than usual.

Figure 12: Clogged bridge in the Vesdre Valley.

Even if the effect of LW accumulation upstream of the retention rack is well-known, the precise influence of the bridge's geometrical configuration ((shape and height of the deck, number and shape of the piles, shape and height of the railing)) on backwater rise and its effects are still not fully understood.

2.2 EMfloodResilience project

In this context, an Interreg Euregio Meuse-Rhine project entitled EMfloodResilience was initiated between 11 partners from Germany, the Netherlands, and Belgium. The overall objective is to be better prepared for the next extreme flood event (see https://emfloodresilience.eu/).

This project is divided into 6 workpackages. This thesis is in line with the fourth of them, entitled "Improve flood hazard and risk mapping based on the experiences in 2021". It is further divided into 3 sub-workpackages, the first of which is of interest:

4.1. Calculation with an experimental model of the behavior of floating debris

In this workpackage, University of Liège (Uliège), the University of Technology of Delft (TU Delft) and the Rhine-Westphalia Technical University of Aachen (RWTH Aachen) collaborate on data collection, modeling, and prediction related to floating debris and their impact on structures along the rivers of the EMR region during the floods in July 2021.
3 stages have been defined to accomplish this work:

1. Constitution of a database documenting floating debris and affected structures
2. Complementary experimental modelling in 3 laboratories (Aachen, Delft, and Liege)
3. Design recommendations and operational procedure

At the beginning of the present Master thesis, in January 2023, the first stage of the project was completed (4.1.a). A database including geometry parameters of the bridges of the EMR region and the debris accumulation was made available.

The second stage involves laboratory experiments. The Interreg project team decided to separate it in 3 phases, each of them with a particular objective:

- Phase 1: Considering a reference bridge and reference flow conditions, define a limited number of debris scenarios.
- Phase 2: Considering a reference bridge and the debris scenarios defined in the previous step, define a limited number of flow scenarios.
- Phase 3: Considering the debris scenarios and the flow scenarios, study the influence of the bridge geometry.

The figure 13 summarize the EMfloodResilience project and situates this master thesis within it.

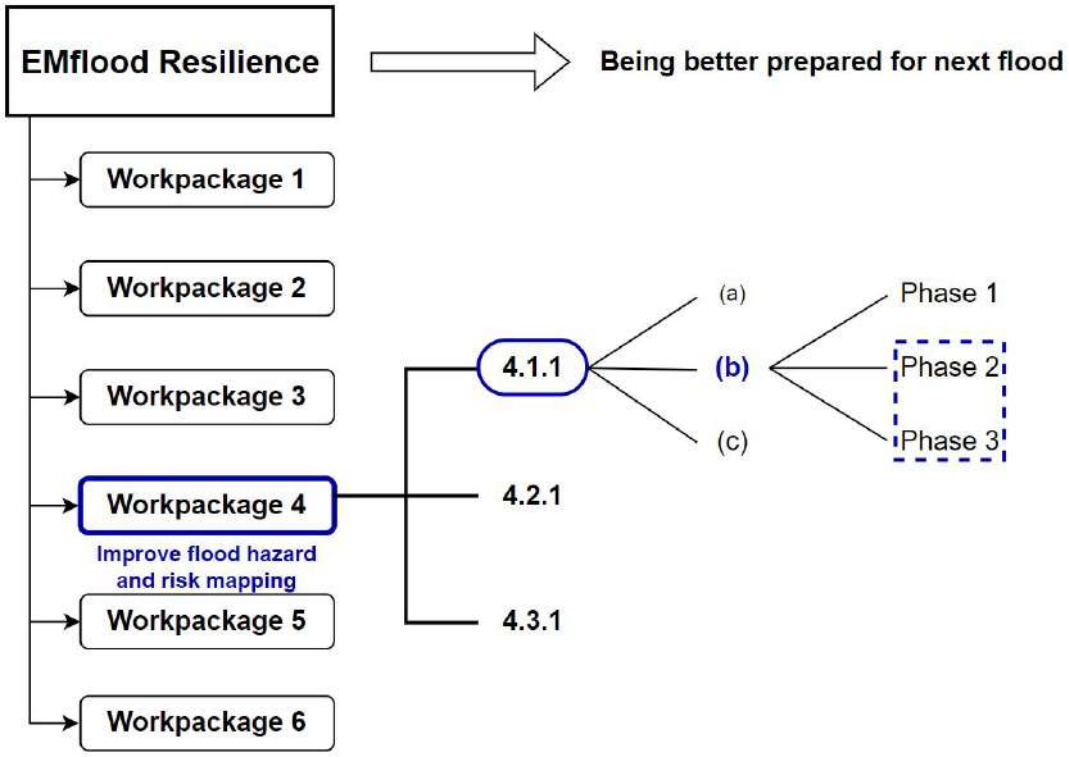

Figure 13: Description of the EMfloodResilience Project and link to this work.

2.3 Objectives

This master thesis is part of the second step of the stage b. As Phase 1 was already completed and the debris scenarios determined, it is focusing primarily on Phases 2 and 3. It considers 2 debris scenarios and 2 bridge configurations in a wide range of flow conditions.

Regarding the literature, consideration of bridges as blockage structures for LW accumulations is original. Furthermore, not only logs are considered but also 2D and 3D elements as plywood plates and cars for example.

Indeed, Schmocker and Hager, 2011 studied the probability of blockage at bridge but for single logs. In this master thesis, and in the EMfloodResilience project in general, the blockage at the bridge is considered as certain. Also, the wood volumes are extreme to approach Schalko's characteristic volume in order to recreate the worst-case scenario. The flow conditions studied are intense as well in order to reproduce flood conditions, because it is the context in which the backwater rise due to LW is the most problematic and mainly causes damages.

Part II
Methodology

3 Experimental set up

3.1 Flume

3.1.1 Description

The experiments were conducted at the Engineering Hydraulics Laboratory of the University of Liège.

The rectangular flume used has a discharge capacity of 170 L/s (±0.1%). It is 10 m long, 0.985 m wide (B) and 0.5 m high (see fig. 14).

Its side walls are made of glass, and the bottom is made of glass and PVC. The channel bottom is horizontal with a fixed slope. A downstream valve allows varying the water height h for constant discharges. The approach flow depth h_0 is measured with an accuracy of *1 mm* using ultrasonic distance sensors (UDS) (fig. 16).

The UDS are the vnp-35/IU/TC from Microsonic. They have an accuracy of ±1% and a measure range between 65 and 500 mm (see appendix C). They are placed approximately 540 mm above the bottom of the channel to prevent them from getting wet, while keeping the measurements in the range. Measurements are taken at a frequency of 10 Hz and the data acquisition is done with the software Labview.

There are 5 UDSs numbered from 0 to 4 and distributed along the flume as shown in figure 17.

Figure 14: Flume.

Figure 15: Vnp-35/IU/TC ultrasonic distance sensor from Microsonic.

Figure 16: Sensors in the flume.

Various flow conditions were established by adapting both the inflow discharge and the height of the downstream valve.

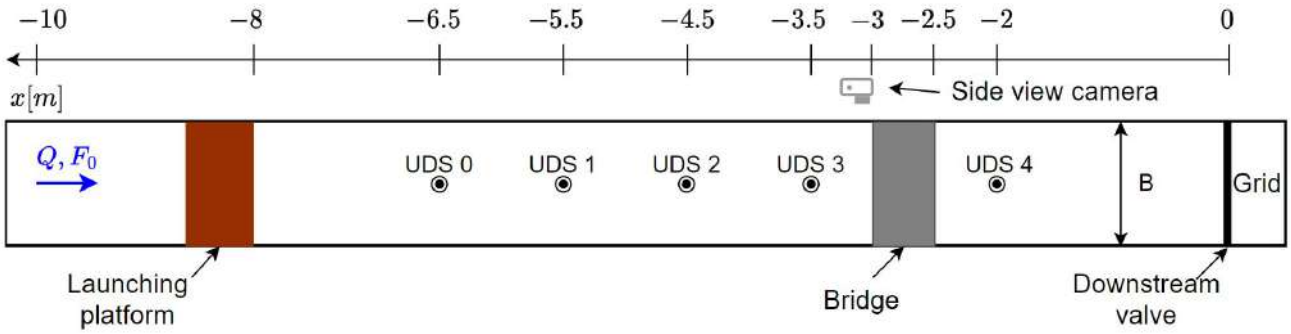

Figure 17: Plan view of the experimental setup and arrangement of UDS_s
Notations: B is the width of the flume, Q is the discharge and F_0 is the initial Froude number of the flow.

3.1.2 Roughness of the flume

Manning–Strickler formula (eq.(14)) can be used to describe the open-channel flow in the flume.

$$U = K_s R_h^{2/3} J^{1/2} \tag{14}$$

where

- $U[m/s]$ is the mean flow velocity through the cross-section
- $K_s[m^{1/3}/s]$ is the Strickler's coefficient, an empirical coefficient that depends on multiple factors, including surface roughness and sinuosity
- $R_h[m]$ is the hydraulic radius obtained by dividing the cross-sectional area of flow by the wetted perimeter: $R_h = \Omega/\chi$
- $J[m/m]$ is the hydraulic gradient

The process to determine the K_s coefficient is the following :

1. The water line for 2 different discharges and a critical downstream condition are calculated numerically for an estimated K_s.
2. Experimental water lines in the same flow conditions are measured in the flume by 4 sensors placed along the flume (in red and purple on the figure 18).

3. The K_s used to draw the numerical water lines is then adapted for these water lines (in light and dark blue on the figure 18) to fit the experimental values.

The fitting is done by the method of the least squares: the sum of the squared distances between the numerical and experimental values is calculated and then minimized by varying K_s.

The 2 different discharges tested are $70L/s$ and $120L/s$. 3 sets of measures for each discharge were taken. Each test gives a slightly different value for K_s (table 3).

Table 3: Strickler's coefficient for the 3 sets of each discharge tested.

Q [L/s]	set	$K_s[m^{1/3}/s]$
70	1	113.03
	2	113.13
	3	112.54
120	1	113.08
	2	113.05
	3	113.64

Mean $[m^{1/3}/s]$	113.08
Standard deviation $[m^{1/3}/s]$	0.35
Min $[m^{1/3}/s]$	112.54
Max $[m^{1/3}/s]$	113.64

The mean of these K_s is $113,08m^{1/3}/s$ (with a standard deviation of $0.35m^{1/3}/s$). The distance between two numerical water lines calculated for the same discharge with the minimum and maximal values for K_s is of maximum 0.3 mm which is smaller than the precision of the sensors. Therefore, a value of

$$K_s = 113m^{1/3}/s$$

will be used for the following work.

Figure 18 represents the experimental values and the numerical water lines calculated with a K_s of $113m^{1/3}/s$. It shows that the fitting is indeed correct.

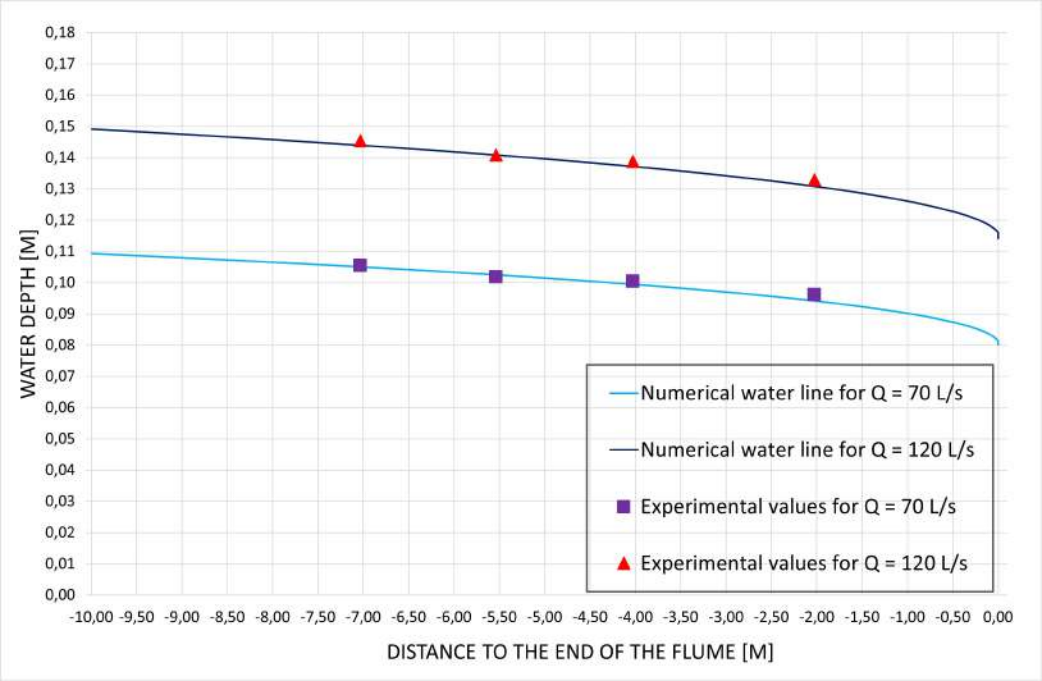

Figure 18: Numerical water lines ($K_s = 113m^{1/3}/s$) fitting experimental values.

3.2 Bridge

The bridge is placed at 2.5 m from the downstream end of the flume between the UDS 3 and 4 (fig. 17 and 19). A camera is placed next to the flume upstream of the bridge. It enables to take side-view pictures during the tests.

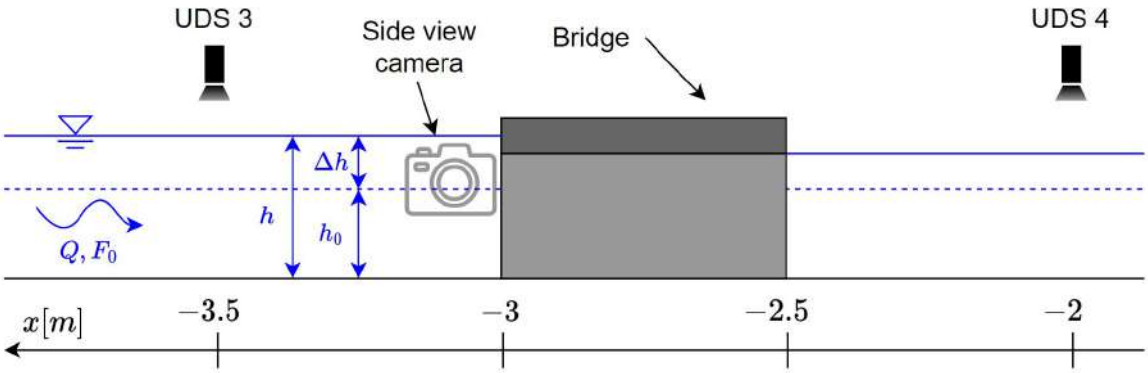

Figure 19: Side view of the experimental setup
Notations: h is the water depth,h_0 is the initial water depth and Δh is the backwater rise.

3.2.1 Geometry

To determine the bridge geometry, the database from the first step of the Interreg project is used. This database collects information about 152 bridges from Belgium, Germany, and Netherlands. It describes parameters such as the type of bridge, its location, shape, and the number of piers. The integrality of the parameters is presented at the appendix A.1.

From this database, only the 118 Belgian bridges are kept. The ones with no information on the geometry (72 bridges) are excluded. Then, only the bridges with a rectangular opening are taken into account. The railway bridges and the pedestrian bridges are excluded as well.

At the end, only 24 bridges are remaining. 4 of them have no pier, 13 of them have one pier, and the 7 remaining have two piers. The parameters of these 24 bridges are listed at the appendix A.2.

The mean of each geometric parameter is calculated for all the 24 bridges (mean rectangular bridges in fig. 4), the 13 bridges with one pier (mean 1 pier in fig. 4) and the 7 bridges with two piers (mean 2 piers in fig. 4). These results are presented in the figure 4.

The choices made for the reference dimensions of the bridge can be found in the last line of the table.

The opening width is chosen at 8.3 m to fit in the worst-case scenario in terms of risk of blockage and to make it possible to test bridges with one or two piers.

The pier width, the opening height and the deck thickness are chosen to be realistic while staying as close as possible to the mean value.

Table 4: Dimensions of the reference bridge.

	Opening width [m]	Pier width [m]	Opening height [m]	Deck thickness [m]	Bridge width [m]
Mean rectangular bridges	14,9	1,09	3,7	1,2	9,6
Mean 1 pier	13,6	1,10	4,0	1,3	9,6
Mean 2 piers	8,3	1,08	3,7	1,0	8,6
Choice	8,3	1,1	3,8	1,15	9,1

The first geometry tested is a one pier bridge. The scale of the model was determined for the total width (two opening width and one pier width) to fit the dimension of the flume (0.985 m).

The total width is $2 \times 8.3 + 1.1 = 17.7m$. The scale is then $0.985/17.7 = 0,056 \approx 1/18$. The scale factor is then

$$\lambda = 18$$

The model will then have an opening height $h_b = 21.1cm$, an opening width $w_b = 46,1cm$ and a pier width $w_{pb} = 6,1cm$. The deck is $6.4cm$ thick and $50cm$ wide (fig. 20a).

The second geometry tested is a two pier bridge (fig. 20b). The dimensions are the same as the one pier bridge, except that it has two piers. The maximum opening width is situated between the two piers and not between a pier and the side of the flume anymore, but is kept the same (46.1 cm).

The dimensions of the model bridges are shown in the table 5 and represented in the figure 21.

Table 5: Model bridge dimensions.

Characteristics	Geometry 1	Geometry 2
Pier number [/]	1	2
Pier width [m]	0.061	
Distance between the pier(s) and the left wall of the channel [m]	0.461	0.200 ; 0.722
Maximum Opening width [m]	0.461	
Opening height [m]	0.211	
Deck thickness	0.064	
Bridge width	0.500	

(a) (b)

Figure 20: Model bridges with one pier (a) and two piers (b) in the flume.

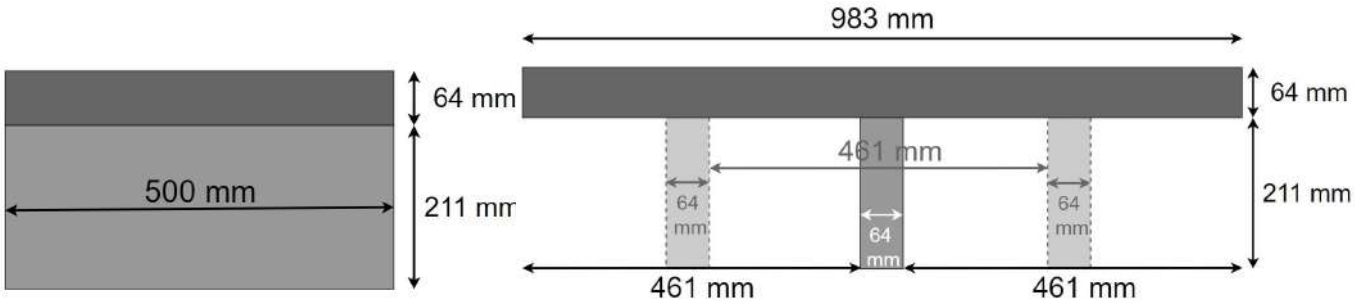

(a) Side view. (b) Front view.

Figure 21: Dimensions of the model bridge.

The bridge's plans are shown in the appendix B.

3.2.2 Head losses

The local head losses due to the bridge had to be calculated in order to be able to distinguish the head losses due to the LW accumulation and the one due to the bridge.

The head losses in the flow are composed of longitudinal and local head losses, such as :

$$\Delta H_{tot} = \Delta H_{long.} + \Delta H_{loc.} \tag{15}$$

The longitudinal losses are mainly due to the friction of the water against the sides of the canal and the bridge. They are already taken into account in the computation of the water lines.

The local head losses are due to a modification of the geometry of the flume. They can be computed with the equation 16:

$$\Delta H_{loc.} = \xi \frac{v^2}{2g} \tag{16}$$

Where coefficient ξ depends on the geometry change. The two geometries of the bridge are distinguished.

One pier

To determine the local head losses of the single pier, experimental measures are taken for 6 flow velocities. The choice of these 6 configurations is detailed in the section 5.1.

First, the total head losses $\Delta H_{tot,exp}$ are measured between the most upstream and the most downstream sensors (UDS 0 and 4).

Then, the longitudinal head losses $\Delta H_{long.}$ are calculated thanks to the water lines computation.

With these two quantities and equation (15), a first estimate of the local head losses can be calculated for each configuration.

$$\Delta H_{loc.,est.} = \Delta H_{tot,exp} - \Delta H_{long.}$$

A coefficient ξ can then be calculated for each configuration with equation(16).

$$\xi = \frac{H_{loc.,est.} 2g}{v^2}$$

Table 6: Computation of the coefficient of local head losses ξ, 1 pier.

Config.	v [m/s]	$\Delta H_{tot,exp.}$ [mm]	$\Delta H_{long.}$ [mm]	$\Delta H_{loc,est.}$ [mm]	$\xi_{est.}$ [/]
1	0.282	2.16	0.90	1.26	0.312
2	0.415	2.07	1.89	0.18	0.021
3	0.626	4.62	4.35	0.27	0.013
4	0.386	2.23	0.79	1.44	0.190
5	0.574	2.72	1.76	0.96	0.057
6	0.841	4.93	3.76	1.17	0.033
			Mean:		**0.104**
			Mean w/o outliers:		**0.031**

The results for each step described for the 6 configurations are presented in the table 6.

These coefficients ξ are represented on the figure 22 according to the velocity of the flow.

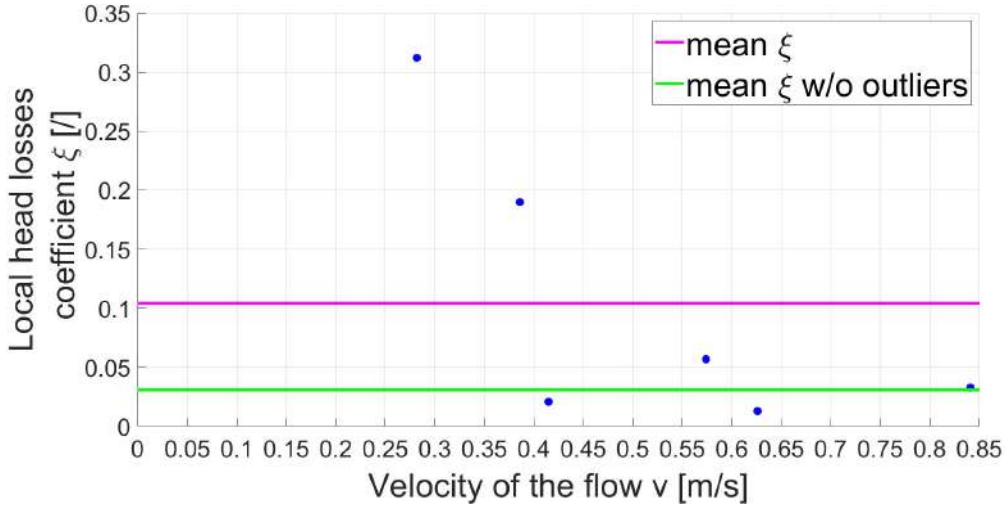

Figure 22: Local head losses' coefficient according to the velocity of the flow,1 pier.

As in can be seen in the table 6, the average of these coefficients is equal to 0.104. But on the figure 22, it is clear that the values of ξ for the lowest velocities (under $0.4m/s$) are higher than the ξ for the highest (over $0.4m/s$) velocities that seem to be in the same range. For that reason, the first two ξ coefficients are excluded of the computation of the mean.

The coefficient of local head losses for the bridge geometry with one pier is then assumed to be

$$\xi_{mean,1p} = 0.031$$

From this averaged ξ_{mean}, the local head losses are recomputed with equation (16) in order to verify that the assumption is correct.

$$\Delta H_{loc,calc.} = \xi_{mean,1p} \frac{v^2}{2g}$$

The total losses can then be calculated with equation (15) and compared to the experimental total losses. The assumption is considered correct if the difference between these quantities is of the order of 1 mm, which is the measurement precision of the UDSs.

The results of the described computation are presented in the table 7.

Table 7: Computation of the local head losses with ξ_{mean}.

Config.	v [m/s]	$\Delta H_{tot,exp.}$ [mm]	ξ_{est} [/]	ξ_{mean} [/]	$\Delta H_{loc,calc.}$ [mm]	$\Delta H_{tot,calc.}$ [mm]	$\lvert\Delta H_{tot,exp.} - \Delta H_{tot,calc.}\rvert$ [mm]
1	0.282	2.16	0.312	0.031	0.13	1.14	1.0
2	0.415	2.07	0.021		0.275	2.37	0.3
3	0.626	4.62	0.013		0.63	5.28	0.7
4	0.386	2.23	0.190		0.24	1.25	1.0
5	0.574	2.72	0.057		0.53	2.71	0.01
6	0.841	4.93	0.033		1.13	5.55	0.6

By analyzing the table 7, it can be concluded that the assumption for $\xi_{mean} = 0.031$ is correct. Indeed, the computed total head losses are all within the $\pm$ 1 millimeter range around the measured losses.

Two piers

The same methodology is followed for the bridge with two piers.

First, the coefficient of local head losses ξ is computed for each velocity (see tab .8).

Table 8: Computation of the coefficient of local head losses ξ, 2 piers.

Config.	v [m/s]	$\Delta H_{tot,exp.}$ [mm]	$\Delta H_{loc,est.}$ [mm]	$\xi_{est.}$ [/]
1	0.281	0.73	0.35	0.087
2	0.413	2.8	0.55	0.063
3	0.605	8.63	2.52	0.135
4	0.386	1.19	0.36	0.047
5	0.569	6.02	4	0.242
6	0.823	14.96	9.73	0.282
			Mean:	**0.143**

These coefficients ξ are represented on the figure 23 according to the velocity of the flow.

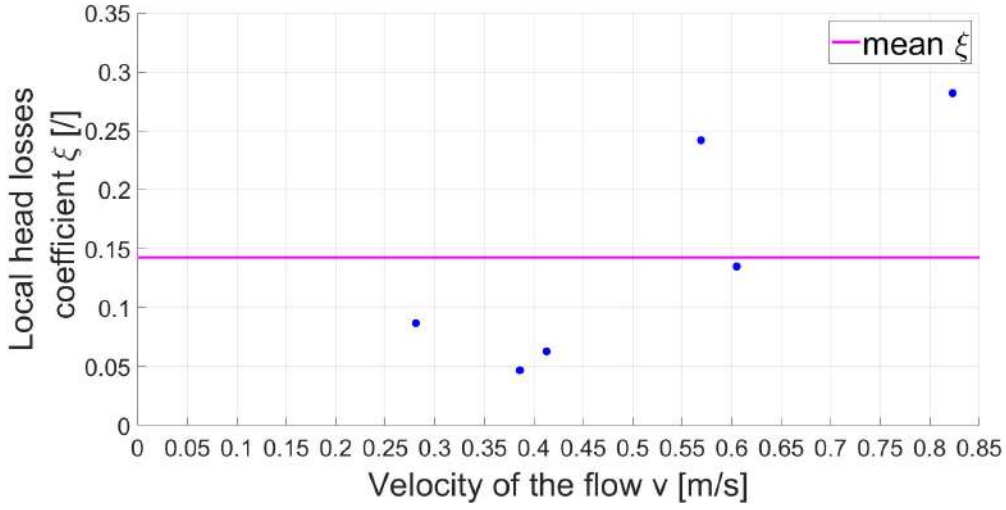

Figure 23: Local head losses' coefficient according to the velocity of the flow,2 piers.

As in can be seen in the table 8, the average of these coefficients is equal to 0.143. The coefficient of local head losses for the bridge geometry with two piers is then assumed to be

$$\xi_{mean,2p} = 0.143$$

From this averaged $\xi_{mean,2p}$, the local head losses are recomputed with equation (16) in order to verify that the assumption is correct.

Table 9: Computation of the local head losses with ξ_{mean}.

Config.	v [m/s]	$\Delta H_{tot,exp.}$ [mm]	ξ_{est} [/]	ξ_{mean} [/]	$\Delta H_{loc,calc.}$ [mm]	$\Delta H_{tot,calc.}$ [mm]	$\lvert\Delta H_{tot,exp.} - \Delta H_{tot,calc.}\rvert$ [mm]
1	0.281	0.73	0.087	0.143	0.57	1.47	0.7
2	0.413	2.8	0.063		1.25	4.27	1.5
3	0.605	8.63	0.135		2.93	9.77	1.1
4	0.386	1.19	0.047		1.08	2.93	1.3
5	0.569	6.02	0.242		2.43	6.4	0.4
6	0.823	14.96	0.282		5.56	13.73	1.2

By analyzing the table 9, it can be concluded that the assumption for $\xi_{mean} = 0.143$ is correct. Indeed, the differences between the computed and the measured total losses are all the order of 1 mm.

The head losses due to the piers will later be neglected. Indeed, in comparison to the head losses due to the accumulations, they are small. This will be detailed later in the document.

4 Floating debris

In order to represent the different kinds of floating debris that clocked the bridges during the floods of 2021, 3 types of model wooden floating debris are used:

1. Natural wood to represent the trees and branches (fig. 24a)
2. 2D-elements in wood, called “plates” in this document (fig. 24b)
3. 3D-elements in wood, called “cubes” in this document (fig. 24c)

(a) (b) (c)

Figure 24: Debris types, (a) Natural wood, (b) 2D elements, (c) 3D elements.

4.1 Natural wood

Trees and branches in LW accumulations can be of very different sizes. By analyzing pictures of the remaining LW accumulations after the flood of July 2021, it could be determined that the size of the pieces ranges from 1.5 m to 13 m. Some examples of the pictures used are given at figure 25.

(a) (b)

Figure 25: Large wood accumulations at bridges.

Size distribution

Two studies were used as reference to determine the size distribution of the natural wood: Bezzola and Hegg, 2007 and Rickli and Hess, 2009 (see fig. 26).

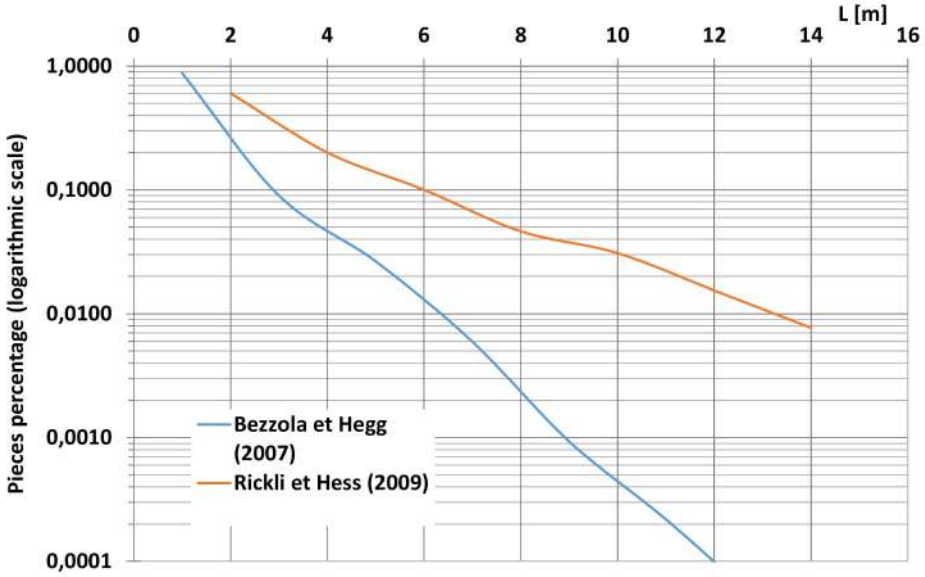

Figure 26: References size distribution of natural debris according to 2 studies.

The first one, (Bezzola & Hegg 2007), observed the size distribution of the wood pieces stocked in four accumulation structures in Switzerland after a flooding event in 2005.

The second one, (Rickli & Hess 2009), counted and measured driftwood in 10 streams in Switzerland after the same flooding event.

Because the flow and wood conditions in the studied rivers in the present work are closer to the second study, we tried to reproduce a distribution as close as possible to the one determined by Rickli & Hess.

The model logs used in the experiments have a length L_L varying from 10 cm to 70 cm and a mean diameter d_{Lm} varying from 5 cm to 35 cm (the ratio D/L is equal to 20) (see column "model L" and "model D" of the table 10). By multiplying these dimensions by the scale factor $\lambda = 18$, the real life dimensions are obtained. These are represented in column "L" and "D" of the table 10.
In order to follow the distribution of Rickli & Hess, the percentage for each type of piece needs to be the one presented at the column "piece %" of the table 10.

Table 10: Model Log length and diameter, corresponding real life length and diameter, percentage of every type of piece.

	model L [m]	model D [m]	L[m]	D[m]	piece %
1	0.100	0.005	1.8	0.09	61.80
2	0.200	0.010	3.6	0.18	18.26
3	0.300	0.015	5.4	0.27	9.55
4	0.400	0.020	7.2	0.36	5.06
5	0.500	0.025	9	0.45	2.81
6	0.600	0.030	10.8	0.54	1.69
7	0.700	0.035	12.6	0.63	0.84

This distribution is represented in red on the figure 27 with the distribution from Bezzola & Hegg and Rickli & Hess.

Figure 27: Size distribution of the natural debris.

4.2 2D elements

Besides trees and branches, large plates of different kinds were found in the accumulations at bridges. These could be plywood plates, form work plates, walls of houses, ...
These 2D elements are idealized and represented by plates with dimensions of 10×6×0.2 cm (fig. 24b). Multiplied by the scale factor, these dimensions correspond to plates with a length of 1.8 m and a width of ≈ 1 m.

The plate thickness is not measured precisely. For that reason, the quantity of plates will not be expressed in number of plates but in total thickness.
For example, if $3dm^3$ of plates is needed, it will mean that a stack of $\frac{3}{1\times0.6} = 5dm = 50cm$ of plates is needed.

4.3 3D elements

In addition to the logs and plates, more massive elements like containers, cars or even trailers were clogged in the LW accumulations.

As the 2D elements, these debris were idealized and represented by "cubes" with the dimensions 9×9×18 cm. At 1:1 scale, these dimensions correspond to a Fiat 500 car (≈3.2×1.6 m).

4.4 Quantity

The quantity of each type of debris was determined during the first phase of the project, before the beginning of the present work.

The different mixtures tested during the phase 1 are the following:

1. 100% logs
2. 75% logs, 25% cubes

3. 50% logs, 50% cubes
4. 75% logs, 25% plates
5. 50% logs, 50% plates
6. 60% logs, 20% cubes, 20% plates
7. 40% logs, 30% cubes, 30% plates

These mixtures are represented by the blue squares on the figure 28.

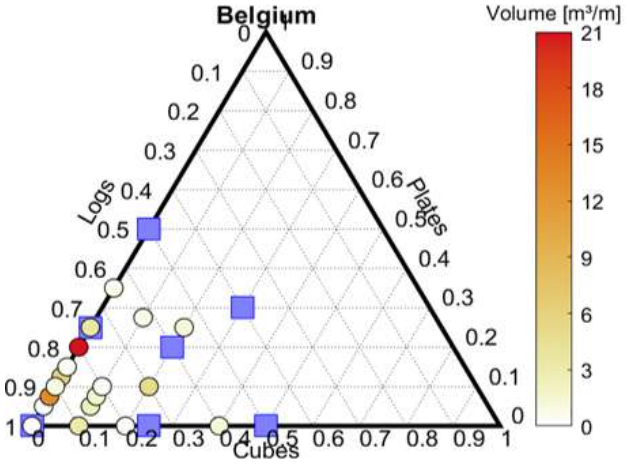

Figure 28: Tested mixture.

The backwater rises resulting from these mixtures are shown in the figure 29.

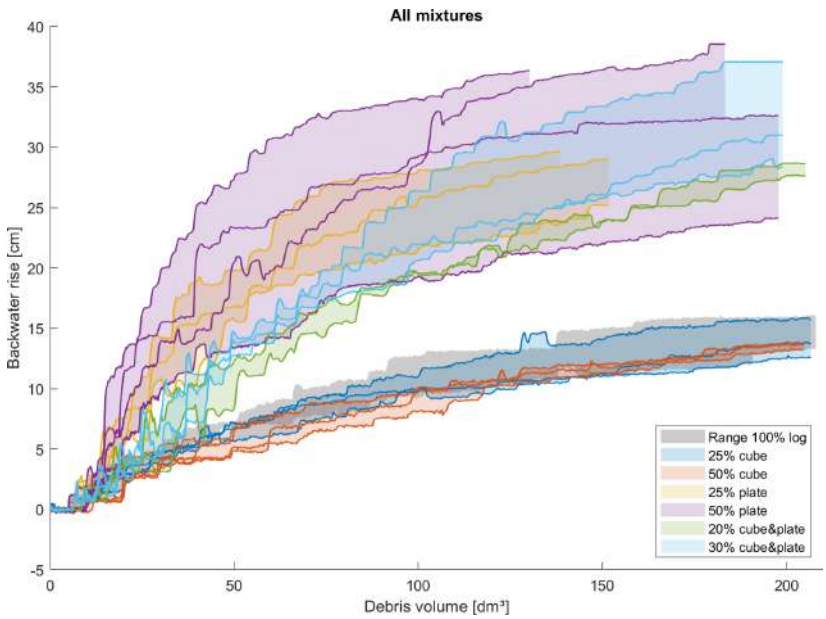

Figure 29: Backwater rise resulting from all mixtures measured during the first phase of the project.

The mixtures tested in the context of this master thesis are mixtures with 75% of logs and 25% of either cubes or plates. This choice was made because these mixtures are intermediate in the sens of they don't give extremely low or high backwater rise.

In the first phase, it was observed that cubes cause a smaller backwater rise than plates.

On figure 29, it is clear that the backwater rise is increasing slower when the volume of debris reaches 70 dm^3. This volume corresponds to $70 \times 16^3 = 286720 dm^3 = 286.72 m^3$ in the 1:1 scale (the scale factor of the phase 1 set up is $\lambda = 16$). Scaled for the phase 2, this volume becomes $286720/18^3 = 49.16 \approx 50 dm^3$.

The full debris volume is then 50 dm^3 with $0.75 \times 50 = 37.5 dm^3$ of logs and $0.25 \times 50 = 12.5 dm^3$ of cubes or plates.
Because of the given volume of the cubes, it is not possible to use exactly 12.5 dm^3 of cubes. The closest volume achievable is $9 \times 0.9 \times 0.9 \times 1.8 = 13.1 dm^3$. To be consistent, the volume of plates is also of $13.1 dm^3$ and the volume of logs is $37.6 dm^3$ which correspond to 74.1% of logs and 25.9% of others. The total volume is then $50.7 dm^3$
The numbers of logs of each size are given at the table 11.

Table 11: Quantity of logs of different sizes.

	L[m]	D[m]	Unit volume [m^3]	#pièces	Volume [m^3]
1	0,1	0,005	$1,9635 \times 10^{-6}$	660	0,001296
2	0,2	0,01	$1,5708 \times 10^{-5}$	195	0,003
3	0,3	0,015	$5,30144 \times 10^{-5}$	102	0,005
4	0,4	0,02	0,000125664	54	0,007
5	0,5	0,025	0,000245437	30	0,007
6	0,6	0,03	0,000424115	18	0,008
7	0,7	0,035	0,000673479	9	0,006
			Σ	1424	0,0376

To reproduce the conditions in which the accumulation are formed in the rivers, this volume of debris needs to be added progressively. But for practical reasons, it is impossible to add it continuously. Furthermore, an accumulation needs to formed and for that, a certain amount of woods needs to arrive simultaneously at the bridge.

The volume is thus added in five batches of $\approx 10 dm^3$.

The numbers of each size of logs and cubes or plates in each batch is represented in the tables 12 and 13.

Table 12: Quantity of logs and cubes in each batch for mixtures with ≈ 25% cubes and 75% logs.

	Batch1	Batch2	Batch3	Batch4	Batch5	**Total**
1	132	132	132	132	132	**660**
2	39	39	39	39	39	**195**
3	21	21	20	20	20	**102**
4	11	11	11	11	10	**54**
5	6	6	6	6	6	**30**
6	4	4	4	3	3	**18**
7	2	2	2	2	1	**9**
#cubes	2	2	2	2	1	**9**
Volume cubes [m^3]	0,00292	0,00292	0,00292	0,00292	0,00146	**0,0131** =13,1L: 25,9 %
Volume logs [m^3]	0,0079	0,0079	0,0078	0,0074	0,0066	**0,0376** = 37.6L: 74.1 %

Table 13: Quantity of logs and cubes in each batch for mixtures with $\approx 25\%$ plates and 75% logs.

	Batch1	Batch2	Batch3	Batch4	Batch5	**Total**
1	132	132	132	132	132	**660**
2	39	39	39	39	39	**195**
3	21	21	20	20	20	**102**
4	11	11	11	11	10	**54**
5	6	6	6	6	6	**30**
6	4	4	4	3	3	**18**
7	2	2	2	2	1	**9**
Plates [cm]	43,7	43,7	43,7	43,7	43,7	$\mathbf{218,5}$
Volume plates $[m^3]$	0,00262	0,00262	0,00262	0,00262	0,00262	$\mathbf{0,0131}$ =13,1L 25,8%
Volume logs $[m^3]$	0,0079	0,0079	0,0078	0,0074	0,0066	$\mathbf{0,0376}$ =37,6L 74,2%

5 Test program and procedure

5.1 Hydraulic configurations

Ten hydraulics configurations are tested. They are determined by 5 values of initial water depth and 3 Froude numbers.
For the highest water depth, it is not possible to reach a Froude number of 0.27. For this reason, the measurements are made at a Froude of 0.2 .

Table 14: Configurations.

$Fr_0[-]$ $h_0[mm]$	0.27	0.40	0.60
100	Config. 1	Config. 2	Config. 3
200	Config. 4	Config. 5	Config. 6
240	Config. 7	Config. 8	/
310	Config. 9	/	/
375	Config. 10 (! $Fr_0 = 0.20$!)	/	/

The five different water depths allow to experiment on one water depth far below the deck ($h_0 = 100mm$), one just below the deck ($h_0 = 200mm$), one at the deck ($h_0 = 240mm$) and two above the deck ($h_0 = 310\text{and}375mm$) (see fig. 30).

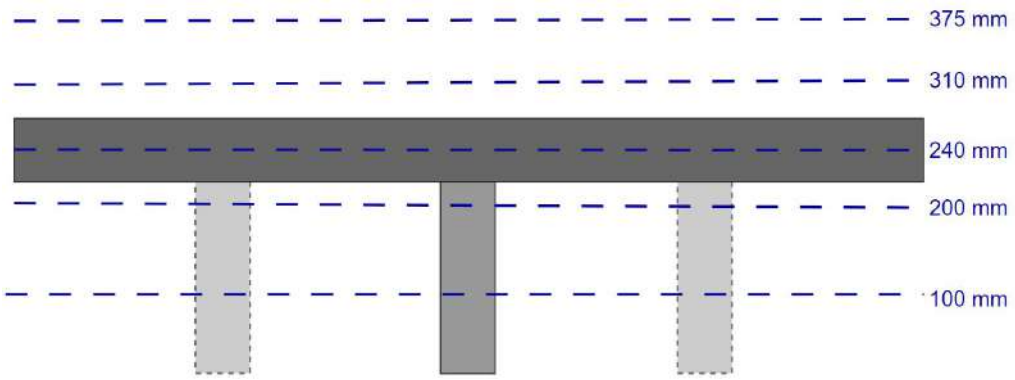

Figure 30: Tested initial water depths.

The range of Froude numbers was determined in order to fit the range observed during the 2021 flood in the Vesdre river. This range goes from 0.2 to 0.8. A Froude number of 0.8 could not be reached in the present set up. The reachable Froude numbers are represented at the figure 31. The Froude of 0.27 was chosen to match the one used in the first phase of the project in order to be able to compare the results.

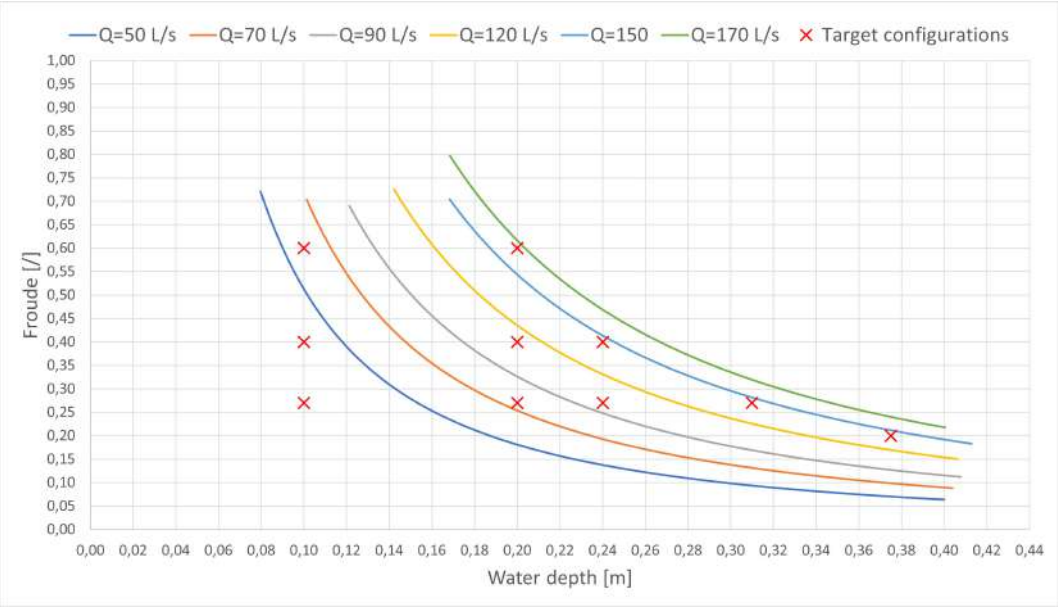

Figure 31: Reachable Froude numbers for different discharges according to the water depth.

5.2 Test program

Overall, 79 tests were conducted (see table 15). Each test is referenced to with the format [*Letter number number_number* p].
The first item is the letter C or P, referring to the mixture tested. C stands for the mixture with 25% cubes and P stands for the mixture with 25% plates.
The second item is a number between 1 and 10 referring to the configuration tested.
The third item is a figure between 1 and 3 referring to the repetition.
After the underscore, the number refers to the number of piers and the piers stands for "pier(s)".

For example, $C7\_1p$ corresponds to an experiment conducted with a debris mixture composed of 25% of cubes and 75% of logs, with an initial water depth, h_0, equal to 240 mm, an initial Froude number equal to 0.27 on a one pier bridge. $C7\_2p$ corresponds to an experiment conducted with the same debris mixture, in the same hydraulic conditions, but on a two pier bridge.

For the two series of tests (C and P), the same 10 configurations of initial Froude numbers (Fr_0) and flow depth (h_0) were tested.

Table 15: Test program.

Tests	$h_0[mm]$	$Fr_0[-]$	# piers	Logs [%]	Plates [%]	Cubes [%]	# repetitions
C1_1p		0.27					
C2_1p	100	0.4					3
C3_1p		0.6					
C4_1p		0.27					
C5_1p	200	0.40					2
C6_1p		0.60			0	25	
C7_1p	240	0.27					2
C8_1p		0.4					
C9_1p	310	0.27					2
C10_1p	375	0.2	1	75			3
P1_1p		0.27					
P2_1p	100	0.4					2
P3_1p		0.6					
P4_1p		0.27					
P5_1p	200	0.4					2
P6_1p		0.6			25	0	
P7_1p	240	0.27					2
P8_1p		0.4					
P9_1p	310	0.27					2
P10_1p	375	0.2					3
C1_2p		0.27					
C2_2p	100	0.4					2
C3_2p		0.6					
C4_2p		0.27					
C5_2p	200	0.40					2
C6_2p		0.60			0	25	
C7_2p	240	0.27					2
C8_2p		0.4					
C9_2p	310	0.27					2
C10_2p	375	0.2	2	75			3
P1_2p		0.27					
P2_2p	100	0.4					2
P3_2p		0.6					
P4_2p		0.27					
P5_2p	200	0.4					2
P6_2p		0.6			25	0	
P7_2p	240	0.27					2
P8_2p		0.4					
P9_2p	310	0.27					2
P10_2p	375	0.2					2

5.3 Test procedure

Each test followed the same procedure.

First, a constant discharge and the downstream valve height are set depending on the tested configuration (see tab.16) .

Table 16: Discharge and valve height for each configuration.

Fr	0,27		0,4		0,6	
h[mm]	Q[L/s]	Valve height [cm]	Q[L/s]	Valve height [cm]	Q[L/s]	Valve height [cm]
100	26	4,3	39	3,2	59	1,7
200	75 (27, 5 Hz)	9	110 (35, 6 Hz)	6,6	165 (49, 7 Hz)	4
240	98 (32, 1 Hz)	10,5	145 (44, 6 Hz)	7,5	/	/
310	144 (44, 2 Hz)	12,8	/	/	/	/
375	142 (43, 6 Hz) (Fr = 0.2)	20	/	/	/	/

Then, the debris are introduced in the flow using a launching board in 5 batches of 10 dm^3. The launching board (fig. 32) is situated 8 m upstream from the end of the flume and 5 m upstream from the bridge (fig. 17).

Figure 32: One of the 5 batches ($\approx 10L$ of wood).

For each batch, the debris that passed the bridge are re-added in the flow until they get stuck in the accumulation.
At least 3 minutes are needed between each batch in order to let the flow stabilize.

When all the volume of wood is in the flume, the flow is fully stabilized after 3 min and the measurement can thus be stopped 3 minutes after the last launch of wood.

Several parameters are measured during the test. The water height is measured at different axial positions with the 5 ultrasonic sensors. These water heights are later converted in back-water rise. The accumulation length is measured at the end of each test. In addition, a side view camera is taking a picture every minute during the test (fig. 33a) and a top-view picture is taken after each launch of a batch (fig. 33b).

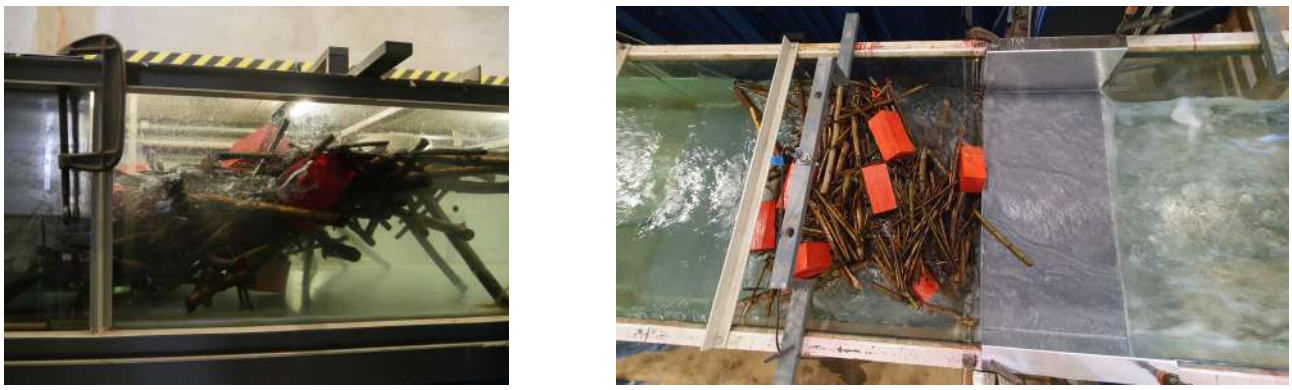

(a) (b)

Figure 33: Side (a) and top (b) view pictures of the test $C06\_1p$.

6 Data analysis

6.1 Sensors calibration

The sensors deliver data in Volt. To convert this voltage into a distance, the sensors have to be calibrated. 3 or 4 point calibrations were used for all the sensors and the determination coefficients R^2 are equal to 1 for all of them.

6.2 Data cleaning

Some noise can be observed in the data. Indeed, once the voltage is converted into a distance, the evolution of the water depth during the test can be represented (see fig. 34).

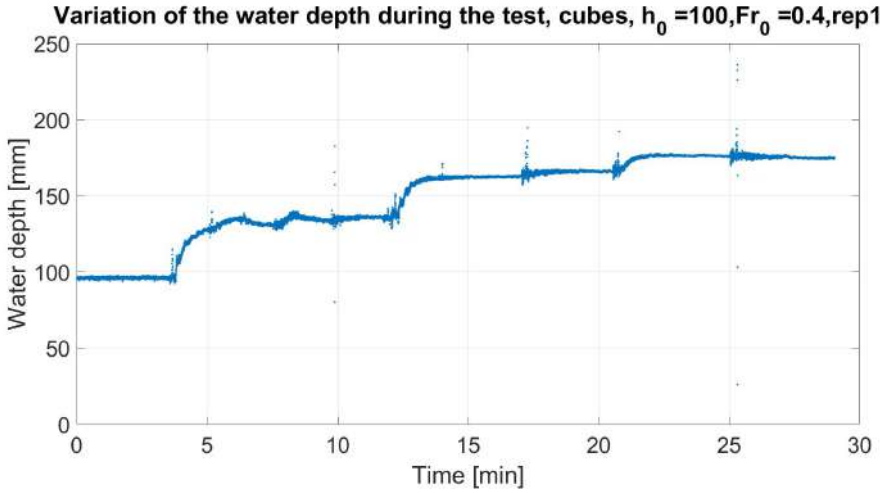

Figure 34: Raw water depth during the test $C021\_1p$.

In order to clean the data, the outliers need to be removed. For that, a specific code is written in Matlab. A moving mean is computed over a 100 points window which corresponds to 10s of measures as the data acquisition frequency equals 10Hz.
Once the average is computed, a point is considered as an outlier if it deviates by more than 2 standard deviations from the local mean. The outliers are replaced by the local mean. This treatment is applied as many times as necessary to remove all outliers.
The difference between the raw and the cleaned data is illustrated at the figure 35

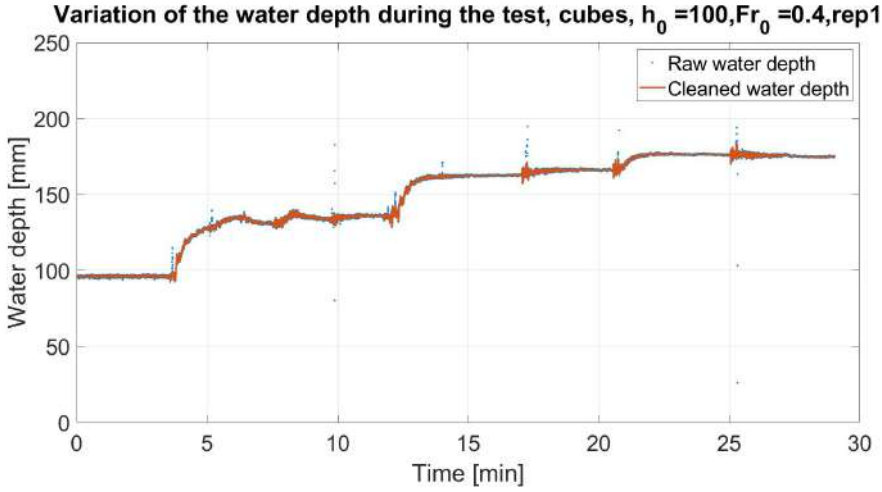

Figure 35: Raw and cleaned water depth during the test $C021\_1p$.

Part III
Results

7 Backwater rise

7.1 Observations

One typical test is represented in the figure 36 with the pictures taken by the side view camera. This is the first repetition of the test with an initial water level of 200 mm and an initial Froude number of 0.4 ($C51\_1p$). The first image (fig. 36a) shows the initial flow without blockage. The five next images ((fig. 36b, 36c, 36d, 36e and 36f) correspond to the accumulations resulting from the successive additions of 5 batches of debris to the flow.

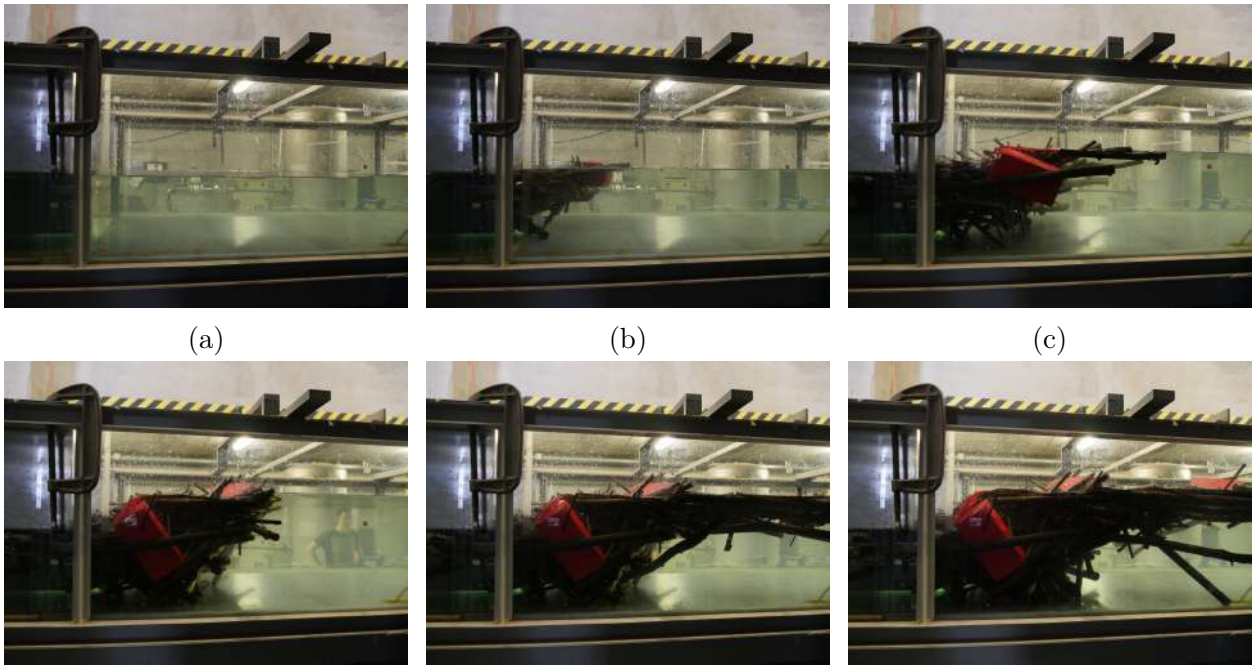

(a) (b) (c)

(d) (e) (f)

Figure 36: Illustration of a typical test, side view ($h_0 = 200mm$, $Fr_0 = 0.4$, cubes, 1 pier).

The first observation is that the water level increases with the volume of debris accumulated at the bridge. The first batch causes a more significant backwater rise than the next ones.

During the tests, when launching the first batch, a lot of debris pass the bridge and do not get clogged. Therefore, volumes that are re-launched are significant. The figure 37 shows the volume of debris that passed the bridge after the launch of the first batch during the test $C51\_1p$.

Figure 37: Volume of debris that passed the bridge after the launch of the first batch during the test $C51\_1p$ ($h_0 = 200mm$, $Fr_0 = 0.4$)

For the highest Froude numbers, the entire first batch sometimes needs to be relaunched or the first two batches need to be launched together in order to create an accumulation. Once the first logs get clogged, less and less debris passes the bridge until they do not pass at all.

For the last configuration ($Fr_0 = 0.2$ and $h_0 = 375mm$), no accumulation could be formed at all. Indeed, the entire batch of debris passed over the bridge deck without any signed of blockage. Thus, no results are available for this configuration.

7.2 Curve appearance

For all the tests mentioned in the table 15, the evolution of the water depth during the test can be represented. In the figure 38, the water depth evolution during the test for an initial water depth of $h_0 = 200mm$ and an initial Froude number of $Fr_0 = 0.60$ ($C62\_1p$) is represented.

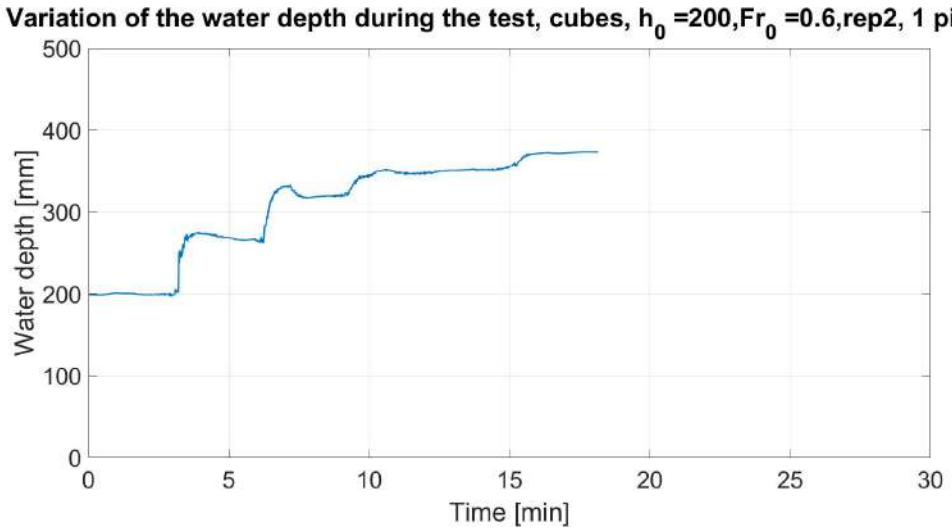

Figure 38: Variation of the water depth during the test $C62\_1p$ ($h_0 = 200mm$, $Fr_0 = 0.60$, cubes, 1 pier).

Visual observations made in the laboratory are confirmed by the data collected. Indeed, the water depth is increasing during the test. The graphs take the form of a staircase. Every step corresponds to the addition of one batch of debris, which is why five steps are visible.

The steps are smaller at the end of the test than at the beginning which means that the water level increase is greater for the first batches than for the last ones. Eventually, water depth reaches a plateau and hardly increases at all.

For every test, the times at which batches are launched are known. For example, the launching times for every batch during the test $C62\_1p$ are presented in table 17.

Table 17: Launching times of batches during the test $C62\_1p$ ($h_0 = 200mm$, $Fr_0 = 0.60$, cubes, 1 pier).

# batch	Time [min]	Cumulated volume [dm^3]
1	3	10.8
2	6	21.6
3	9	32.3
4	12	42.6
5	15	50.7
End time	18	

With these data, the x-axis can be converted from time (in minutes) to volume (in dm^3). In addition, the y-axis can also be converted from the absolute water depth to the backwater rise

$\Delta h = h - h_0$, since it is the increase in water level that is of interest, not the absolute height. The result of these changes, applied to figure 38, is represented in the figure 39.

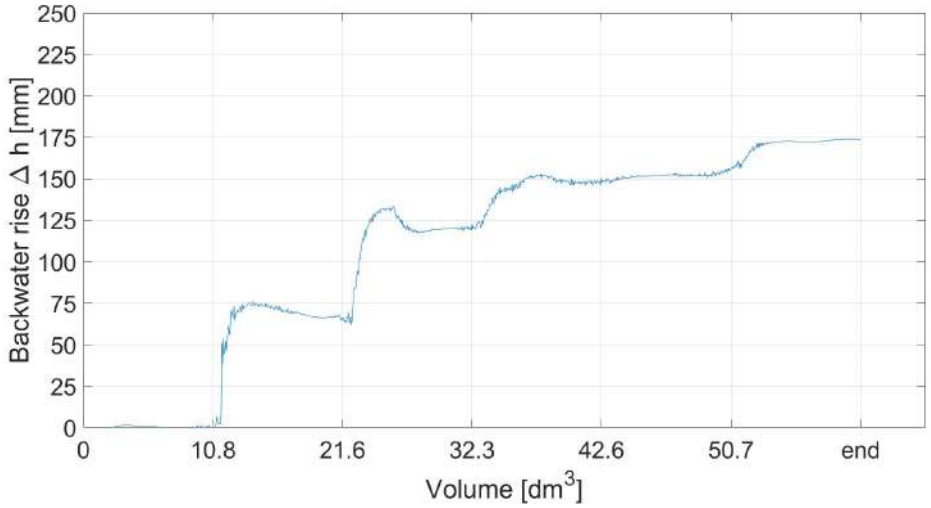

Figure 39: Variation of the backwater rise during the test $C62\_1p$ ($h_0 = 200mm$, $Fr_0 = 0.60$, cubes, 1 pier).

Thanks to this format, it can be confirmed that the steps of water depth correspond indeed to the addition of the 5 batches of debris.

In the following, graphs will be presented in this form.

7.3 Repeatability

During the Phase 1 of the project, it was determined that 3 repetitions of each test were sufficient to obtain representative data. In this phase (Phase 2), the first tests were also repeated 3 times. Their range of variation is 10% around the average as shown in the figure 40.

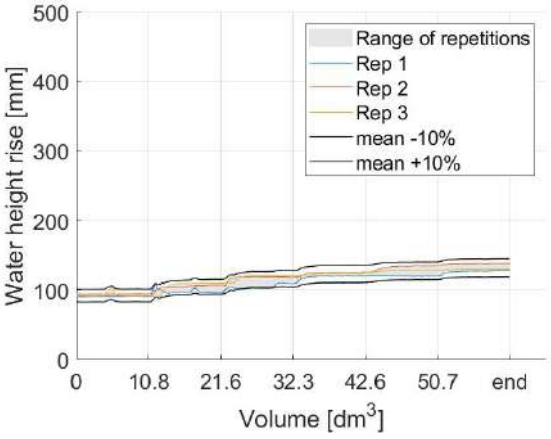

(a) $Fr_0 = 0.27$

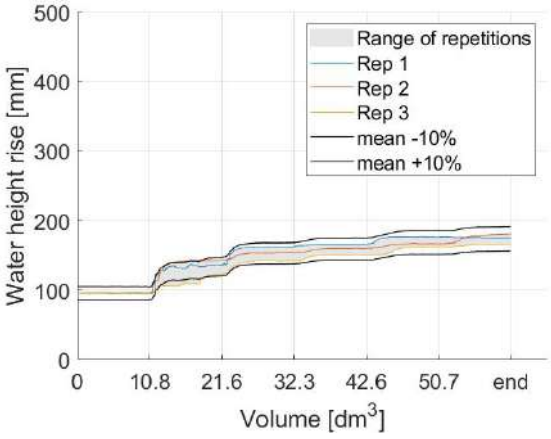

(b) $Fr_0 = 0.40$

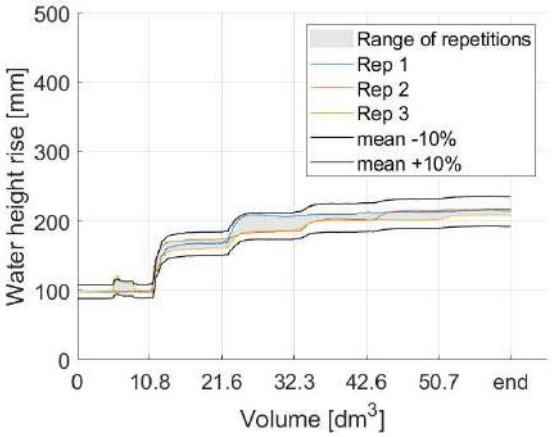

(c) $Fr_0 = 0.60$

Figure 40: Water height according to the added volume, for the tests with cubes and 1 pier, $h_0 = 100mm$.

When repeating the tests only twice, this range is also respected, and this for the 2 bridge geometries and the 2 debris compositions.(see fig. 41). For that reason, the number of repetitions was change from three to two per test.

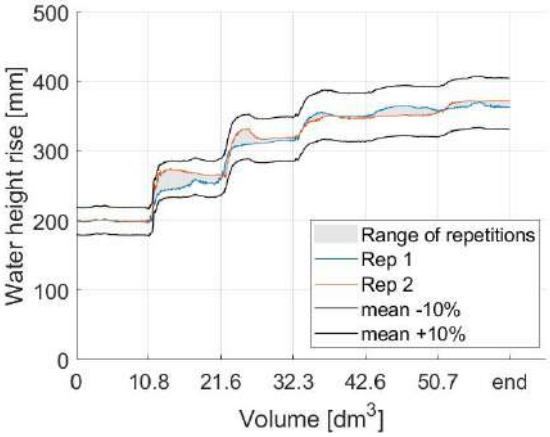

(a) $h_0 = 200mm, Fr_0 = 0.60$, cubes, 1 pier.

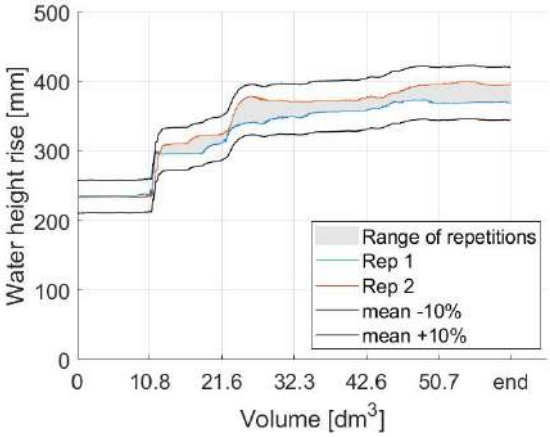

(b) $h_0 = 240mm, Fr_0 = 0.40$, plates, 1 pier.

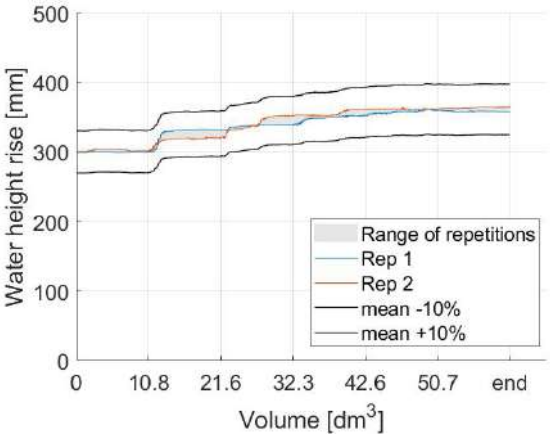

(c) $h_0 = 310mm, Fr_0 = 0.27$, cubes, 2 piers.

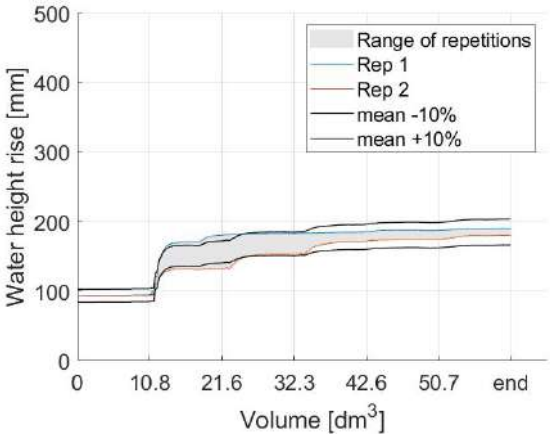

(d) $h_0 = 100mm, Fr_0 = 0.40$, plates, 2 piers.

Figure 41: Water height according to the added volume, for tests with 2 repetitions.

7.4 Average of repetitions

Once all the repetitions have been completed, they were combined to form an average for each test. This makes graphs easier to read and data analysis simpler. An example of this simplification for the tests with cubes, 1 pier and initial water depth of 240 mm is shown in the figure 42.

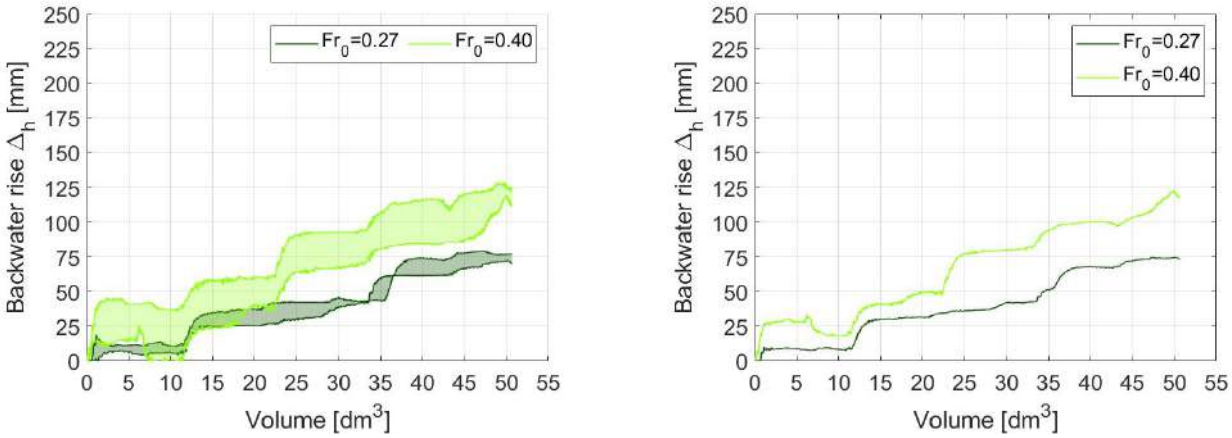

(a) Repetitions.

(b) Means.

Figure 42: Backwater rise according to the added volume, cubes, $h_0 = 240mm$, 1 pier
Comparison between the graph of the repetitions and the mean.

7.5 Effect of the parameters

The parameters that vary in this study are the debris composition (75% logs and 25% cubes or 75% logs and 25% plates), the flow conditions (initial water depth h_0 and initial Froude number Fr_0) and the geometry of the bridge (one or two piers).

7.5.1 Debris composition and bridge geometry

On figure 43, the tests for which the initial flow conditions are $h_0 = 200m$ and $Fr_0 = 0.40$ are compared. It is clear that debris mixtures including plates generate higher backwater rises than debris mixtures including cubes.

The influence of bridge geometry is unclear at this stage of the analysis.

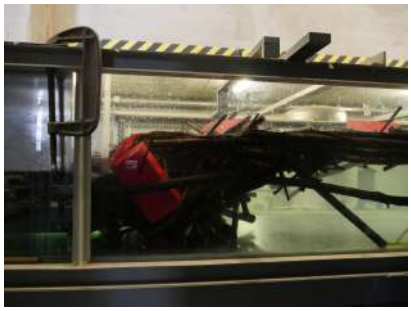

(a) 1 pier, cubes.

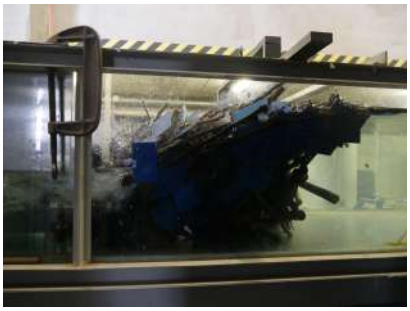

(b) 1 pier, plates.

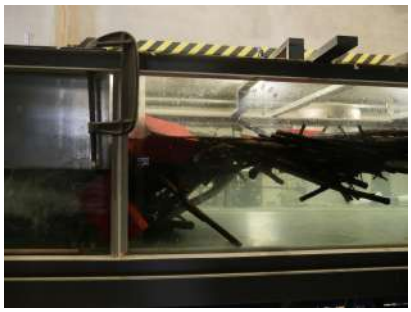

(c) 2 piers, cubes.

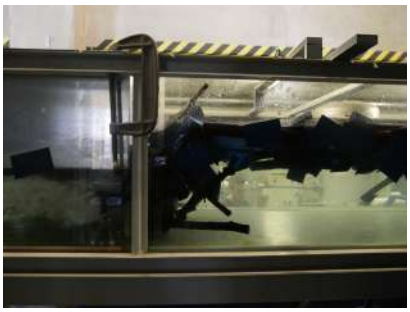

(d) 2 piers, plates.

Figure 43: Comparison of the backwater rise for identical initial hydraulic conditions and variable bridge geometry and debris mixture.

7.5.2 Froude number

Also, the backwater rise increases with the Froude number. Indeed, in the figure 44, 3 tests with one pier, cubes as debris and an initial water depth $h_0 = 200mm$ are compared ($Fr_0 = 0.27$, $Fr_0 = 0.40$, $Fr_0 = 0.60$). It is clear that, even with the same initial water depth, the final water depth is greater for the highest Froude numbers ($Fr_0 = 0.60$).

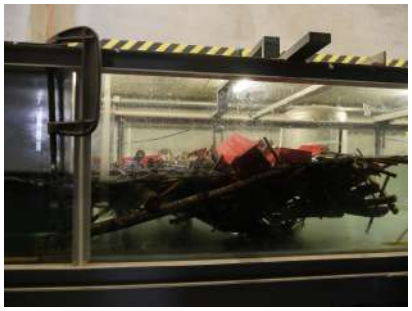

(a) $Fr_0 = 0.27$

(b) $Fr_0 = 0.40$

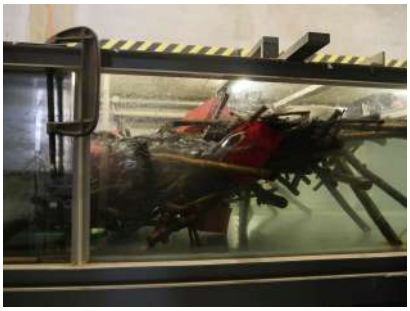

(c) $Fr_0 = 0.60$

Figure 44: Comparison of the backwater rise for the test with $h_0 = 200mm$.

This observation can be made for every initial water depths for which different Froude numbers are tested ($h_0 = 100, 200$ and 240 mm).

8 Accumulation shape

It can be observed that debris first accumulates vertically, along the pier(s). Then, when the flow section is entirely clogged, they accumulate horizontally and form a floating carpet (fig. 36).

As a result, the length of the accumulation increases slightly with the first batches and greatly with the last ones (see fig. 45).

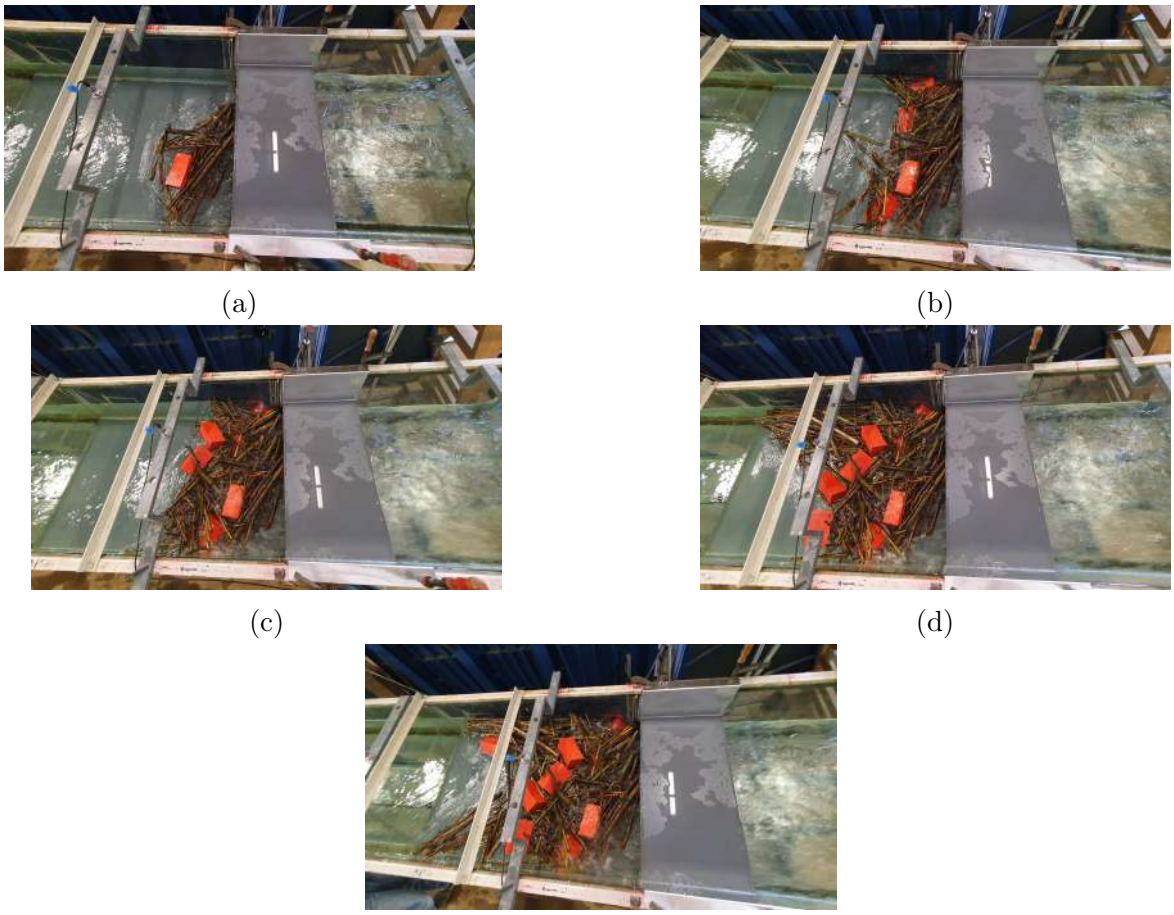

(a) (b) (c) (d) (e)

Figure 45: Illustration of a typical test, top view ($C51\_1p$).

These observations are consistent with what has been observed previously by Schmocker and Hager, 2013.

8.1 Effect of the parameters

8.1.1 Debris composition and bridge geometry

On figure 46, the tests for which the initial flow conditions are $h_0 = 100m$ and $F_{r0} = 0.27$ are compared but this time from the top view. It can be seen that debris mixtures including plates accumulate more compactly than debris mixtures including cubes. But the accumulation length is greater for mixture with plates than with cubes.

The influence of bridge geometry is again unclear at this stage of the analysis.

(a) 1 pier, cubes.

(b) 1 pier, plates.

(c) 2 piers, cubes.

(d) 2 piers, plates.

Figure 46: Comparison of the accumulation lengths for identical initial hydraulic conditions and variable bridge geometry and debris mixture.

8.1.2 Froude number

Contrary to the backwater rise, the accumulation length decreases with the Froude number. Indeed, in the figure 47, the same 3 tests presented in the figure 44 are compared ($h_0 = 200mm$ and $Fr_0 = 0.27$, $Fr_0 = 0.40$, $Fr_0 = 0.60$). It is clear that, even with the same initial water depth, the accumulation is shorter for the highest Froude numbers ($Fr_0 = 0.60$).

(a) $Fr_0 = 0.27$

(b) $Fr_0 = 0.40$

(c) $Fr_0 = 0.60$

Figure 47: Comparison of the backwater rises for the tests with $h_0 = 200mm$.

This observation can be made for every initial water depths for which different Froude numbers are tested ($h_0 = 100, 200$ and $240mm$).

Part IV
Discussions

9 Accumulation length L_{acc}

The accumulation lengths of all the tests performed are represented at the figure 48. The different subfigures correspond to different initial water depths ($h_0 = 100mm$: fig 48a, $h_0 = 200mm$: fig 48b, $h_0 = 240mm$: fig 48c, $h_0 = 310mm$: fig 48d).

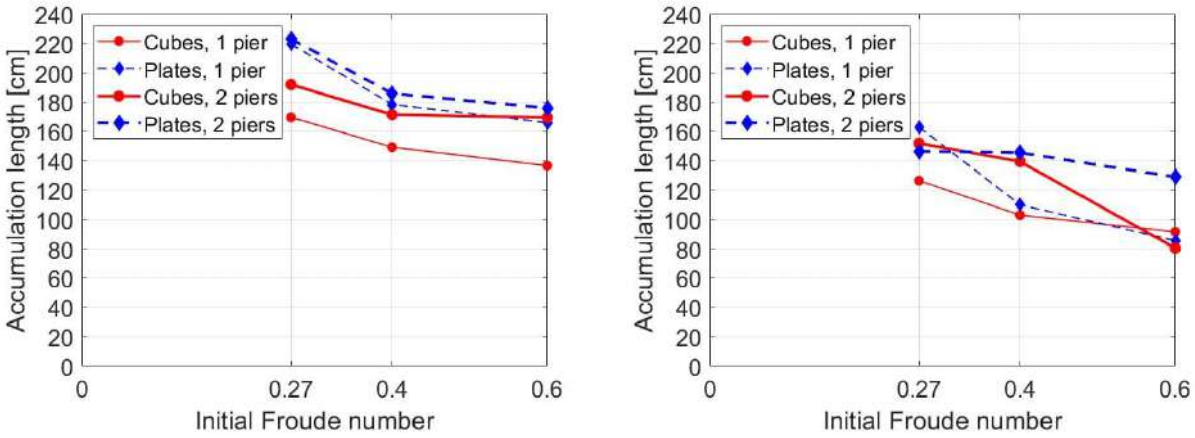

(a) $h_0 = 100mm$ (b) $h_0 = 200mm$

(c) $h_0 = 240mm$ (d) $h_0 = 310mm$

Figure 48: Comparison of the accumulation lengths for the four initial water depths tested.

9.1 Effect of the parameters on L_{acc}

9.1.1 Geometry of the bridge

The accumulation length may be compared for the two investigated bridges, the first one with a single central pier and the second with 2 piers.
The figure 48 shows that accumulation is longer when the bridge has two piers (thicker lines) than when the bridge has only one pier (thinner lines). This can be explained by the fact that with one pier, a part of the accumulation is under the bridge. Indeed, the longest logs accumulate in the pile diagonally to the axis of the channel. Consequently, some debris are

blocked by these diagonal logs under the bridge and the carpet length is shorter as it is measured from the upstream end of the deck.

9.1.2 Mixture

It is clear in the figure 48 that mixture with 25 % plates (dashed blue lines) generate longer accumulations than mixture with 25% cubes (solid red lines). This difference may be explained by the fact that 1 cube corresponds to dozens of plates in terms of volume. But when considering surface area, plates have a significantly larger material surface. Consequently, when it comes to the carpet formation, the plates, that can positioned vertically, horizontally or anyhow in between, take up more space than cubes, resulting in longer accumulations.

9.1.3 Initial water depth h_0

In the figure 49, all initial water depth are compared on the same graph.

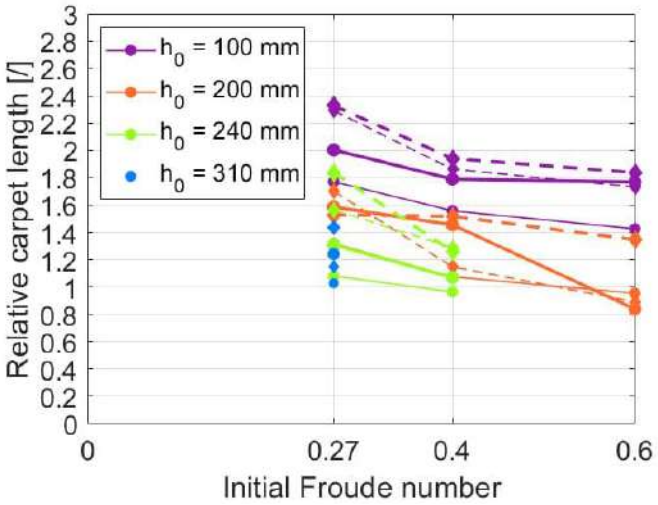

Figure 49: Relative carpet length according to the initial Froude number Fr_0 for each initial water depth h_0.

It is clear that the smallest water depth ($h_0 = 100mm$, in purple in fig. 49) generates the longest accumulations. Then, the distinction between $h_0 = 200mm$, $h_0 = 240mm$ and $h_0 = 310mm$ is not so clear. It seems that higher h_0 values result in shorter accumulation lengths, but the distinction is not sharp enough to draw any conclusions. Longer accumulations at the smallest water depth could be explained by a limitation of the vertical development of the accumulation due to the limitation by the flume bottom. So it can only develop horizontally leading to longer accumulations for a given debris volume.

9.1.4 Initial Froude number Fr_0

As observed in the section 8.1.2, the greater the Froude number, the shorter the accumulation.

This observation is similar to those of Schmocker and Hager, 2013 did. In the figure 50, the fit equation for the relative carpet length (eq. 7) is compared to the relative carpet length measured as part of this project.

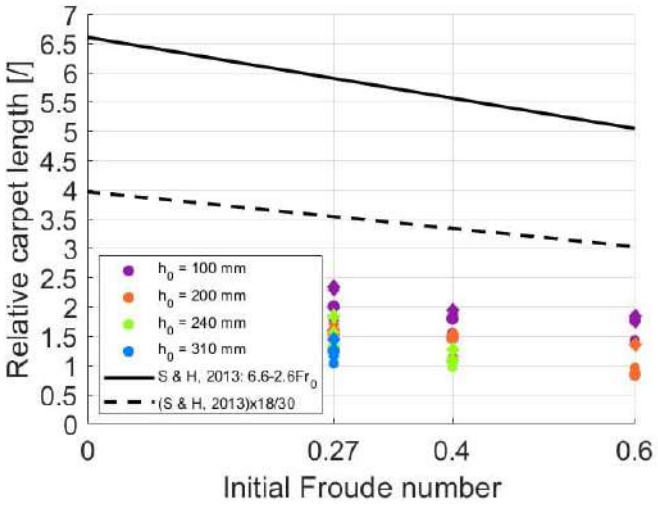

Figure 50: Comparison of the fit equation for the relative carpet length of Schmocker and Hager, 2013 and the scaled fit equation with the data set from this project.

Although the slope seems to agree, it is clear that the accumulation lengths are smaller in our case. This can be partly explained by the quantity of wood added to the flow. Indeed, Schmocker and Hager used $50dm^3$ of logs in a $\approx$ 1:30 scale model which corresponds to $1500m^3$ of wood at 1:1 scale. In this project, $50dm^3$ of debris were used in a 1:18 scale model which correspond to $900dm^3$ of debris. It is trivial that fewer debris cause smaller accumulations. But when scaling this fit equation to the scale of this project, the scaled fit equation (dashed black line in the figure 50) is still higher than the experimental accumulation length.

Other explanations could be the difference in the range of Froude numbers and the difference of debris mixture composition. Indeed, Schmocker and Hager's Froude number values are slightly higher than those tested ($0.5 < Fr_0o < 1.5$ for Schmocker and Hager, 2013 versus $0.27 \leq Fr_0 \leq 0.6$ in this project).
Next, although Schmocker and Hager included different types of mixtures, they only used logs. Cubes and plates could be a reason why the accumulation are smaller since it was observed that a difference in mixture influences this parameter.

The influence of the Froude number on the accumulation length thus also depends on supplementary parameters.

9.2 Fit equations

Fit equations can be determined to correlate the experimental data with the Froude number (see fig. 51 and eq. 17). The choice is made to separate each initial water depth and each mixture. The difference between the accumulation lengths for 1 and 2 piers are considered small enough to determine one fit equation for both geometries. This leads to 6 fit equations. As only one Froude number value is tested for $h_0 = 310mm$, it is not possible to fit any equation for this water depth.

$$\frac{L_{acc}}{B} = 2.07 - 0.84Fr_0 \text{ for } h_0 = 100mm, \text{cubes} \tag{17a}$$

$$\frac{L_{acc}}{B} = 2.64 - 1.50Fr_0 \text{ for } h_0 = 100mm, \text{plates} \tag{17b}$$

$$\frac{L_{acc}}{B} = 1.92 - 1.70Fr_0 \text{ for } h_0 = 200mm, \text{cubes} \tag{17c}$$

$$\frac{L_{acc}}{B} = 1.98 - 1.47Fr_0 \text{ for } h_0 = 200mm, \text{plates} \tag{17d}$$

$$\frac{L_{acc}}{B} = 1.56 - 1.37Fr_0 \text{ for } h_0 = 240mm, \text{cubes} \tag{17e}$$

$$\frac{L_{acc}}{B} = 2.58 - 3.27Fr_0 \text{ for } h_0 = 240mm, \text{plates} \tag{17f}$$

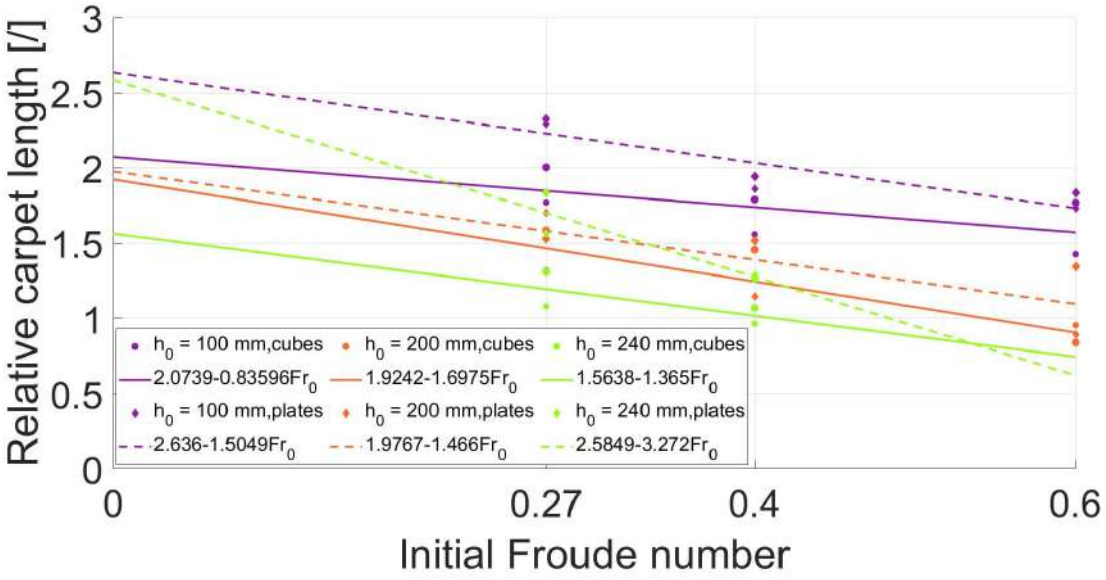

Figure 51: Fit equations for the relative carpet length for each initial water depth h_0 and each mixture (25% cubes or 25% plates).

10 Backwater rise Δh

The backwater rises according to the volume of debris clogged at the bridge are represented on figure 52 for all the conditions tested. The figures 52a and 52b show the results for the bridge with one pier for the mixture with cubes and plates, respectively. The figure 52c and 52c show the results for the bridge with two piers for the mixture with cubes and plates, respectively.

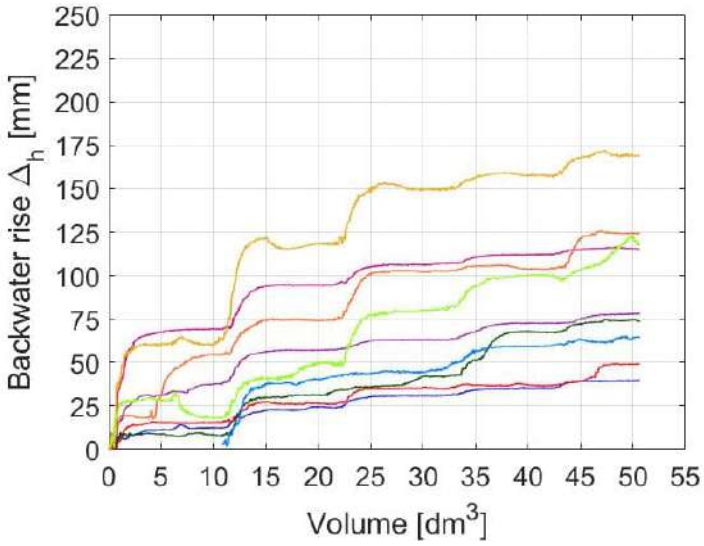

(a) Cubes, 1 pier.

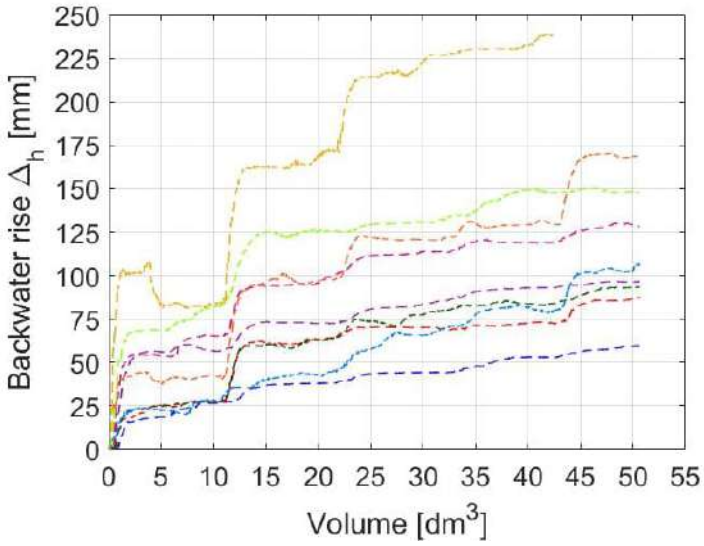

(b) Plates, 1 pier.

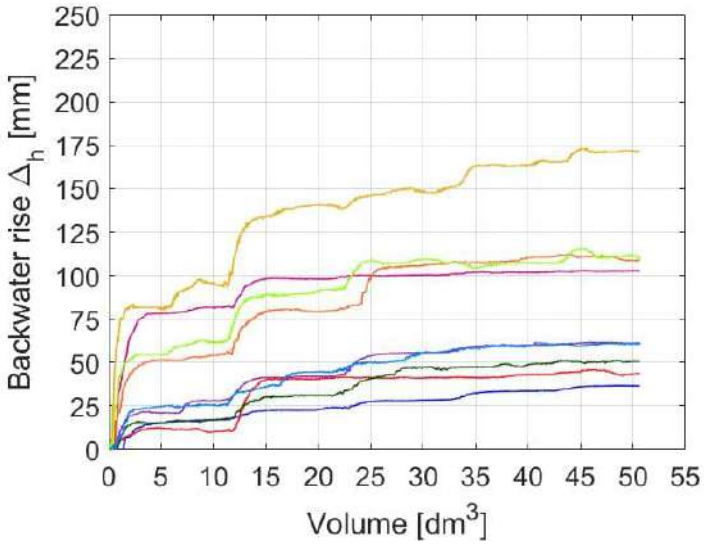

(c) Cubes, 2 piers.

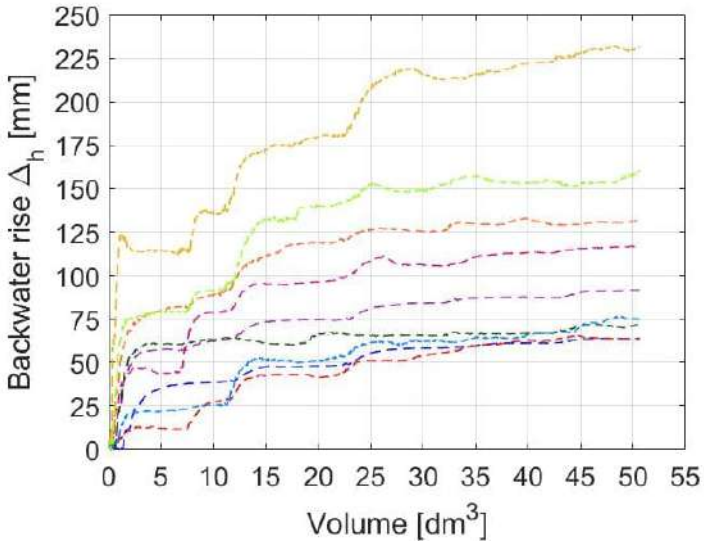

(d) Plates, 2 piers.

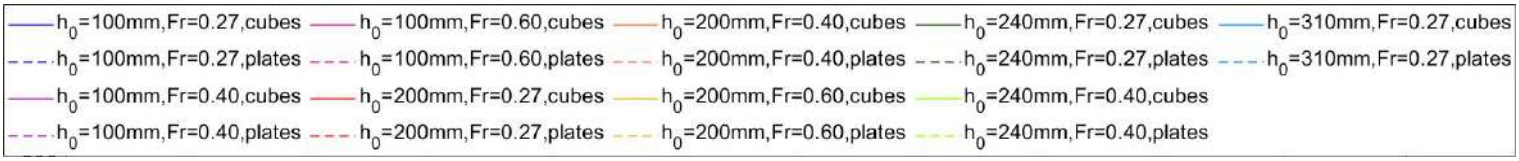

(e) Legend.

Figure 52: Backwater rise according to the volume of debris for all tests.

10.1 Effect of the parameters on Δh

10.1.1 Geometry of the bridge

In the figure 53, 3 representative configurations are presented to illustrate the influence of the number of piers on the backwater rise.

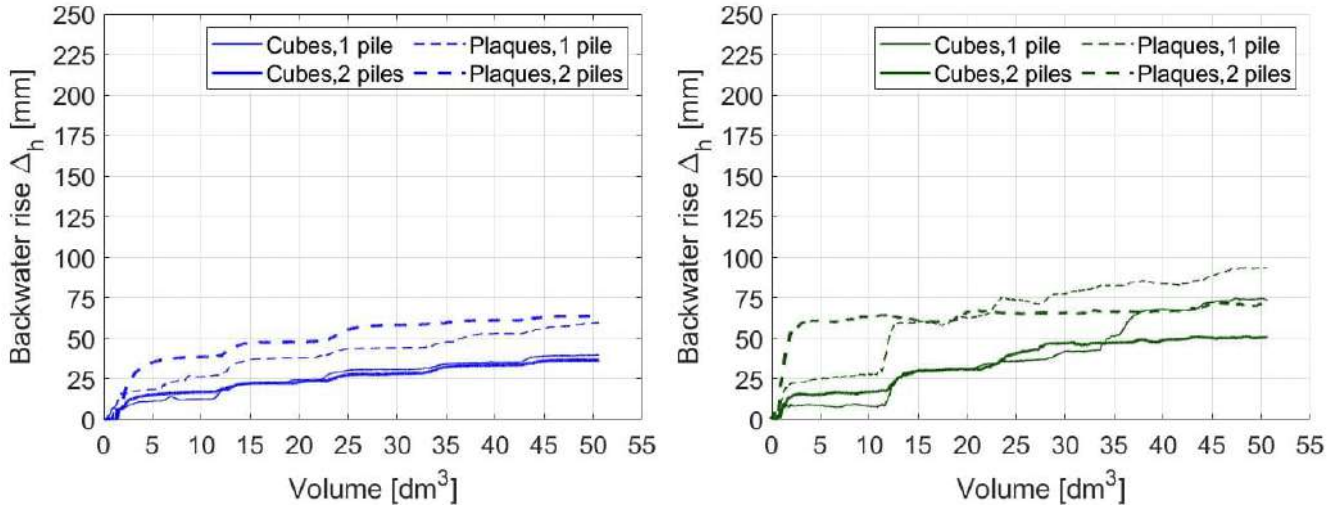

(a) $h_0 = 100mm$, $Fr_0 = 0.27$

(b) $h_0 = 240mm$, $Fr_0 = 0.27$

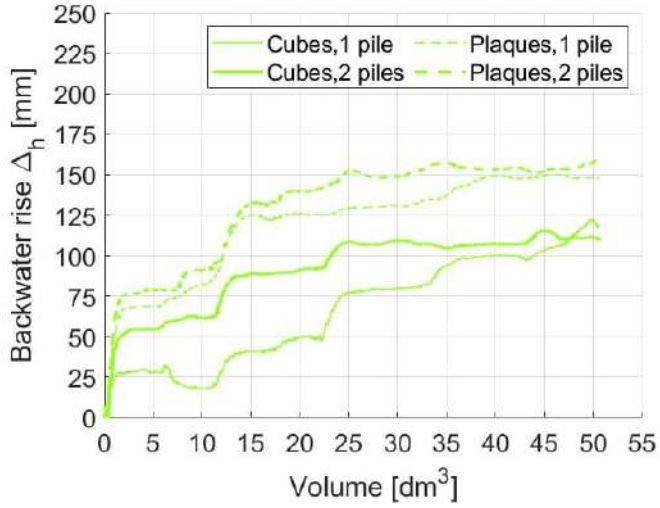

(c) $h_0 = 240mm$, $Fr_0 = 0.40$

Figure 53: Backwater rise according to the added volume for both mixture (25 % cubes and 25 % plates) and both geometries (1 and 2 piers) for 3 representative configurations.

These graphs (53a, 53b and 53c) show that the influence of the geometry varies.
Indeed, for the test with cubes, the final backwater rise with 2 piers is always smaller (fig. 53b) or equal (fig. 53a and 53c) than the one with 1 pier.
For the plates, the final backwater rise with 2 piers is either slightly greater (fig. 53a and 53c) either smaller (fig. 53b) than the one with 1 pier.

As a result, no definite conclusion can be drawn regarding the influence of the number of piers on the backwater rise.

10.1.2 Mixture

The figure 53 can also be used to analyze the influence of the debris mixture.
It is clear that the mixture with 25 % plates (dashed lines) generates higher backwater rise than the mixture with 25 % cubes (solid lines). This confirm what was observed in section 7.5.1.

This difference is explained by the fact that, due to their number and geometry, the plates seal the gaps between the logs better than the cubes. As a result, the accumulation has less porosity and prevents more water from passing through. Thus, the water level rises more.

10.1.3 Initial Froude number Fr_0

In figure 54, the backwater rise according to the added volume is represented separately for the initial water depths $h_0 = 100, 200, 240$ and 310 mm.
The first two h_0 (100 and 200 mm) are situated below the deck. For them, 3 Froude number could be tested (0.27, 0.4 and 0.6). The 240 mm water depth corresponds to the middle of the bridge deck, two Froude number could be tested for this depth (0.27 and 0.4). Lastly, the 310 mm water depth is situated 3 cm above the deck, only the smallest Froude number (0.27) could be reached in the laboratory for this depth (see fig. 30).

The influence of the Froude number observed in the section 7.5.2 is confirmed. The higher the Froude number, the higher the backwater rise.
This can be explained as follows. The Froude number depends on the velocity of the flume (eq. 18).

$$Fr = \frac{u}{\sqrt{gh}} \quad \text{in a flume with a rectangular cross-section} \tag{18}$$

With u the velocity of the flow and h the water depth.
The higher the flow velocity, the greater the head ($H = z + h + \frac{u^2}{2g}$ with z, the altitude of the bottom of the flume). The flow therefore has more energy. It compresses the accumulation against the pile(s) and deck. As the accumulation is denser, it allows less water to pass through, resulting in a greater backwater rise.

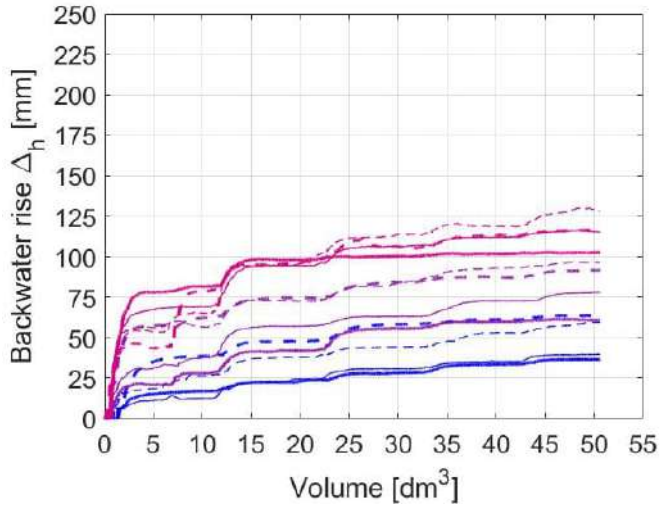

(a) $h_0 = 100mm$

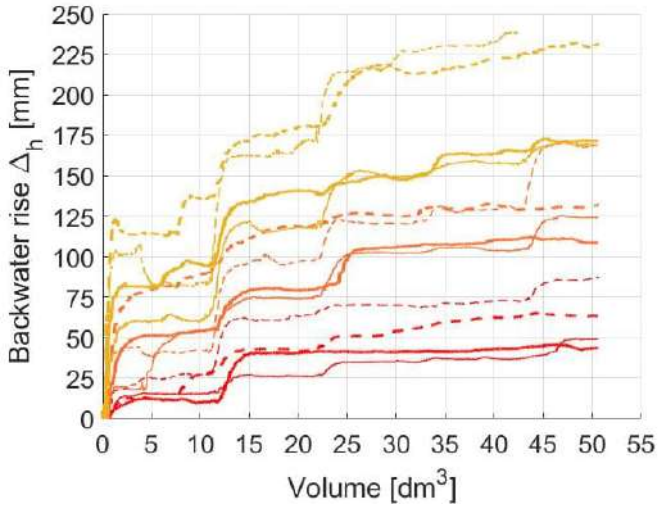

(b) $h_0 = 200mm$

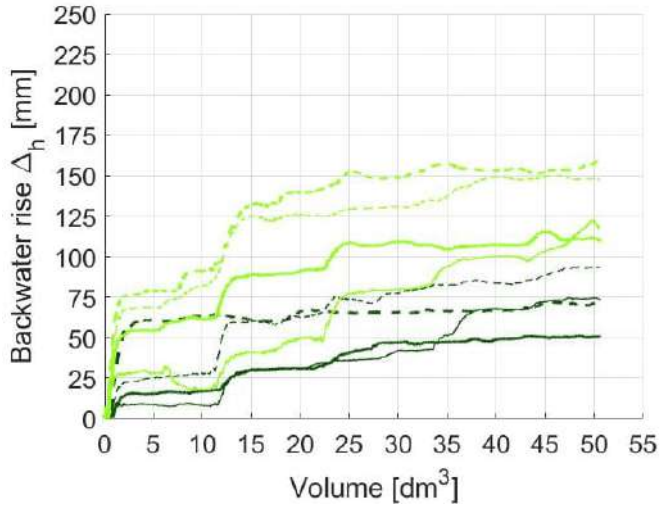

(c) $h_0 = 240mm$

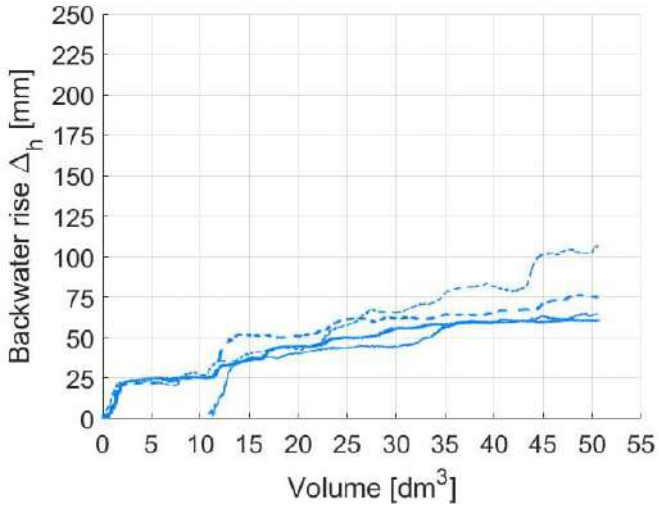

(d) $h_0 = 310mm$

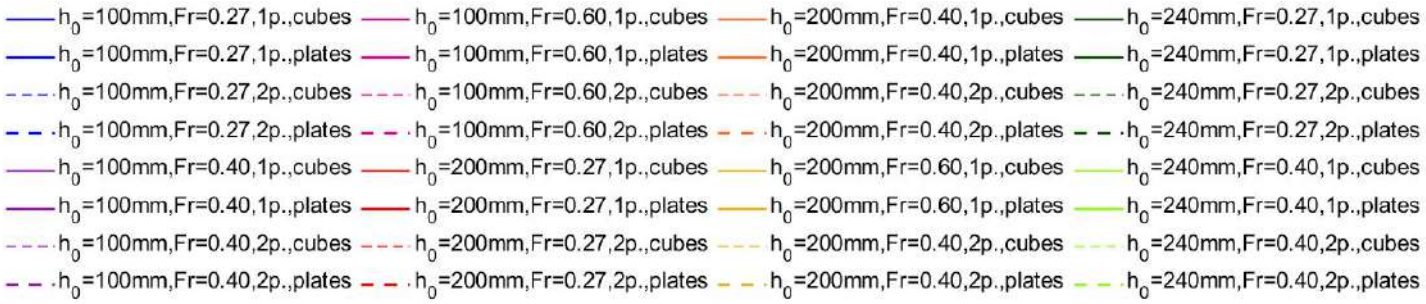

(e) Legend.

Figure 54: Backwater rise according to the added volume for both mixture (25 % cubes and 25 % plates) and both geometries (1 and 2 piers).

In the figure 55, the water depths at the end of each test, scaled by the initial water depth are represented according to the Froude number. They are compared to the fit equation for the relative flow depth (eq. 6) proposed by Schmocker and Hager, 2013.

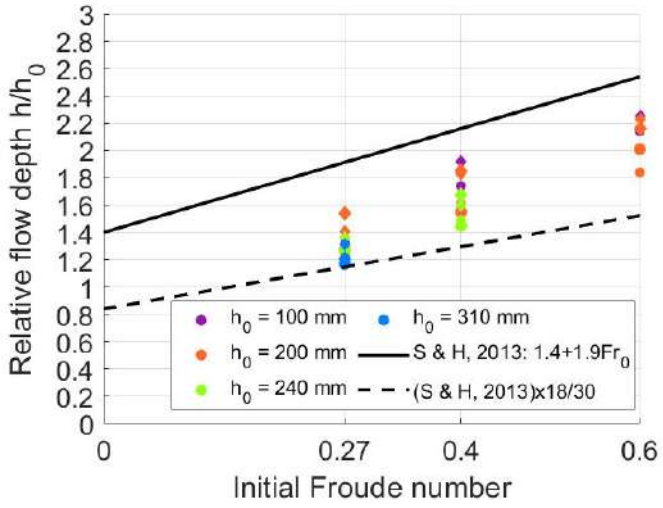

Figure 55: Comparison of the fit equation for the relative flow depth of Schmocker and Hager, 2013 and the scaled fit equation with the data set from this project.

The slope of the Schmocker and Hager, 2013 equation is similar to the one that could be fitted on the experimental data, but it is clear that the relative flow depths are smaller in the present case.
Once again (see section 9.1.4), this could be explained by the quantity of wood added to the flow. When scaling the fit equation of Schmocker and Hager, 2013 to the scale of the present project, the scaled fit equation passes under the experimental data.
In addition, it can be noted that the fit equation for the relative flow depth (fig.55 is closer to the experimental data than the fit equation for the relative carpet length (fig. 50).
This can be explained by the fact that once the accumulation process has reached the carpet formation phase (see fig.8), the water level rises less. Thus, even though Schmocker and Hager, 2013 used higher volume of debris, the water level eventually reaches a plateau that is not so far from the one reached in this project.

Fit equations

A linear equation relating the accumulation length to the Froude number may be fitted on experimental data. Since the results with both bridge geometries are very close to each other, it seems appropriate to find a common equation for each initial water level. First, the cubes and the plates are investigated separately, as it is known that they influence differently the water level (see fig. 56).

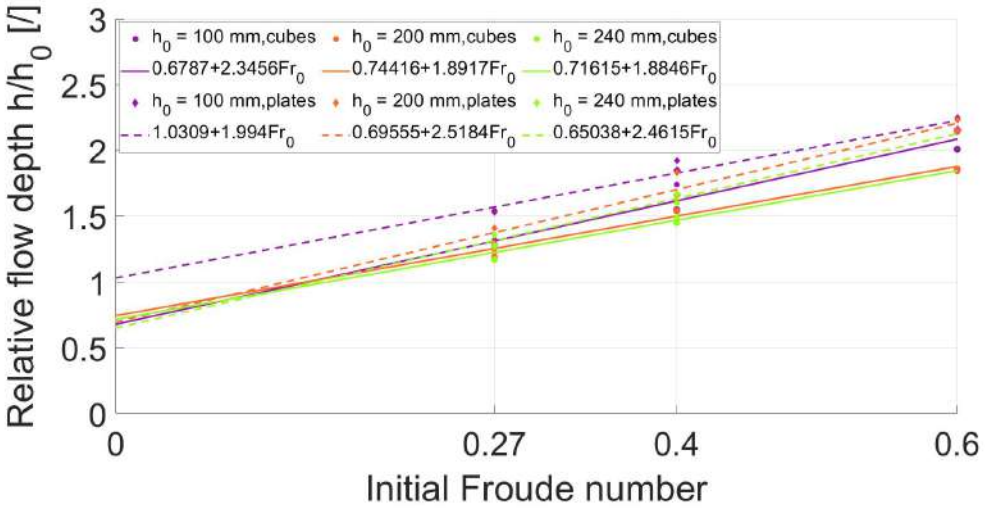

Figure 56: Fit equations for the relative carpet length for each initial water depth h_0 and each mixture (25% cubes or 25% plates).

By analyzing the figure 56, the choice is made to keep cubes and plates separated but to combine all initial water depths. This leads to 2 fit equations (see fig. 57 and eq. 19) that can be combined in one equation(eq.20). For a given debris volume, the water level at the end of a test can then be defined from the initial flow conditions (h_0 and Fr_0).

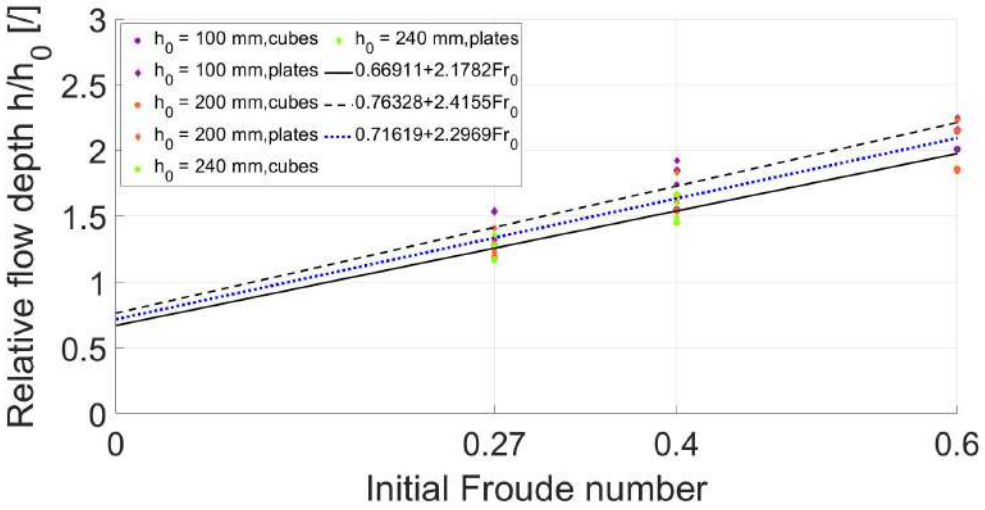

Figure 57: Fit equations for the relative carpet length for each initial water depth h_0 and each mixture (25% cubes or 25% plates).

$$\frac{h}{h_0} = 0.67 + 2.18Fr_0 \text{ for cubes} \tag{19a}$$

$$\frac{h}{h_0} = 0.76 + 2.42Fr_0 \text{ for plates} \tag{19b}$$

$$\frac{h}{h_0} = 0.72 + 2.3Fr_0 \tag{20}$$

10.1.4 Initial water depth h_0

In figure 58, the backwater rise according to the added volume is represented separately for the initial Froude number $Fr_0 = 0.27, 0.40$ and 0.60 in order to observe the influence of the initial water depth for a constant Froude number.

The influence of the water depth is not as clear as the influence of the Froude number.

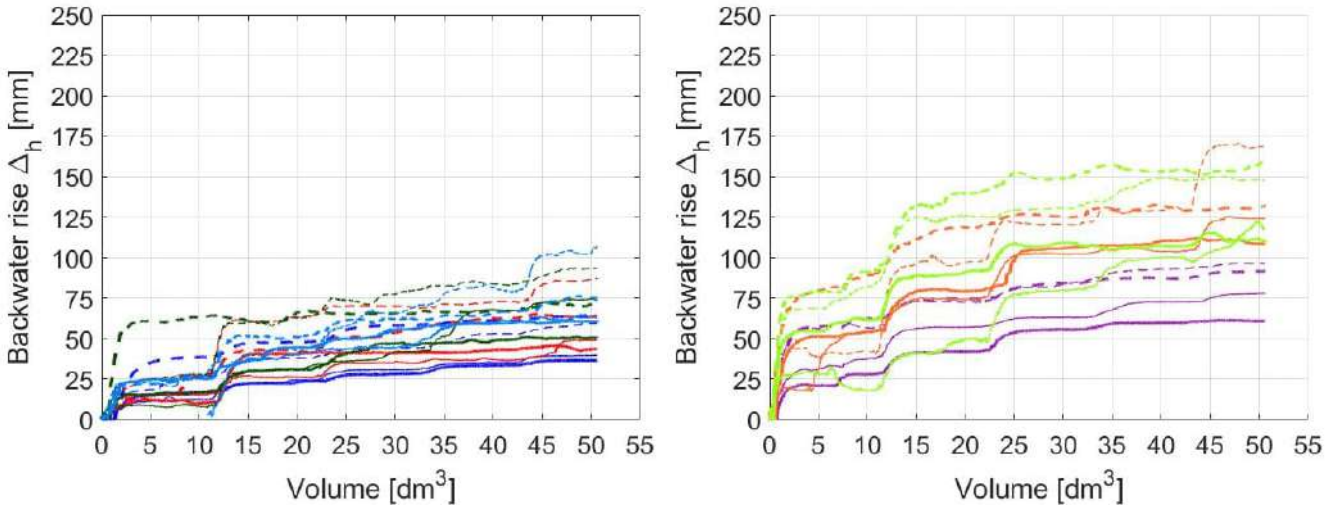

(a) $Fr_0 = 0.27$ (b) $Fr_0 = 0.40$

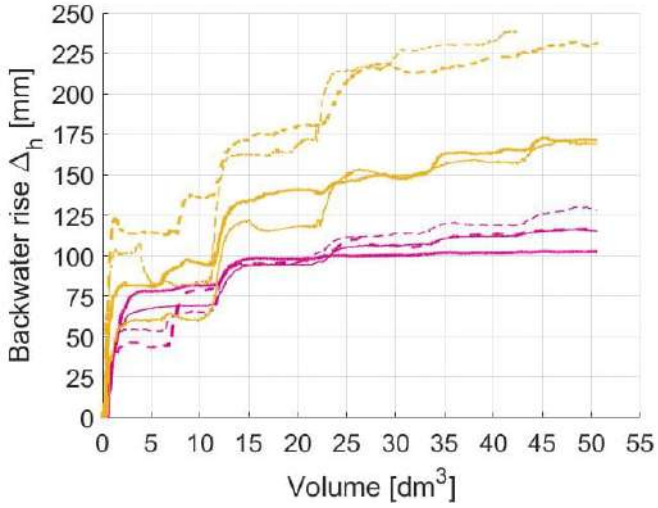

(c) $Fr_0 = 0.60$

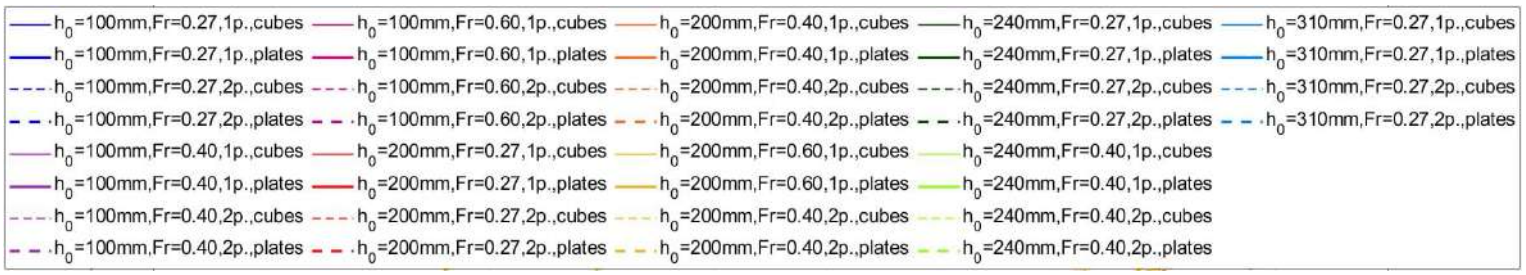

(d) Legend.

Figure 58: Backwater rise according to the added volume for both mixture (25 % cubes and 25 % plates) and both geometries (1 and 2 piers).

To get a clearer picture, the influence of the initial water depth is first analysed for initial water depths under the deck ($h_0 = 100mm$ and $h_0 = 200mm \leq h_{deck} = 210mm$).

In the figure 59, it is clear that, for all initial Froude numbers, the $h_0 = 200mm$ induces a bigger backwater rise than $h_0 = 100mm$. The difference becomes more pronounced as Froude number increases.

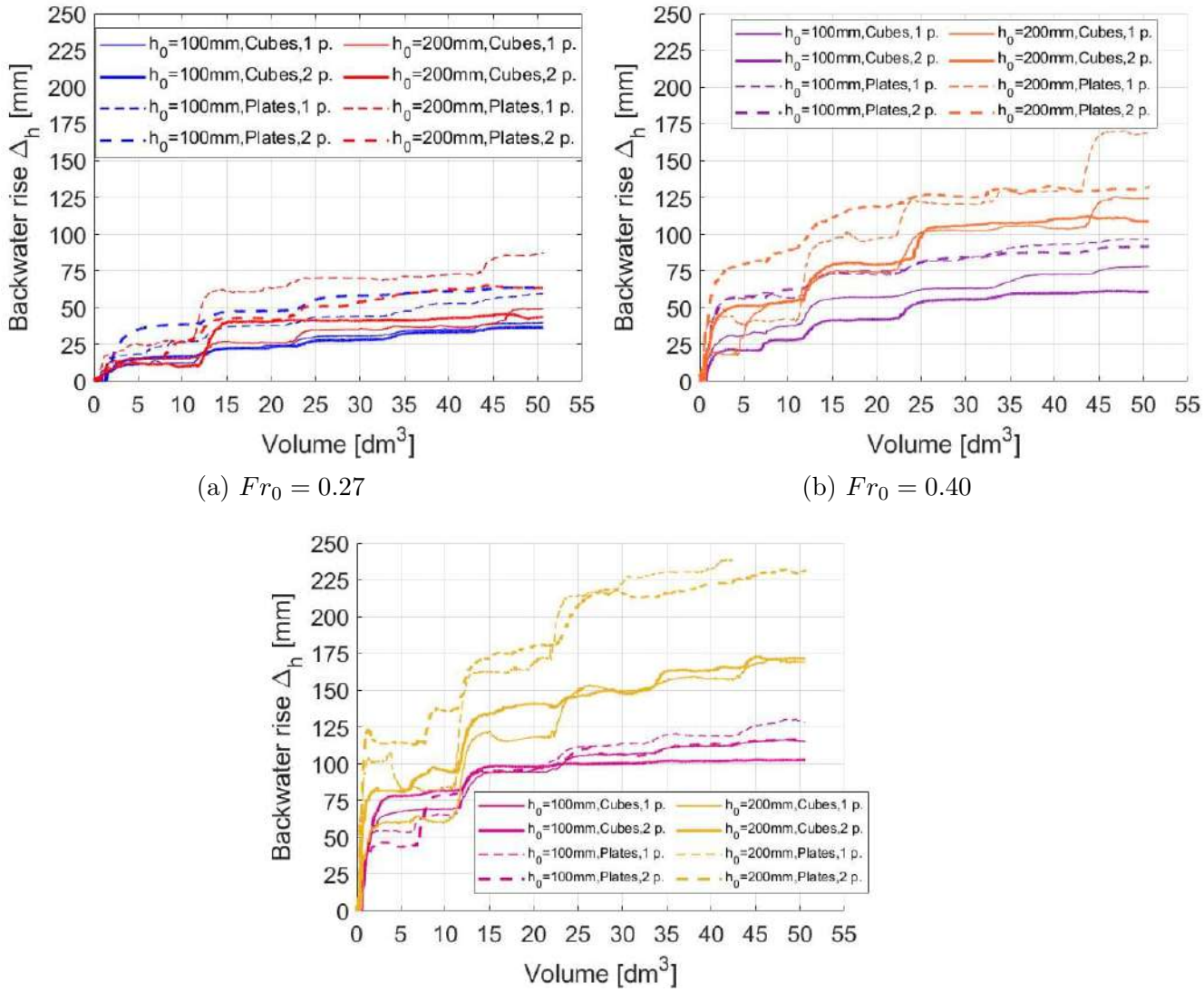

(a) $Fr_0 = 0.27$

(b) $Fr_0 = 0.40$

(c) $Fr_0 = 0.60$

Figure 59: Backwater rise according to the added volume for both mixture (25 % cubes and 25 % plates) and both geometries (1 and 2 piers) for h_0 under the deck.

For initial water depths at the deck ($h_0 = 240mm$) or over the deck ($h_0 = 310mm$), only experiments with a Froude number $Fr_0 = 0.27$ allow to observe an influence of h_0.
The figure 61 shows the backwater rise according to the added volume for $Fr_0 = 0.27$ and initial water depth $h_0 = 240mm$ and $310mm$.
In this case, the $h_0 = 310mm$ induces a bigger backwater rise than $h_0 = 240mm$ when the debris are composed of cubes, but the opposite is observed when the debris are composed of plates.

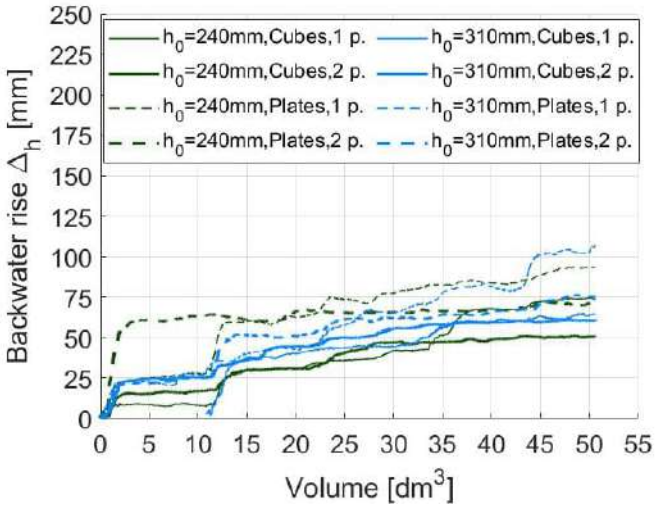

Figure 60: Backwater rise according to the added volume for both mixture (25 % cubes and 25 % plates) and both geometries (1 and 2 piers) for h_0 over the deck.

The bridge deck has thus an impact on the effect of the initial water depth as the trends observed for the smallest h_0 do not propagate when the initial water depth reaches the bridge deck.

11 Parameter fitting

11.1 Comparison to Schalko et al., 2019a

In Schalko et al., 2019a, a power law is fitted to the experimental data to correlate the backwater water rise to the volume of debris.

First, the backwater rise and the volume are made dimensionless. The backwater rise is divided by the initial water depth and the volume is divided by the width of the flume and the squared initial water depth. This gives a relationship such as:

$$\frac{\Delta h}{h_0} \propto \frac{V}{Bh_0^2}$$

Based on the results obtained, the hypothesis of a power law is being considered in order to derive an equation.

$$\frac{\Delta h}{h_0} = a\left(\frac{V}{Bh_0^2}\right)^b \tag{21}$$

For each of their tests, Schalko et al. altered the prefactors and exponents (a, b) to best fit the experimental data. Once a law is obtained for each test, the derivative of equation 21 is computed to express the relative change of $\frac{\Delta h}{h_0}$ as a function of $\frac{V}{Bh_0^2}$.
A characteristic volume is then determined as the volume for which the derivative falls below 10%. It corresponds to the primary and main backwater rise.

The figure 61 illustrates this procedure for 2 of the Schalko tests.

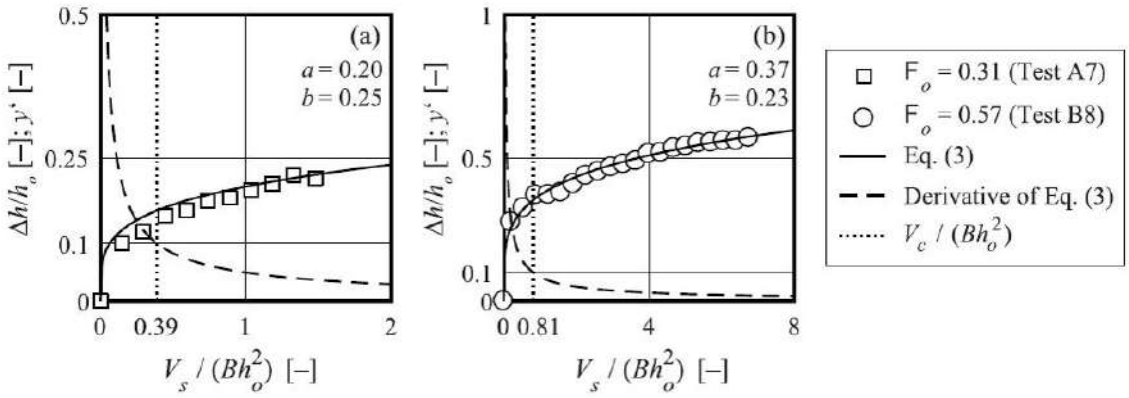

Figure 5. Relative backwater rise $\Delta h/h_o$ and derivative versus relative solid large wood volume $V_s/(Bh_o^2)$ with equation (3), derivative of equation (3), and relative characteristic large wood volume $V_c/(Bh_o^2)$ for test (a) A7 and (b) B8. Parameters a and b for equation (3) are included.

Figure 61: Schalko et al., 2019a fig. 5, Illustration of the procedure to obtain a characteristic volume (Eq. 3 from Schalko corresponds to eq. 21 from this work.

The Schalko test which is the closest to tests performed in the present work is the A1 test ($Fr_0 = 0.27$). The parameters **a** and in order to observe the influence of the initial water height for a constant Froude number. for this test are $a = 0.26$ and $b = 0.35$. In figure 62, this test A1 is compared to the tests with an initial Froude number of 0.27.

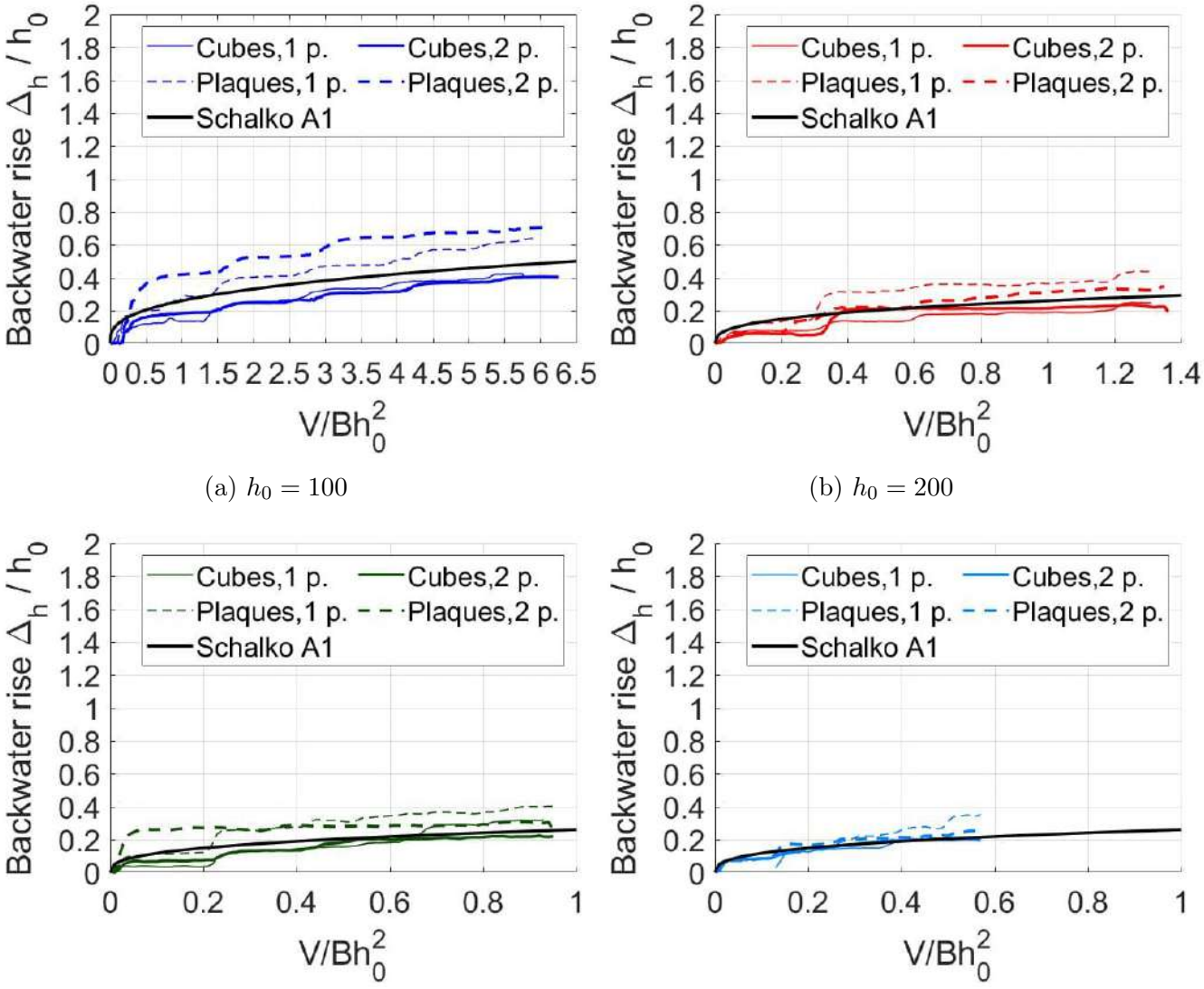

(a) $h_0 = 100$

(b) $h_0 = 200$

(c) $h_0 = 240$

(d) $h_0 = 310$

Figure 62: Comparison between Schalko et al. results and the test with initial Froude number $Fr_0 = 0.27$.

These results are comparable. Therefore, the same procedure should be applicable to the data from this project to obtain characteristic volumes as well.

11.2 Application to this project

11.2.1 Normalization of the results

Instead of dividing the debris volume by Bh_0^2, it is divided by the free section under the bridge (S_{free}, see fig. 63) multiplied by the initial water depth (h_0) in order to limit the influence of the initial water depth and to include the deck effect.
Thus, the form of the power law that is fitted on the experimental data is the following (eq. 22).

$$\frac{\Delta h}{h_0} = a \left(\frac{V}{S_{free} h_0} \right)^b \tag{22}$$

The computation of S_{free} is detailed in the figure 63.

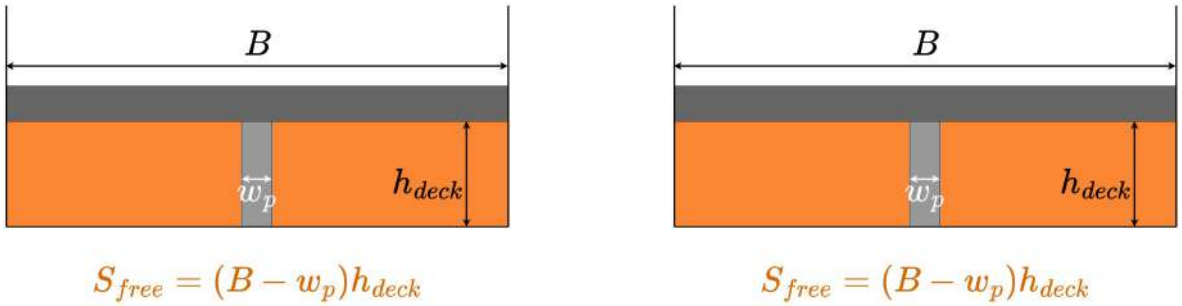

Figure 63: Free section under the bridge for the geometries with one and two piers.

In order to fit the power law to the experimental data, the latter are simplified to 6 points, corresponding to the initial water depth and to water depths measured after the additions of the 5 batches in the flow. The coordinate of each point is the volume of each batch (divided by $S_{free}h_0$ times $S_{free}h_0$) and the mean of the water depths registered during the minute before the addition of the next batch (minus h_0, to get the depth rise and then divided by h_0, to get a relative value).
This simplification is applied to every test. The points obtained for the tests with one pier, an initial water depth of 200 mm and both types of debris are presented in the figure 64.

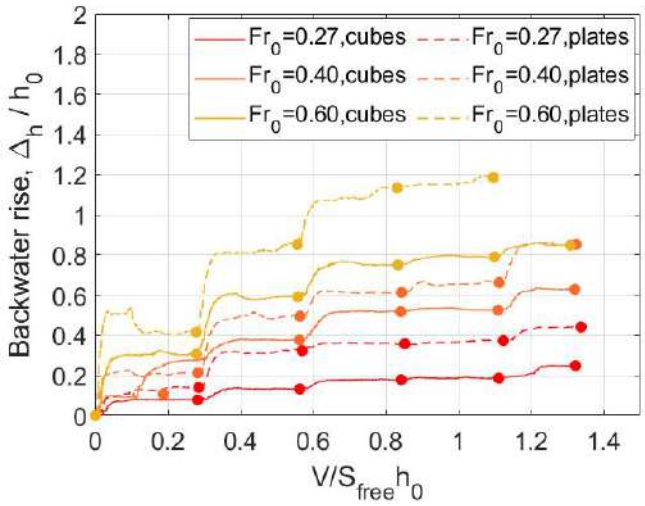

Figure 64: Relative backwater rise according to the dimensionless volume for the test with $h_0 = 200mm$, 1 pier and both mixtures, simplification in 6 points.

11.2.2 Power law fitting

Once each curve is replaced by its 6 points, the coefficients a and b are adjusted so that the power law best fits the data in terms of least squares.
In this way, some **a** and **b** values are obtained for each test (see tab. 18). Two examples for the configuration with $h_0 = 100mm$ and $Fr_0 = 0.27$ are shown at the figure 65.

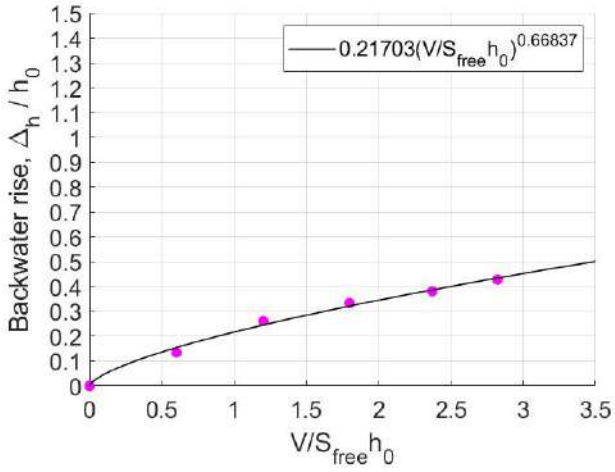

(a) $h_0 = 100$, $Fr_0 = 0.27$, cubes, 1 pier.

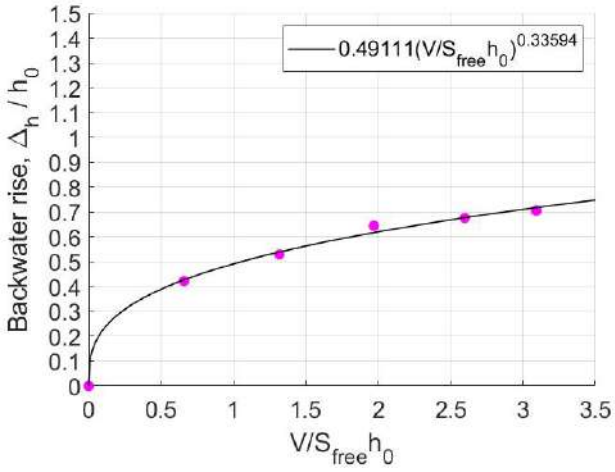

(b) $h_0 = 100$, $Fr_0 = 0.27$, plates, 2 piers.

Figure 65: Power law fitting.

Table 18: Fitted values of parameters a and b for every tests.

		Fr_0	0.27		0.40		0.60	
		h_0	a	b	a	b	a	b
1 pile	Cubes	100	0.22	0.67	0.52	0.44	0.89	0.32
		200	0.19	0.70	0.52	0.71	0.76	0.56
		240	0.29	1.19	0.46	1.08	/	/
		310	0.26	0.95	/	/	/	/
	Plates	100	0.37	0.52	0.72	0.35	0.90	0.40
		200	0.37	0.57	0.67	0.75	1.18	0.68
		240	0.39	0.63	0.63	0.35	/	/
		310	0.38	0.91	/	/	/	/
2 piles	Cubes	100	0.22	0.52	0.40	0.49	0.92	0.14
		200	0.20	0.54	0.51	0.45	0.77	0.34
		240	0.21	0.65	0.46	0.34	/	/
		310	0.22	0.50	/	/	/	/
	Plates	100	0.49	0.34	0.75	0.25	0.91	0.25
		200	0.28	0.56	0.63	0.24	1.06	0.33
		240	0.29	0.06	0.65	0.30	/	/
		310	0.27	0.59	/	/	/	/

It is possible to relate the fitted values of **a** and **b** coefficients relative to the different tests to the parameters of these tests (Fr_0,h_0, debris composition and number of piers).

11.2.3 Coefficient a

The parameters **a** for each test are represented in the figure 66 according to the Froude number for every water depths.
This figure shows that the coefficient **a** depends neither on the initial water depth, nor on the number of piers. On the other hand, it significantly depends on the debris composition : higher values of **a** are obtained for plates than for cubes. For all tests, the coefficient a linearly

increases with the Froude. One linear relation between **a** and Fr_0 is thus fitted for each debris mixtures (see fig.67a, fig.67b and eq. 23).

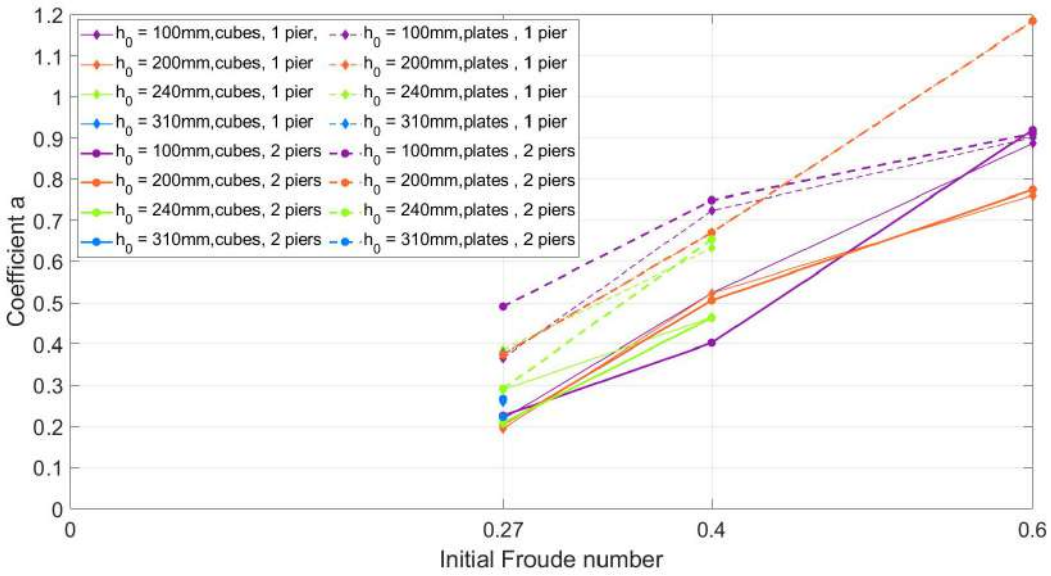

Figure 66: Coefficient **a** according to the Froude number for every h_0, debris mixture and bridge geometries.

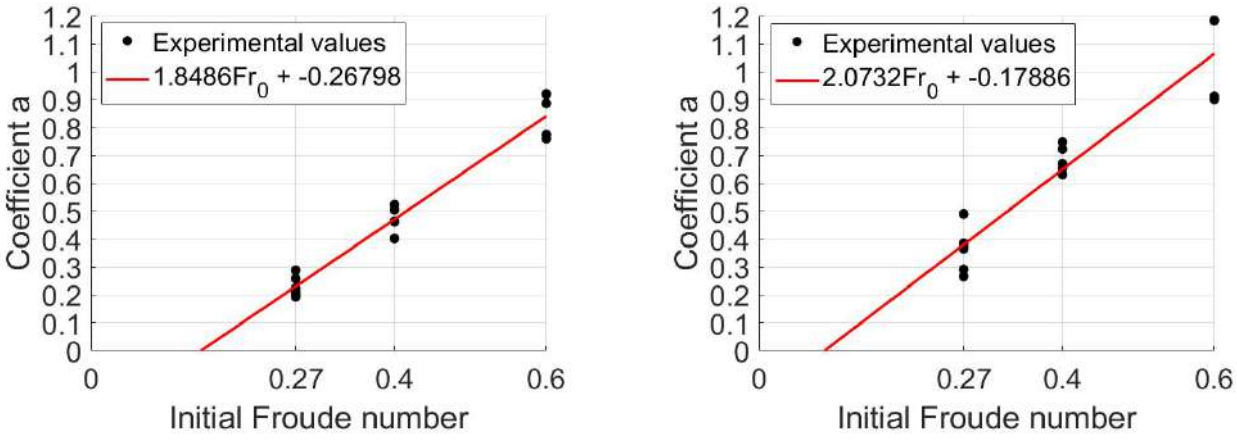

(a) Cubes.

(b) Plates.

Figure 67: Coefficient **a** according to the Froude number for every h_0 and bridge geometries.

$$a = 1.85Fr_0 - 0.27 \text{ for cubes} \tag{23a}$$

$$a = 2.07Fr_0 - 0.18 \text{ for plates} \tag{23b}$$

11.2.4 Coefficient b

The **b** parameter values for each test are represented in the figure 68 according to the Froude number for every water depths.
On the contrary to the **a** coefficient, the **b** coefficient does not seem to depend on the initial Froude number.

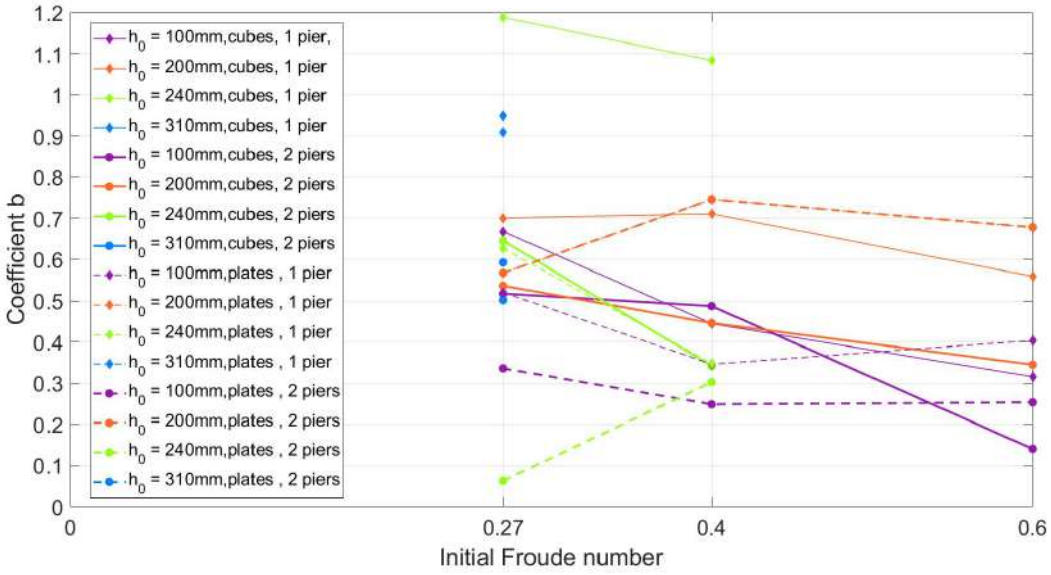

Figure 68: Coefficient **b** according to the Froude number for every h_0, debris mixture and bridge geometries.

Figure 69 presents the **b** parameter values for each test according to the initial water depth for every Froude numbers.

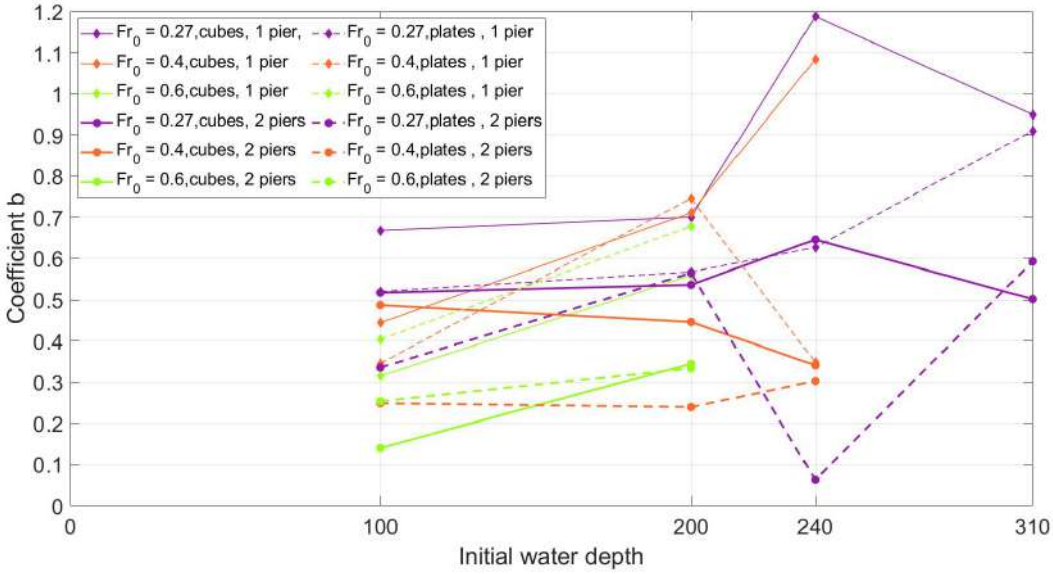

Figure 69: Coefficient **b** according to the initial water depth for every Fr_0, debris mixture and bridge geometries.

By analyzing both graphs (fig. 68 and fig. 69) and table 18, it appears that the fitted values of **b** are higher for debris mixture with cubes than with plates. They are also higher for a bridge with one pier than with 2 piers. But neither the Froude number nor the initial water depth seem to have a significant influence on the coefficient **b** value. The latter could thus be considered as constant for a given number of piers and a given debris composition. The mean of **b** values for both bridge geometries and debris compositions is then computed (see fig.70 and eq. 24). It leads to the following 4 values of **b** : one per bridge geometry and per debris composition.

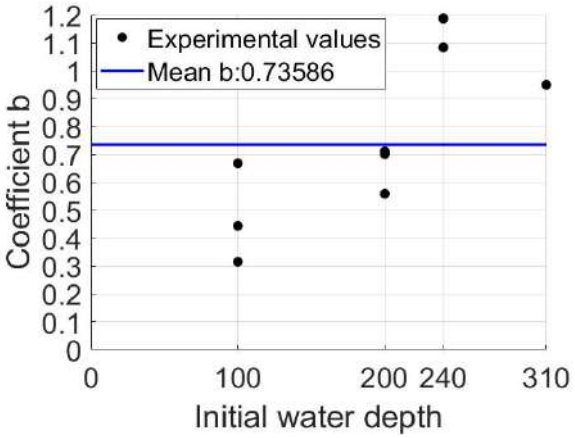

(a) Cubes, 1 pier.

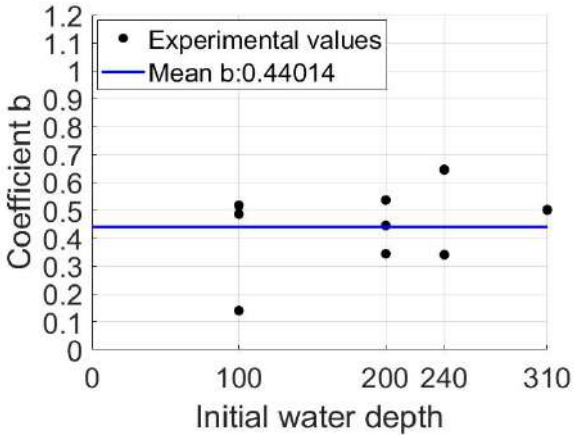

(b) Cubes, 2 piers.

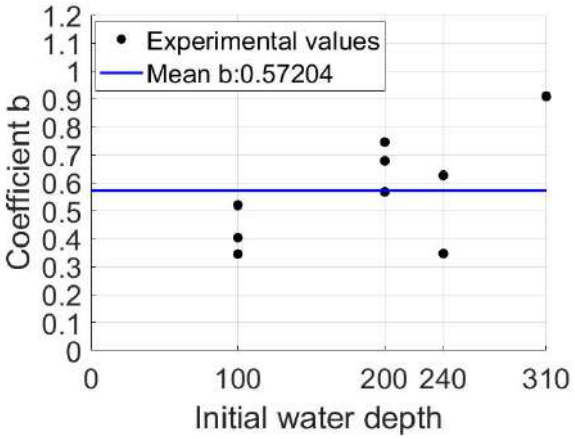

(c) Plates, 1 pier.

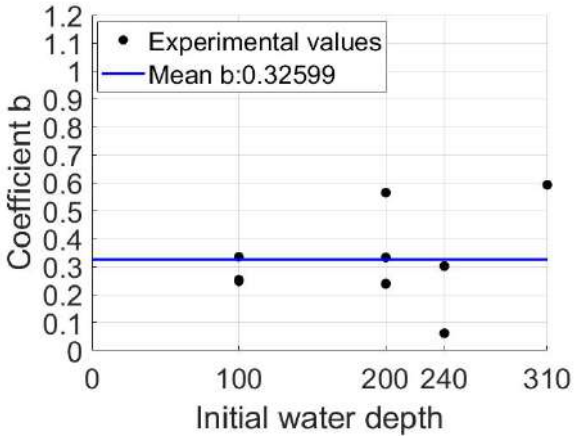

(d) Plates, 2 piers.

Figure 70: Coefficient **b** according to the initial water depth for every Fr_0.

$$b = 0.74 \quad \text{for cubes, 1 pier} \tag{24a}$$
$$b = 0.44 \quad \text{for cubes, 2 piers} \tag{24b}$$
$$b = 0.57 \quad \text{for plates, 1 pier} \tag{24c}$$
$$b = 0.33 \quad \text{for plates, 2 piers} \tag{24d}$$

11.2.5 Verification of the power laws

With equations 23 and 24, new power laws are computed. For each test, they are verified, i.e. it is checked that the laws correctly approximate the experimental data. The results of the verification are presented in the table 19. A green case means that the agreement is good (fig. 71a), an orange case stands for a rather good agreement (fig. 71b), while a red case corresponds to poor agreement (fig. 71c). The "good" or "poor" nature of the agreement between experimental data and the power law is determined on the basis of a visual analysis of the graphs. All the graphs used for comparisons can be found in the appendix D

Table 19: Agreement between power law and experimental data.

		Fr_0	0.27	0.40	0.60
		h_0 [mm]			
1 pile	Cubes	100			
		200			
		240			/
		310		/	/
	Plates	100			
		200			
		240			/
		310		/	/
2 piles	Cubes	100			
		200			
		240			/
		310		/	/
	Plates	100			
		200			
		240			/
		310		/	/

By analyzing the table 19, it seems that the fitting is good for the lowest Froude number and poor for the higher Froude numbers. This trend does not apply to the tests with 2 piers and plates, for which the agreement is globally poor.

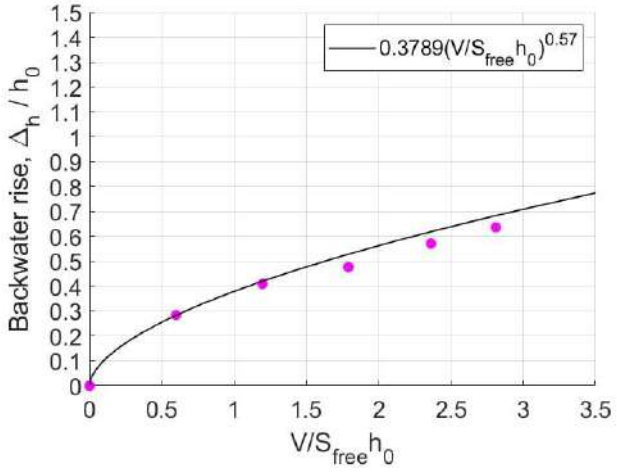

(a) $Fr_0 = 0.27$, Good agreement.

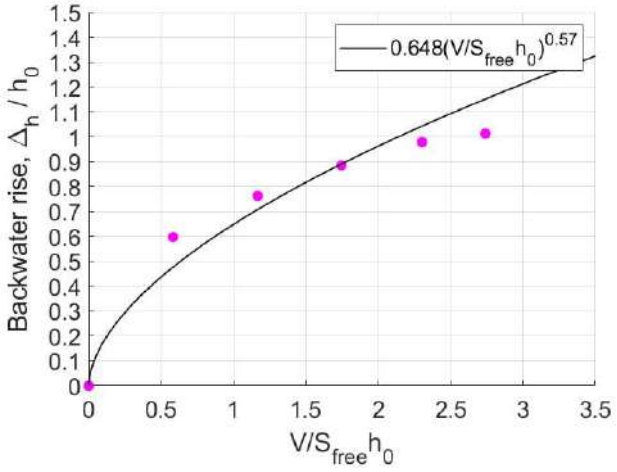

(b) $Fr_0 = 0.40$, Rather good agreement.

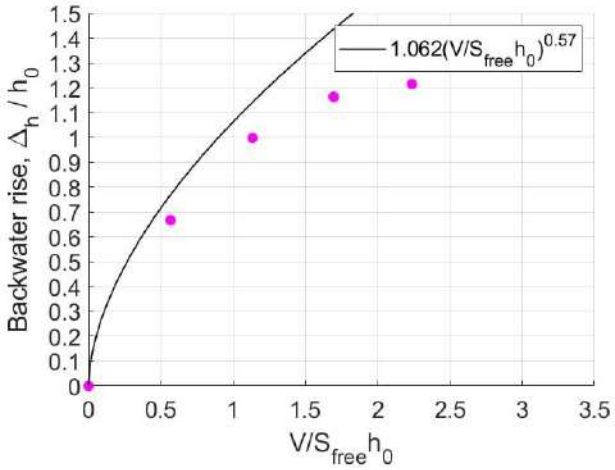

(c) $Fr_0 = 0.6$, Poor agreement.

Figure 71: Evaluation of the agreement between the power law and the experimental data, test with plates, 1 pier and $h_0 = 100mm$.

11.2.6 Characteristic volume

The procedure to compute the characteristic volume is the same as the one proposed by Schalko et al.: the characteristic volume is the volume for which the derivative of the power law falls below 10%. It corresponds to the volume responsible for the primary and main backwater rise.

Since neither coefficient **a** nor **b** depends on the initial water depth, the characteristic volume will not either.

Table 20: Characteristic volume $[dm^3]$.

	Fr_0	0.27	0.40	0.60
1 pile	Cubes	138	2254	21540
	Plates	108	386	1255
2 piles	Cubes	17	62	185
	Plates	23	53	118

For the tests for which the agreement is good or rather good, the volume computed in the table 20 is considered a good (or rather good) approximation of the actual volume responsible for the main backwater rise.

As observed above, the approximation does not seem to work for the highest Froude number. Indeed, the volumes calculated are disproportionately large (see volumes in red in the table 20). Generally speaking, it would seem that volumes considered to be correct are those that are close to the volume actually sent through the channel. This would mean that the best approximations are those for which the characteristic volume has actually been reached in the experiment, which makes sense.

11.3 Head loss approach

One idea to push further the analysis was to investigate the influence of the volume on the head loss generated by the accumulation. Instead of the backwater rise on the y-axis, a head loss coefficient is computed as follows: The head variation upstream of the bridge due to the accumulation is computed with the equation 25:

$$\Delta H = \Delta h + \frac{u^2 - u_0^2}{2g} \tag{25}$$

Because the downstream head is a constant and the head loss due to the bridge is negligible (see section 3.2.2), this variation is equivalent to the head loss due to the debris accumulation.

The Δh is known for every volume of debris and u can be computed with $\frac{Q}{Bh}$ because the section flow upstream of the bridge is the width of the flume multiplied by the water depth. Once the head losses are known for each volume, the head loss coefficient of the accumulation ξ_{acc} is calculated with equation 26:

$$\xi_{acc} = \Delta H \frac{2g}{u_0^2} \tag{26}$$

For each test, a graph of the head loss coefficient according to the dimensionless volume is obtained. The graph of the test with 1 pier, cubes in the debris mixture, an initial water depth of 100 mm and an initial Froude number of 0.27 is presented as an example (fig. 72).

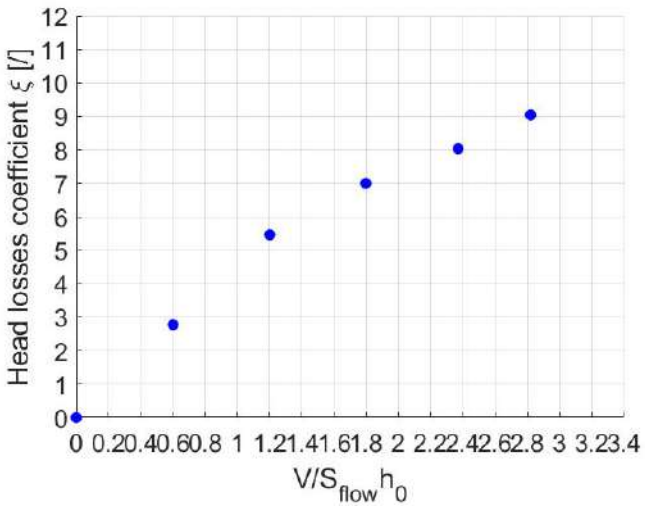

Figure 72: Head loss coefficient according to the relative volume of debris, test $C01\_1p$ (h_0 = 100mm, Fr_0=0.27, 1 pier, cubes).

For every test, a power law of the form of the equation 27 is fitted on the experimental points.

$$\xi_{acc} = a' \left(\frac{V}{S_{free} h_0} \right)^{b'} \tag{27}$$

Coefficient **a'** and **b'** are presented in the table 21.

Table 21: Fitted values of parameters **a'** and **b'** for every tests.

		Fr_0	0.27		0.40		0.60	
		h_0	a'	b'	a'	b'	a'	b'
1 pile	Cubes	100	4.93	0.58	5.51	0.40	4.18	0.70
		200	4.81	0.71	5.81	0.56	3.58	0.44
		240	6.92	1.12	5.13	1.06	/	/
		310	5.48	0.61	/	/	/	/
	Plates	100	7.67	0.55	7.23	0.35	4.23	0.35
		200	9.25	0.35	7.46	0.66	5.73	0.52
		240	8.96	0.43	6.68	0.23	/	/
		310	8.91	0.99	/	/	/	/
2 piles	Cubes	100	4.24	0.56	3.90	0.44	4.42	0.06
		200	5.12	0.08	5.70	0.36	3.78	0.27
		240	4.79	0.52	5.03	0.22	/	/
		310	5.02	0.36	/	/	/	/
	Plates	100	9.80	0.33	7.17	0.24	4.31	0.25
		200	6.88	0.48	7.12	0.13	5.08	0.31
		240	1.80	0.00	1.71	0.00	/	/
		310	6.01	0.44	/	/	/	

Some fitted lines are presented at the figure 73 for the test with 1 pier, plates and initial water depths under the deck.

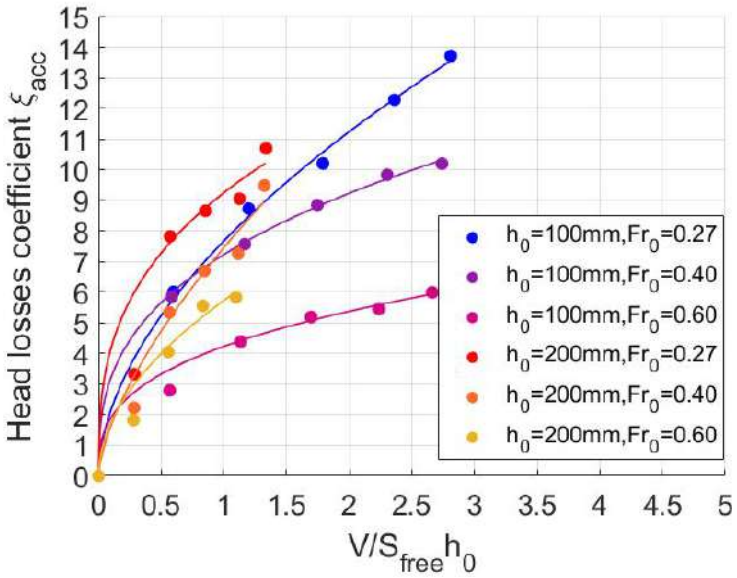

Figure 73: Fitted power law on experimental data from test with 1 pier, plates and initial water depth $h_0 = 100$ and $200mm$.

In this way, some **a'** and **b'** values are obtained for each test.
The parameters **a'** for each test are represented in the figure 74 according to the Froude number for every water depths and the **b'** parameter values for each test are represented in the figure 75 according to the initial water depth for every Froude numbers.

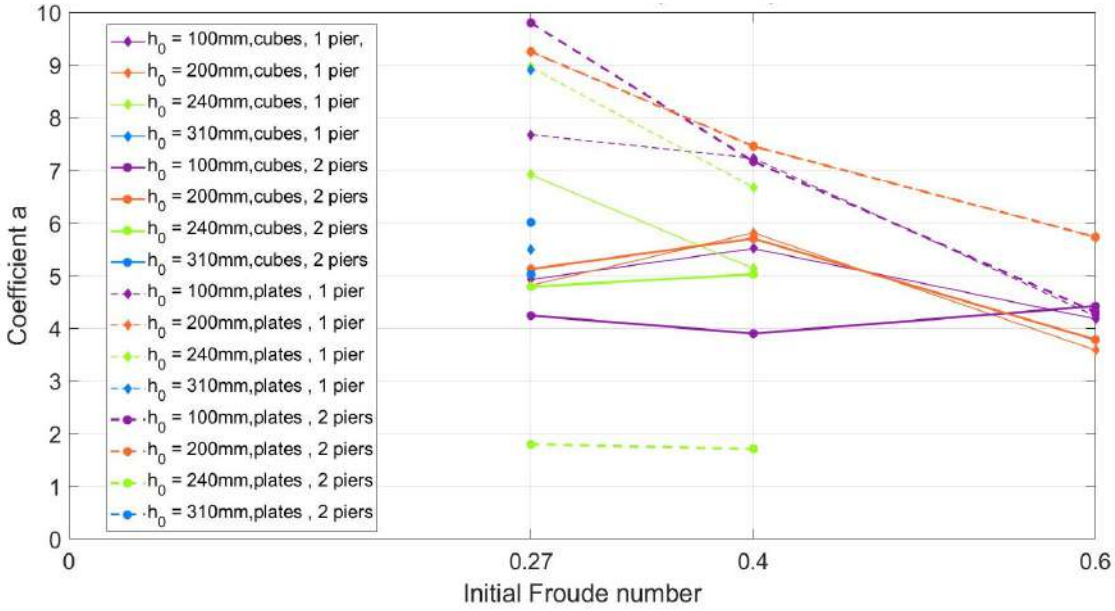

Figure 74: Coefficient **a'** according to the initial Froude number for all h_0.

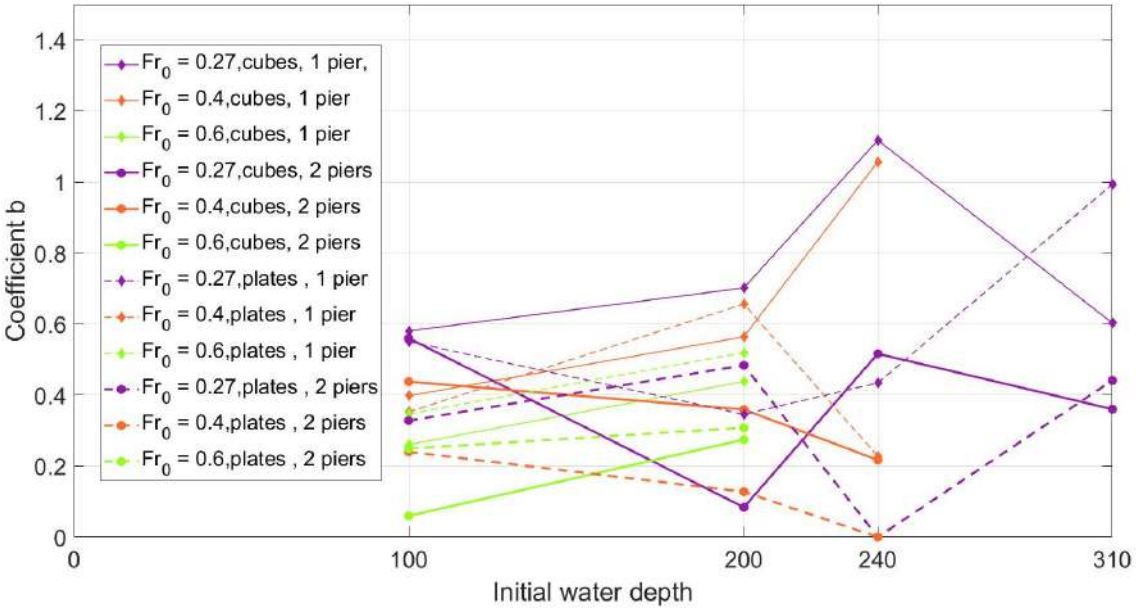

Figure 75: Coefficient **b'** according to the initial water depth for all Fr_0.

Unlike above, it's not possible to find a link between the a and b coefficients and the test parameters. Neither for **a'**, nor for **b'**, it is possible to observe a clear trend in their dependencies on the initial water depth or on the Froude number. The impact of the debris mixture and of the bridge geometry can neither be detected.

The head loss approach needs thus to be improved in order to obtain usable results.

Part V
General conclusions and perspectives

The goal of this work was to study the impact of a bridge as a blockage structure for large wood accumulation and consequently the effect on flow conditions. The influence of the bridge geometry, in particular the number of piers was included as well as the composition of the debris accumulation.

Therefore, an experimental campaign was carried out in a 1:18 scale model flume. Two bridge geometries were investigated, with the deck remaining identical and the number of piers varying from 1 to 2.
Two different mixtures of debris were studied, the first with 75% of logs and 25% of cubes, the second with 75% of logs and 25% of plates.
Initial Froude numbers from 0.2 to 0.6 and initial water depths from 100 mm to 310 mm were combined in order to define 10 different flow conditions.
With a number of repetitions for each test of between 2 and 3, no fewer than 79 tests were carried out.

The experiments have shown the following:

1. As Schmocker and Hager, 2013 had already determined, the accumulation process takes place in 2 phases. The initial debris accumulation during which the debris accumulate vertically along the pier(s) and the formation of a debris carpet, during which floating debris accumulate horizontally on the surface.

2. Water depth increases with the volume of debris accumulated at the bridge. Once a certain volume of debris is reached, the water depth barely rises at all.

3. The bridge geometry does not have a big impact on the flow conditions. Indeed, although a two pier bridge causes a longer accumulation than a one pier bridge, the effect on the backwater rise could not be distinguished between the two geometries.

4. The debris composition has a significant impact on the accumulation formation and on the backwater rise. This phenomenon was already observed in the first phase of the project. Plates generate a longer accumulation and a significantly greater backwater rise compared to cubes.

5. The initial Froude number Fr_0 of the flow has a significant effect on both the accumulation structure and the flow conditions. The larger the Froude number, the shorter the accumulation. As a result, the accumulation is more compact and blocks more water, leading to a greater backwater rise.
   Some fit equations could be derived to correlate the relative carpet length ($\frac{Lacc}{B}$) to the Froude number and the relative flow depth rise at the end of the test ($\frac{h}{h_0}$) to the Froude number (see equations 17, 19 and 20). The effect of Froude number on accumulation length differs according to initial water depth and debris mixtures, whereas the effect of Froude on water height depends very little on debris composition (if at all). Using equation 20, the final water level can be deduced from the flow conditions (h_0 and Fr_0) alone.

6. The influence of the initial water depth depends on the position of the bridge deck. For h_0 under the deck, it could be concluded that the higher water depths generate higher

backwater rise. The influence of the deck is obvious, but it would be needed to investigate more water depths, both above and below the deck, to draw more definite conclusions.

The evolution of water depth as a function of accumulation volume can be represented by a power law. To obtain laws that do not depend on the scale, the normalization proposed by Schalko et al., 2019a (21) was adapted to the present case. The coefficient **a** in these power laws could be correlated to the Froude number for each mixture, independently of h_0 and the number of piles. A constant exponent **b** was determined for each geometry and mixtures, independently of the h_0. From these laws, characteristic volumes, responsible for the primary backwater rise, can be deduced. For each Froude, bridge geometry and debris composition, a characteristic volume was determined independently of the water level (see tab. 20).

A "head loss" approach was initiated. Power laws were fitted on the experimental data for each test, but unlike those based on water level, the coefficients of the power laws could not be correlated with the test conditions. For the future, it therefore seems reasonable to retain the approach based on the water height or to investigate head losses in another way.

To take this work a step further, the points of attention should be the influence of the initial water depth, taking deck height into account, and a more systematic determination of characteristic volumes.

For the first point, at least 3 water depths under and over the deck should be tested in order to determine if the eventual dependency is linear or not. For the water depth over the bridge, the volume of batches should be adapted. Indeed, when the water is too far over the deck, the accumulation is impossible to initiate if the volume of debris is too small. Larger volume should be used, at least for the first batches.

For the second point, the characteristic volumes that were determined are only reasonable for certain configurations. Investigating in this way to determine more reliable values for characteristic volumes and then an increase in the maximum water level is essential to understand the most important effects an accumulation could have on flow conditions.

In the next phase of the EMfloodResilience project, more flow conditions will be tested, as well as a wider variety of bridge geometries. This will enable to validate the correlations established, and extend their range of applications.

To conclude, this approach based on experimental results in order to establish scale-independent correlations will contribute to better understand and quantify the observed phenomenon. Eventually, new bridge design, less prone to debris accumulation, may be defined in order to reduce the impact of extreme flood.

List of symbols

a	bulk factor
a and a'	coefficient of power law
b and b'	exponent of power law
B or B_r	flume width
C_v	sediment concentration
D	log diameter
d_L or D_L	log diameter
d_{Lm}	mean log diameter
d_m	mean grain size
d_p	pier diameter
D_R	pole diameter (in racks)
f_A	accumulation type factor
F_A	Froude number with large wood accumulation
FM	organic fine material
F_r or F	Froude number
Fr_0 or F_0	initial Froude number
g	gravitational acceleration
h	water depth
H	head
H	(Schmocker and Hager, 2013) bridge deck
h_0	initial water depth
h_A	large wood accumulation height
h_b	(Schalko et al., 2019b) movable bed height;
h_b	opening height of the bridge
H_R	rack height
J	hydraulic gradient
J_0	bottom slope;
K_s	Strickler's coefficient
L_A or L_{acc}	Accumulation length
L_b	movable bed length;
L_c	large wood carpet length
L_L or L	log length
L_S	scour length
LW_A	large wood accumulation factor
LW_p	normalized LW accumulation parameter
N	number of logs (Wang)
p or P_L	blockage probability
P_{LM}	maximum blockage probability
Q	discharge
Q_0	approach flow discharge
R or R_h	hydraulic radius
R^2	coefficient of determination
s	relative sediment density
S_r	scour depth at retention rack

u	(Schalko et al., 2018) flow diversion factor;
u	velocity of the flow
v	velocity of the flow
v_0 or u_0	initial velocity of the flow
v_A	flow velocity in the accumulation
V_c	Characteristic volume
V_d	total volume of logs (Wang)
V_l	loose large wood volume
V_s	solid large wood volume
w_b	opening width of the bridge
w_p or w_{pb}	pier width
ΔH	Head variation or loss
Δh	backwater rise
$\Delta h/h_0$	relative backwater rise
Δh_c	characteristic backwater rise
η	backwater rise ratio
θ_{IC}	bed shear stress of initial condition
λ	scale factor
λ	(Schmocker 2013) log parameter
ξ	head loss coefficient
ρ_d	LW density
ρ_f	density of the debris flow
σ_g	geometric standard deviation of the grain size distribution;

Abbreviations

LW	large wood
UDS	ultrasonic distance sensor

List of Figures

Bibliography

Bezzola, G. R., & Hegg, C. (2007). Ereignisanalyse hochwasser 2005, teil 1 - prozesse, schäden und erste einordnung. *Umwelt-Wissen*, *707*, 215.

Braudrick, C. A., Grant, G. E., Ishikawa, Y., & Ikeda, H. (1997). Dynamics of wood transport in streams; a flume experiment. *Earth surface processes and landforms*, *22*(7), 669–683. https://doi.org/10.1002/(SICI)1096-9837(199707)22:7<669::AID-ESP740>3.0.CO;2-L

Davidson, S., MacKenzie, L., & Eaton, B. (2015). Large wood transport and jam formation in a series of flume experiments. *Water Resources Research*, *51*(12), 10065–10077. https://doi.org/https://doi.org/10.1002/2015WR017446

Follett, E., Schalko, I., & Nepf, H. (2020). Momentum and energy predict the backwater rise generated by a large wood jam. *Geophysical research letters*, *47*(17). https://doi.org/https://doi.org/10.1029/2020GL089346

Gschnitzer, T., Gems, B., Aufleger, M., Mazzorana, B., & Comiti, F. (2014). On the evaluation and modelling of wood clogging processes in flood related hazards estimation. In *Engineering geology for society and territory – volume 3* (pp. 139–142). Springer International Publishing. https://doi.org/https://doi.org/10.1007/978-3-319-09054-2_27

Keller, E. A., & Swanson, F. J. (1979). Effects of large organic material on channel form and fluvial processes. *Earth Surf. Process. Landforms*, *4*(4), 361–380. https://doi.org/https://doi.org/10.1002/esp.3290040406

Rickli, C., & Hess, J. (2009). Aspects de la formation des bois flottants. *Cours de formation continue KHOS. Fribourg, Switzerland: Kommission für Hochwasserschutz KHOS*.

Ruiz-Villanueva, V., Wyzga, B., Zawiejska, J., Hajdukiewicz, M., & Stoffel, M. (2016). Factors controlling large wood transport in a mountain river. *Geomorphology (Amsterdam, Netherlands)*, *272*, 21–31. https://doi.org/https://doi.org/10.1016/j.geomorph.2015.04.004

Schalko, I., Lageder, C., Schmocker, L., Weitbrecht, V., & Boes, R. M. (2019a). Laboratory flume experiments on the formation of spanwise large wood accumulations; part I, effect on backwater rise. *Water resources research*, *55*(6), 4854–4870. https://doi.org/https://doi.org/10.1029/2018WR024649

Schalko, I., Lageder, C., Schmocker, L., Weitbrecht, V., & Boes, R. M. (2019b). Laboratory flume experiments on the formation of spanwise large wood accumulations; part II, effect on local scour. *Water resources research*, *55*(6), 4871–4885. https://doi.org/https://doi.org/10.1029/2019WR024789

Schalko, I., Schmocker, L., Weitbrecht, V., & Boes, R. M. (2018). Backwater rise due to large wood accumulations. *Journal of hydraulic engineering (New York, N.Y.)*, *144*(9). https://doi.org/https://doi.org/10.1061/(ASCE)HY.1943-7900.0001501

Schalko, I., Schmocker, L., Weitbrecht, V., & Boes, R. M. (2020). Laboratory study on wood accumulation probability at bridge piers. *Journal of Hydraulic Research*, *58*(4), 566–581. https://doi.org/https://doi.org/10.1080/00221686.2019.1625820

Schalko, I. (2020). Wood retention at inclined racks: Effects on flow and local bedload processes. *Earth Surface Processes and Landforms*, *45*(9), 2036–2047. https://doi.org/https://doi.org/10.1002/esp.4864

Schmocker, L., & Hager, W. (2011). Probability of drift blockage at bridge decks. *Journal of hydraulic engineering (New York, N.Y.)*, *137*(4), 470–479. https://doi.org/https://doi.org/10.1061/(ASCE)HY.1943-7900.0000319

Schmocker, L., & Hager, W. H. (2013). Scale modeling of wooden debris accumulation at a debris rack. *Journal of Hydraulic Engineering*, *139*(8), 827–836.

Wang, D., Wang, X., Chen, X., Lian, B., Wang, J., & Wang, F. (2022). Laboratory flume experiments on the characteristics of large wood accumulations from debris flow and the backwater rise at slit-check dams. *Landslides*, *19*(9), 2135–2148.

Wyss, A., Schalko, I., & Weitbrecht, V. (2021). Field study on wood accumulation at a bridge pier. *Water (Basel)*, *13*(18), 2475–. https://doi.org/https://doi.org/10.3390/w13182475

Appendix

A Database

A.1 Database parameters

Location										
Type of structure	Year of construction		River	Municipality	Structure / street name	EPSG	X reg	Y reg	Lat	Long
	[YYYY]	comments							[° ' " N]	[° ' " E]

Location		
Curvilinear abscissa	River bed altitude	Upstream river shape
[m]	[m]	

Structure										
Opening(s) shape	Width	Length	Slope	Angle	Thickness	Altitude on the bridge	Form open section	Abutments	Nb of piers	Pier width
	[m]	[m]	[%]	°	[m]	[m]			[#]	[m]

Structure										
Distance between piers	Min distance	Max distance	Pier shape	Pier protrusion	Id photo bridge	Handrail material	Handrail height	Handrail porosity	Id photo handrail	Structure damage
[m]	[m]	[m]		[m]			[m]	[%]		

Flood event at the structure					
Flood event	Type of flow	Discharge	Altitude max water level	Max water depth	Flow width
		[m³/s]	[m]	[m]	[m]

Deposit										
Clogging	Carpet	Total	Total width	Total height	Carpet	Carpet	Carpet	Volume	Location at structure	Id photo deposit
	y/n	[m]	[m]	[m]	[m]	[m]	[m]	[m³]		

Main debris contents						
Main trunk presence	Id main Type 1	Volume percentage 1	Id main Type 2	Volume percentage 2	Id main Type 3	Volume percentage 3
		[%]		[%]		[%]

A.2 Geometric parameters

Id	River bed altitude	Width	Length	Thickness	Altitude on the bridge	opening height	Nb of piers	Pier width	Distance between piers	Min distance	Max distance	distance of interest	Pier shape
[#]	[m]	[m]	[m]	[m]	[m]	[m]	[#]	[m]	[m]	[m]	[m]	[m]	
30052	79,9	8,2	40	0,70	83,94	3,34	0	No pier	40	40	40	40,0	No pier
30065	273,88	12	30	1,15	276,4	1,37	0	No pier	30	30	30	30,0	No pier
30074	260	15,7	21,6	1,40	264,56	3,16	0	No pier	21.6	21,6	21,6	21.6	No pier
30075	76,7	10	37	0,9	81,89	4,29	0	No pier	37		No pier	37,0	
30052	141,93	4,26	24,21	0,65	146,67	4,09	1	1,5	11.31-11,41	11,31	11,41	11,4	Round nosed
30028	124,06	10,7	28,9	1,05	129,4	4,29	1	1	13.1-14.05	13,1	14,05	13,6	Round nosed
30076	103,93	10,2	30,35	1,50	110,23	4,80	1	1	14.7-14.65	14,65	14,7	14,7	Round nosed
30082	103,33	10,2	38,3	1,40	109,32	4,59	1	1,1	19.15-19.15	19,15	19,15	19,2	Sharp nosed
30088	184,53	15	26	1,55	189,37	3,29	1	1	12	12	12	12,0	Round nosed
30092	102,03	10,2	30,6	1,63	107,38	3,72	1	1	14,8-14,8	14,8	14,8	14,8	Round nosed
30093	88,56	4,58	32,15	1,30	94,22	4,36	1	1,41	13.92-14.32	13,92	14,32	14,1	Round nosed
30112	78,21	17,4	32	1,25	83,7	4,24	1	1	15-15	15	15	15,0	Sharp nosed
30092	71,83	5,67	35	1,06	77	4,11	1	0,8	12.52-12.42	12,42	12,52	12,5	Square nosed
30093	64,62	17	41	1,80	69,68	3,26	1	0,8	20-20	20	20	20,0	Round nosed
30097	137,65	10	22	1,35	142,37	3,37	1	1,5	9.3-9.45	9,3	9,45	9,4	Round nosed
30112	177,75	3,5	20	1,3	182,32	3,27	1		9,5			9,5	Round nosed
30120	163,2	6,5	23,1	0,85	168,49	4,44	1		10,7			10,7	Sharp nosed
30121	198,3	3	26	0,70	202,05	3,05	2	0,8	6.5-9.5-6.5	6,5	9,5	9,5	Circular
30030	168,28	10,1	33,09	1,50	174,02	4,24	2	0,75	11.12-10.45-11.52	10,45	11,52	10,5	Round nosed
30039	140,4	14,5	29,36	1,50	145,3	3,40	2	1,2	9.45-7.76-9.15	7,76	9,45	7,8	Round nosed
30041	138,65	3,97	24,85	0,50	143,35	4,20	2	1,2	7.6-7.05-7.8	7,05	7,8	7,1	Round nosed
30044	131,12	11,83	27,43	1,00	135,22	3,10	2	1,1	8.94-7.75-8.55	7,75	8,94	7,8	Round nosed
30046	130,37	12	28,55	1,45	135,5	3,68	2	1,4	8.8-8.2-8.75	8,2	8,8	8,2	Round nosed
30061	128,95	4,84	28,4	0,65	133,74	4,14	2		7,17			7,2	Round nosed

B Geometry

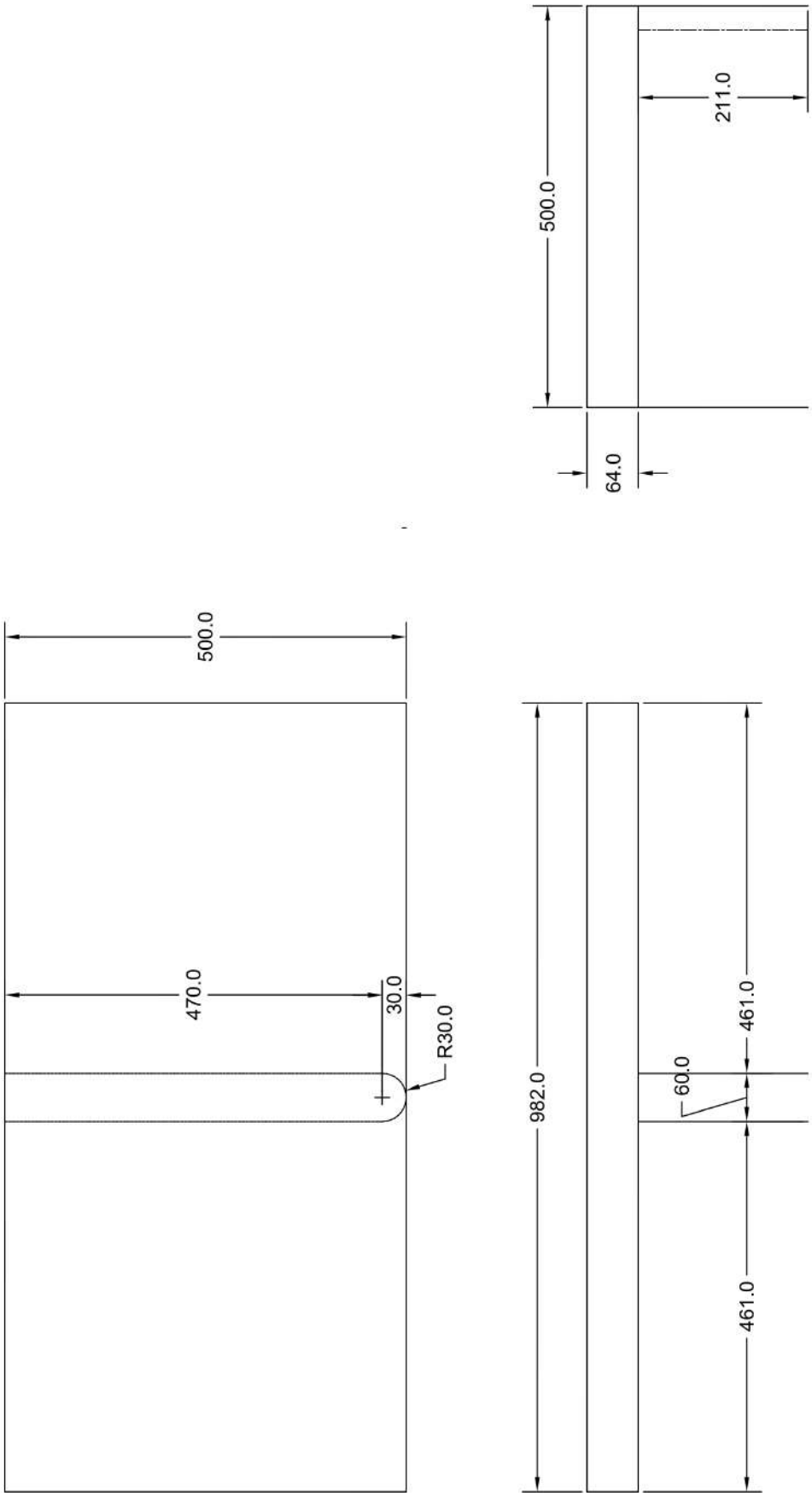

C User's manual of the vnp-35/IU/TC ultrasonic sensor from Microsonic

microsonic

Instruction manual

vnp-Ultrasonic Sensors with one analogue output

vnp-25/IU/TC
vnp-35/IU/TC
vnp-130/IU/TC
vnp-340/IU/TC
vnp-600/IU/TC

Product description

- The vnp-sensor with one analogue output measures the distance to an object within the detection zone contactless. A signal proportional to distance is created according to the adjusted window margings of the analogue characteristic curve.
- The actual window margings arise from a virtual origin set with the Teach-in procedure and offsets that are set numericaly using two push-buttons and a three-digit LED-display (TouchControl). As an additional feature the virtual origin can be shifted contineously by connecting the control input line »Sync/Com« at pin 5 of the sensor connector to $+U_B$.
- Light emitting diodes (three-colour LEDs) indicate all operation conditions.
- Choosing between rising and falling output characteristic is possible.
- Useful additional functions are set in the Add-on-menu.
- The measured distance value can be displayed relatively in relation to the virtual origin (see Add-on-menu).
- Using the LinkControl adapter (optional accessory) all TouchControl and additional sensor parameter settings may be made by a Windows-Software.

Important instructions for assembly and application

All employee and plant safety-relevant measures must be taken prior to assembly, start-up, or maintenance work (see operation manual for the entire plant and the operator instruction of the plant).

The sensors are not considered as safety equipment and may not be used to ensure human or machine safety!

The vnp-sensors indicate a **blind zone**, in which the distance cannot be measured. The **operating range** indicates the distance of the sensor that can be applied with normal reflectors with sufficient function reserve. When using good reflectors, such as a calm water surface, the sensor can also be used up to its **maximum range**. Objects that strongly absorb (e.g. plastic foam) or diffusely reflect sound (e.g. pebble stones) can also reduce the defined operating range.

Synchronisation

If the assembly distances shown in Fig.1 for two or more sensors are exceeded the integrated synchronisation should be used. Connect Sync/Com-channels (pin 5 at the units receptable) of all sensors (10 maximum).

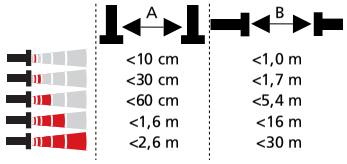

Fig. 1: Assembly distances, indicating synchronisation/multiplex

Multiplex mode

The Add-on-menu allows to assign an individual address »01« to »10« to each sensor connected via the »Sync/Com« line (Pin5). The sensors perform the ultrasonic measurement sequentially from low to high address. Therefore any influence between the sensors is rejected.
The address »00« is reserved to synchronisation mode and deactivates the multiplex mode. (To use synchronised mode all sensors must be set to address »00«.)

Assembly instructions

☞ Assemble the sensor at the installation location.
☞ Plug in the connector cable to the M 12 connector.

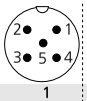

		colour
1	$+U_B$	brown
3	$-U_B$	blue
4	-	black
2	I/U	white
5	Sync/Com.	grey

Fig. 2: Pin assignment with view onto sensor plug and colour coding of the microsonic connection cable

Start-up

vnp-sensors are delivered factory made with the following settings:

- Rising analogue characteristic
- Offsets at 10 cm
- Measurement range set to maximum range

Set the parameters of the sensor manually to adjust the relative window margins (offsets).

- The offsets can be programmed in the range of ± 99 cm around the teachable origin.
- For offsets less than 10 cm the programmable resolution is 1 mm.

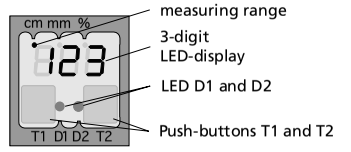

Fig. 3: TouchControl

Operation

By connecting the control input line »Sync/Com« at pin 5 for 3 seconds to + U_B the virtual origin is set to the actually measured distance. This has to be done in normal operation mode.
vnp-sensors work maintenance free. Small amounts of dirt on the surface do not influence function. Thick layers of dirt and caked-on dirt affect sensor function and therefore must be removed.

Note

- vnp-sensors have internal temperature compensation. Because the sensors heat up on their own, the temperature compensation reaches its optimum working point after approx. 30 minutes of operation.
- If an object is within the set window margins of the analogue output, then LED D1 lights up green, if the object is outside the window margins, then LED D1 lights up red.
- The load put to the analogue output is detected automatically when turning supply voltage on.
- During normal mode operation, the measured distance value is displayed on the LED-indicator in mm (up to 999 mm) or cm (from 100 cm). Scale switches automatically and is indicated by a point on top of the digits. Alternatively a percentage scale may be set in the add-on menu. In this connection 0% and 100% correspond to the set window margins of the analogue output.
- If no objects are placed within the detection zone the LED-indicator shows »- - -«.
- If no push-buttons are pressed for 20 seconds during parameter setting mode the made changes are stored and the sensor returns to normal mode operation.
- You can lock the key pad to provide inputs, see »Key lock and factory setting«.
- You can reset the factory settings at any time, see »Key lock and factory setting«.

Show parameters

Tapping push-button T1 shortly during normal mode operation shows »PAr« on the LED-display. Each time you tap push-button T1 the actual settings of the analogue output are shown.

Set the offsets to origin numerically using LED-display....

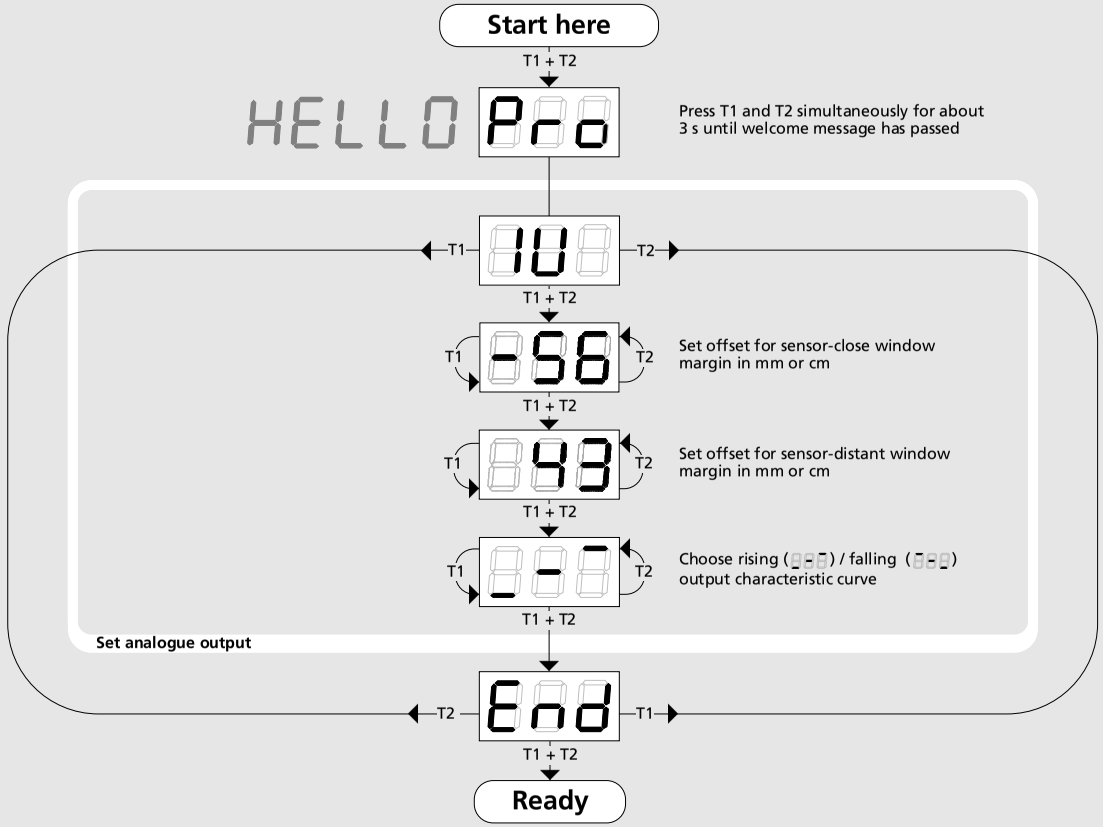

CE 89/336/EEC

...then adjust origin with the Teach-in procedure

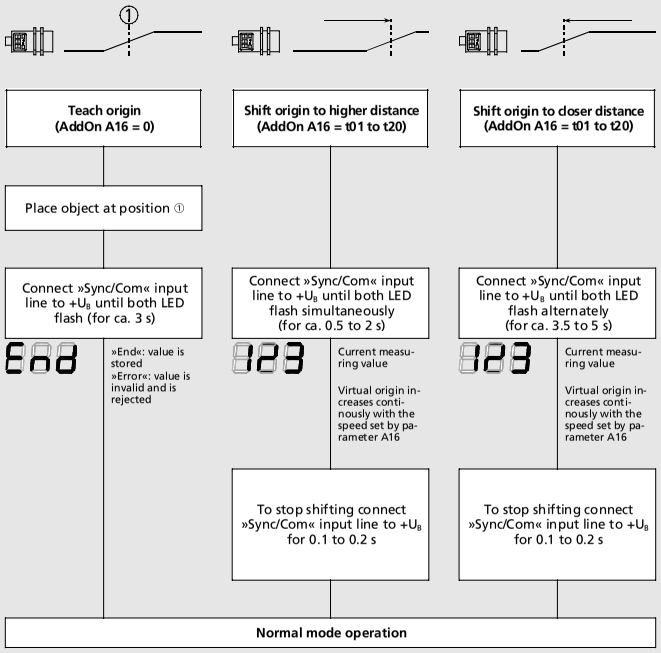

Example for numerically set offsets and teached origin

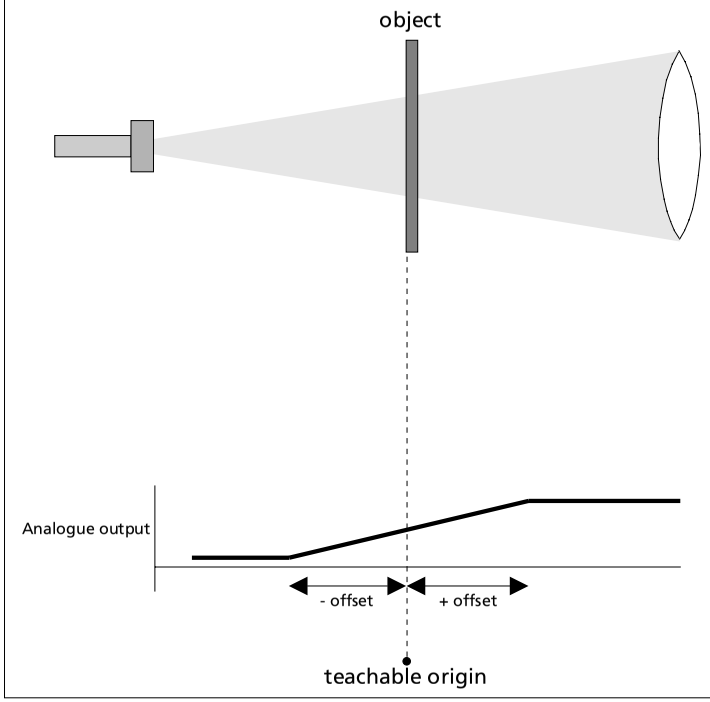

Display mode, key lock and factory setting

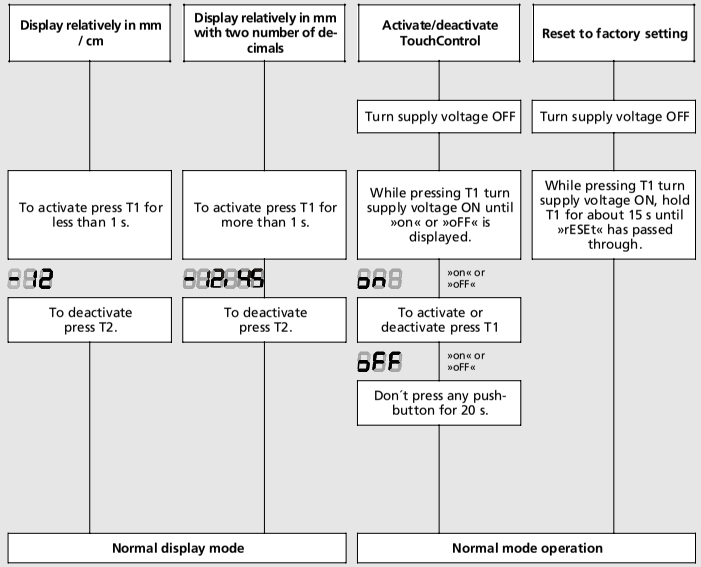

Usefull additional functions in Add-on menu (for experienced users only, settings not required for standard applications)

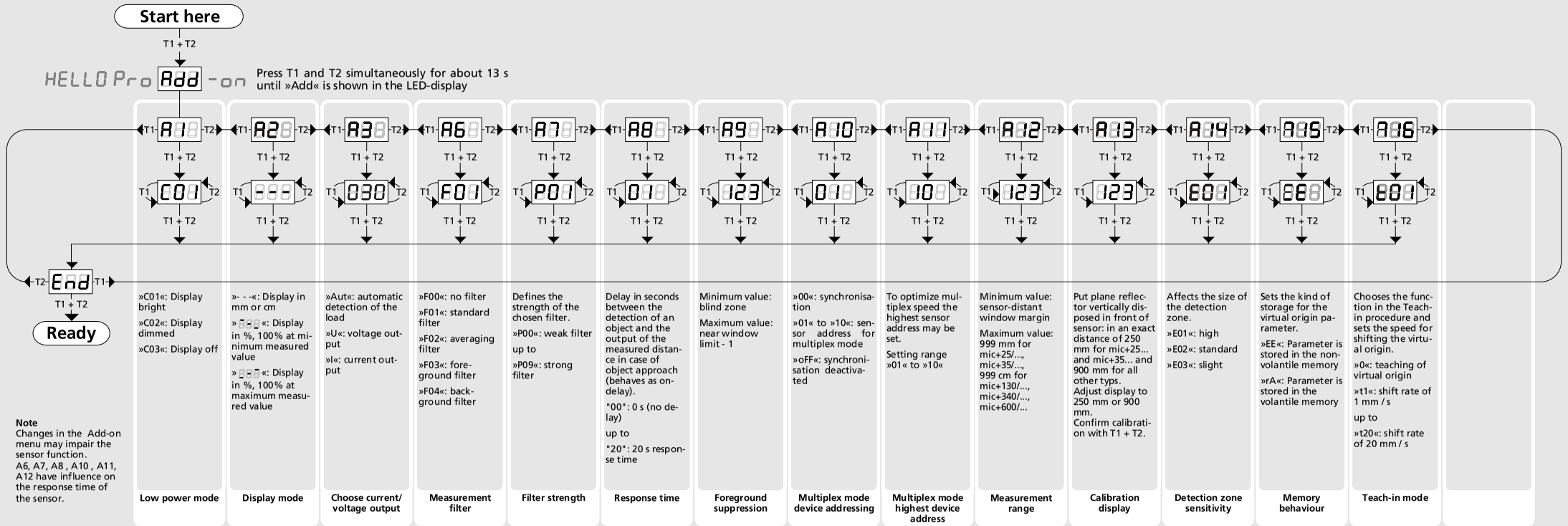

Note
Changes in the Add-on menu may impair the sensor function.
A6, A7, A8 , A10 , A11, A12 have influence on the response time of the sensor.

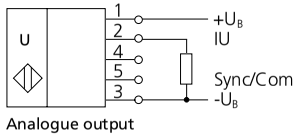

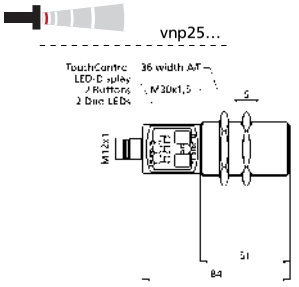

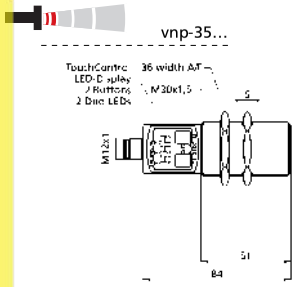

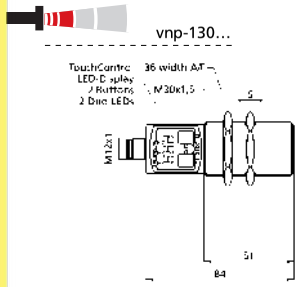

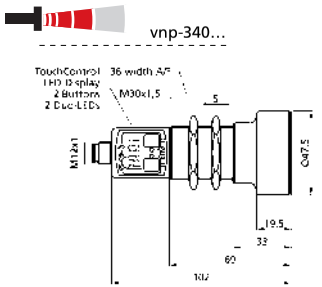

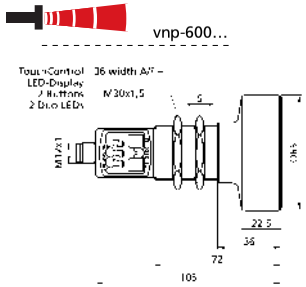

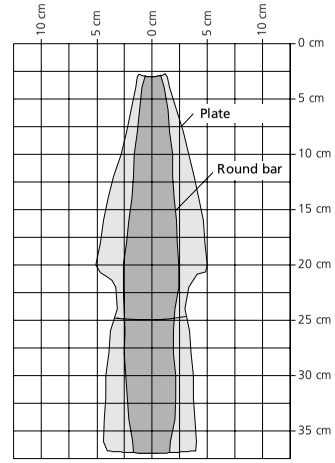

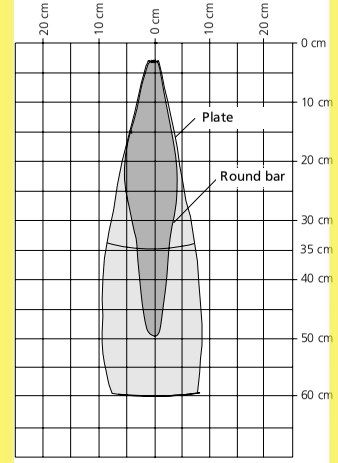

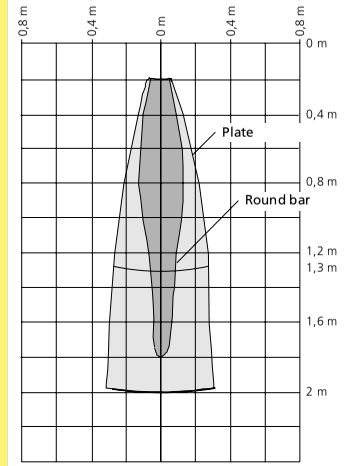

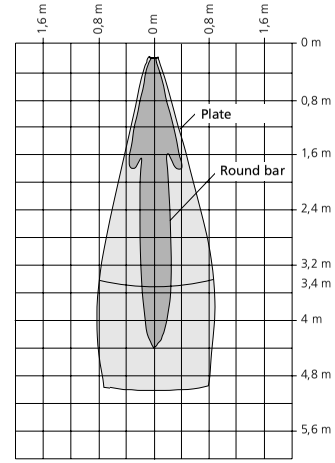

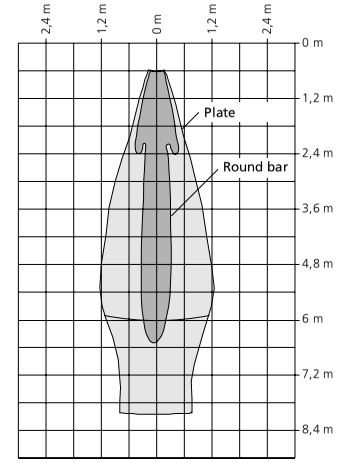

Technical data

Analogue output

	vnp25…	vnp-35…	vnp-130…	vnp-340…	vnp-600…
Blind zone	0 to 30 mm	0 to 65 mm	0 to 200 mm	0 to 350 mm	0 to 600 mm
Operating range	250 mm	350 mm	1.300 mm	3.400 mm	6.000 mm
Maximum range	350 mm	600 mm	2.000 mm	5.000 mm	8.000 mm
Angle of beam spread	Please see detection zone	Please see detection zone	Please see detection zone	Please see detection zone	Please see detection zone
Transducer frequency	ca. 320 kHz	ca. 400 kHz	ca. 200 kHz	ca. 120 kHz	ca. 80 kHz
Resolution, sampling rate	0,18 mm	0,18 mm	0,18 mm	0,18 mm	0,18 mm
Reproducibility	± 0,15 %	± 0,15 %	± 0,15 %	± 0,15 %	± 0,15 %
Accuracy	Temperature drift internal compensated, ≤ 2 % may be deactivated[1] (0,17%/K without compensation)	Temperature drift internal compensated, ≤ 2 % may be deactivated[1] (0,17%/K without compensation)	Temperature drift internal compensated, ≤ 2 % may be deactivated[1] (0,17%/K without compensation)	Temperature drift internal compensated, ≤ 2 % may be deactivated[1] (0,17%/K without compensation)	Temperature drift internal compensated, ≤ 2 % may be deactivated[1] (0,17%/K without compensation)
Detection zones for different objects: The dark grey areas are determind with a thin round bar (10 or 27 mm dia.) and indicate the typical operating range of a sensor. In order to obtain the light grey areas, a plate (500 x 500 mm) is introduced into the beam spread from the side. In doing so, the optimum angle between plate and sensor is always employed. This therefore indicates the maximum detection zone of the sensor. It is not possible to evaluate ultrasonic reflections outside this area.					
Opperating voltage U_B	9 V to 30 V DC, reverse polarity protection	9 V to 30 V DC, reverse polarity protection	9 V to 30 V DC, reverse polarity protection	9 V to 30 V DC, reverse polarity protection	9 V to 30 V DC, reverse polarity protection
Voltage ripple	±10 %	±10 %	±10 %	±10 %	±10 %
No-load supply current	≤ 80 mA	≤ 80 mA	≤ 80 mA	≤ 80 mA	≤ 80 mA
Housing	Brass sleeve, nickel-plated, plastic parts: PBT, TPU; Ultrasonic transducer: polyurethane foam, epoxy resin with glass content	Brass sleeve, nickel-plated, plastic parts: PBT, TPU; Ultrasonic transducer: polyurethane foam, epoxy resin with glass content	Brass sleeve, nickel-plated, plastic parts: PBT, TPU; Ultrasonic transducer: polyurethane foam, epoxy resin with glass content	Brass sleeve, nickel-plated, plastic parts: PBT, TPU; Ultrasonic transducer: polyurethane foam, epoxy resin with glass content	Brass sleeve, nickel-plated, plastic parts: PBT, TPU; Ultrasonic transducer: polyurethane foam, epoxy resin with glass content
Class of protection to EN 60529	IP 67	IP 67	IP 67	IP 67	IP 67
Norm conformity	EN 60947-5-2	EN 60947-5-2	EN 60947-5-2	EN 60947-5-2	EN 60947-5-2
Type of connection	5-pin initiator plug, PBT	5-pin initiator plug, PBT	5-pin initiator plug, PBT	5-pin initiator plug, PBT	5-pin initiator plug, PBT
Controls	2 push-buttons (TouchControl)	2 push-buttons (TouchControl)	2 push-buttons (TouchControl)	2 push-buttons (TouchControl)	2 push-buttons (TouchControl)
Indicators	3-digit LED-display, 2 three-colour LEDs	3-digit LED-display, 2 three-colour LEDs	3-digit LED-display, 2 three-colour LEDs	3-digit LED-display, 2 three-colour LEDs	3-digit LED-display, 2 three-colour LEDs
Programmable	Yes, with TouchControl and LinkControl	Yes, with TouchControl and LinkControl	Yes, with TouchControl and LinkControl	Yes, with TouchControl and LinkControl	Yes, with TouchControl and LinkControl
Operating temperature	-25°C to +70°C	-25°C bis +70°C	-25°C bis +70°C	-25°C bis +70°C	-25°C bis +70°C
Storage temperature	-40°C to +85°C	-40°C bis +85°C	-40°C bis +85°C	-40°C bis +85°C	-40°C bis +85°C
Weight	150 g	150 g	150 g	210 g	270 g
Response time[1]	50 ms	70 ms	110 ms	180 ms	240 ms
Time delay before availibility	< 300 ms	< 300 ms	< 300 ms	< 300 ms	< 300 ms
Order No.	**vnp-25/IU/TC**	**vnp-35/IU/TC**	**vnp-130/IU/TC**	**vnp-340/IU/TC**	**vnp-600/IU/TC**
Current output 4 – 20 mA	$R_L \leq 100\ \Omega$ at $9V \leq U_B \leq 20V$; $R_L \leq 500\ \Omega$ at $U_B \geq 20V$ Rising/falling output characteristic	$R_L \leq 100\ \Omega$ at $9V \leq U_B \leq 20V$; $R_L \leq 500\ \Omega$ at $U_B \geq 20V$ Rising/falling output characteristic	$R_L \leq 100\ \Omega$ at $9V \leq U_B \leq 20V$; $R_L \leq 500\ \Omega$ at $U_B \geq 20V$ Rising/falling output characteristic	$R_L \leq 100\ \Omega$ at $9V \leq U_B \leq 20V$; $R_L \leq 500\ \Omega$ at $U_B \geq 20V$ Rising/falling output characteristic	$R_L \leq 100\ \Omega$ at $9V \leq U_B \leq 20V$; $R_L \leq 500\ \Omega$ at $U_B \geq 20V$ Rising/falling output characteristic
Voltage output 0 – 10 V	$R_L \geq 100\ k\Omega$ at $U_B \geq 15$ V, short-circuit-proof Rising/falling output characteristic	$R_L \geq 100\ k\Omega$ at $U_B \geq 15$ V, short-circuit-proof Rising/falling output characteristic	$R_L \geq 100\ k\Omega$ at $U_B \geq 15$ V, short-circuit-proof Rising/falling output characteristic	$R_L \geq 100\ k\Omega$ at $U_B \geq 15$ V, short-circuit-proof Rising/falling output characteristic	$R_L \geq 100\ k\Omega$ at $U_B \geq 15$ V, short-circuit-proof Rising/falling output characteristic

---

[1] Can be programmed with TouchControl and LinkControl

D Verification of the approximation of power law

The figures are named with the code of the test (see tab. 15)

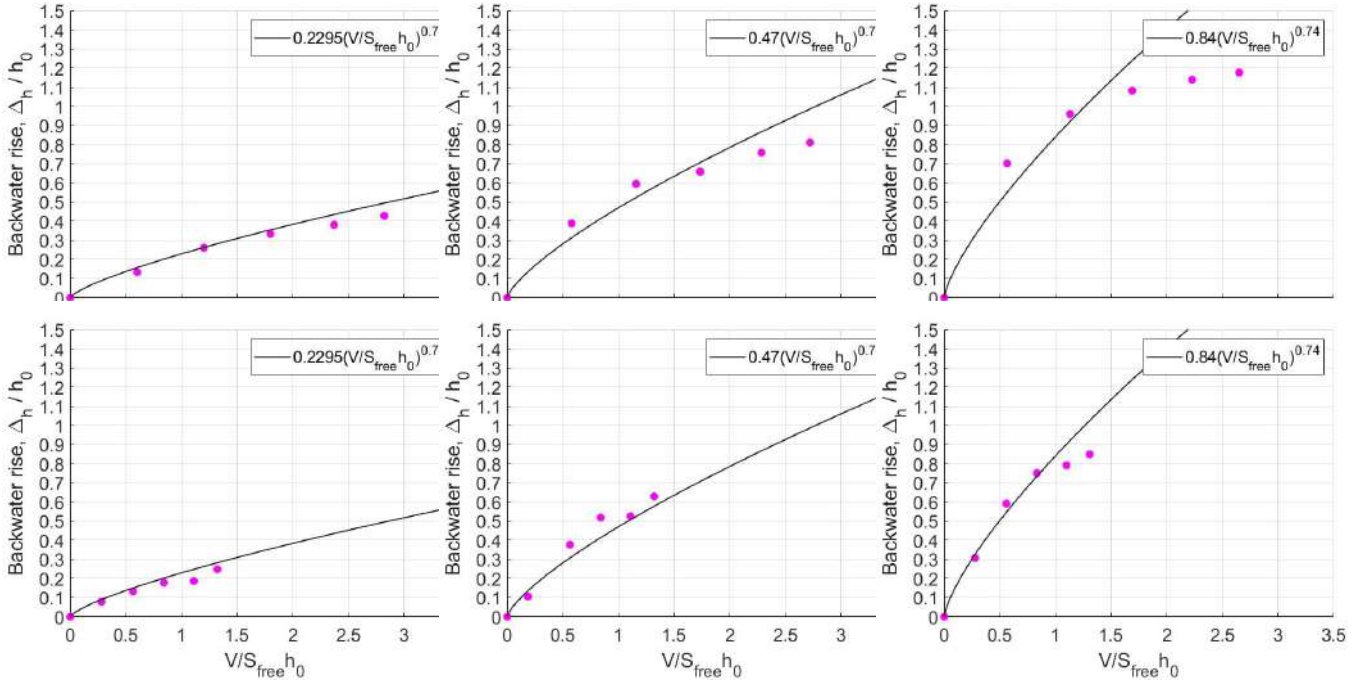

(d) $C04\_1p$ (e) $C05\_1p$ (f) $C06\_1p$

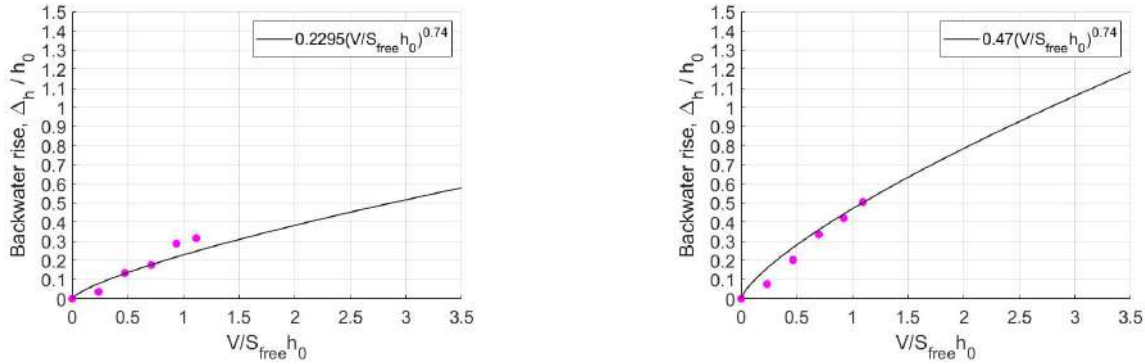

(g) $C07\_1p$ (h) $C08\_1p$

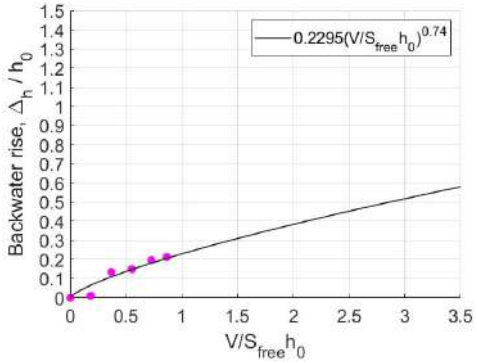

(i) $C09\_1p$

Figure 76: Comparison of the approximation of the power law with the experimental data, test with cubes, 1 pier

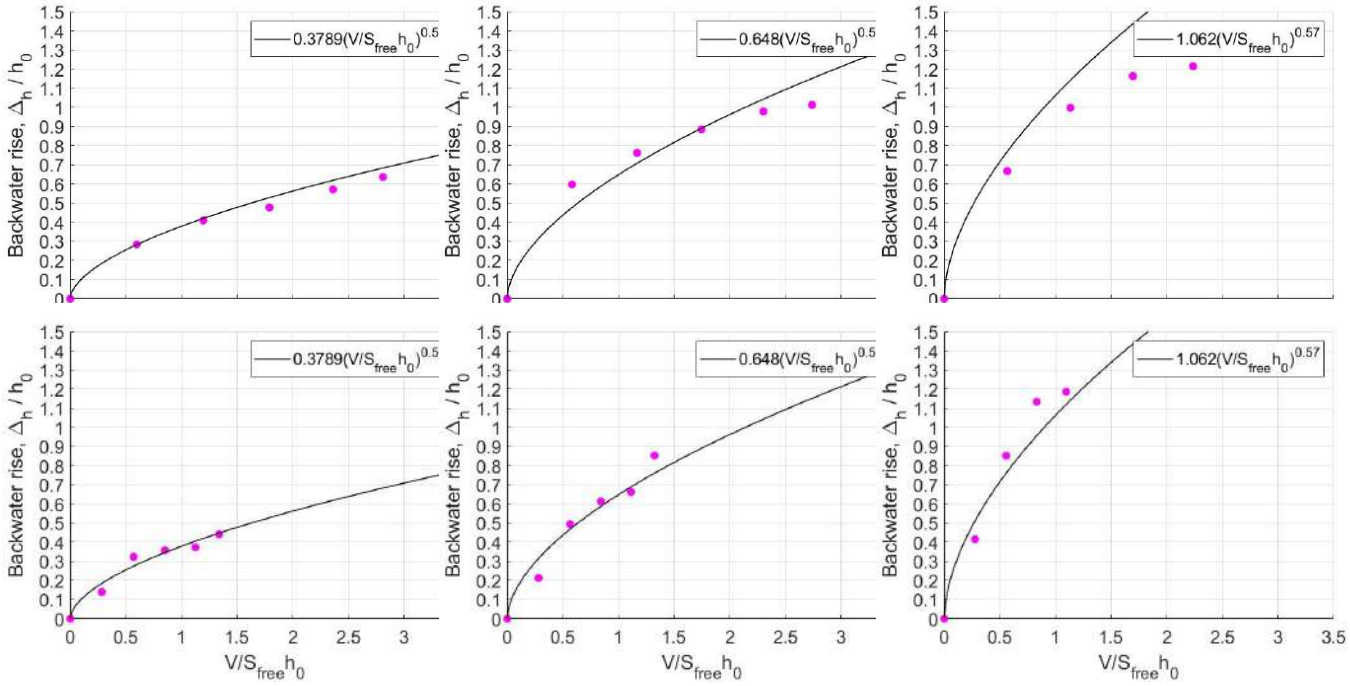

(d) $P04\_1p$ (e) $P05\_1p$ (f) $P06\_1p$

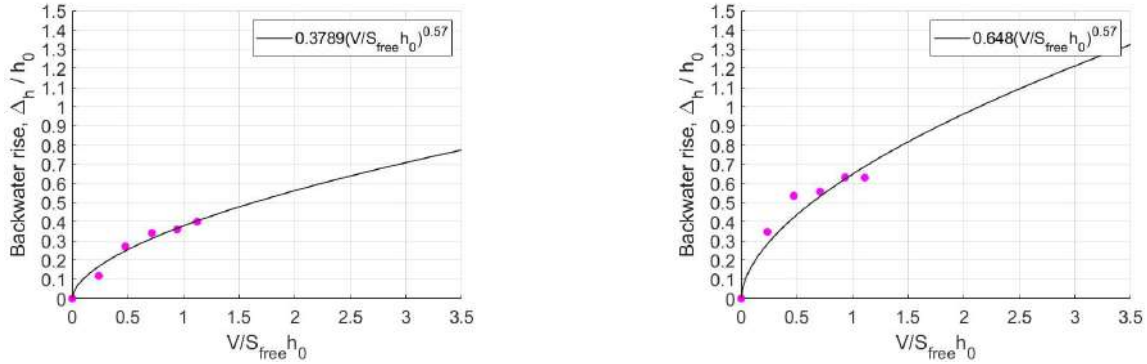

(g) $P07\_1p$ (h) $P08\_1p$

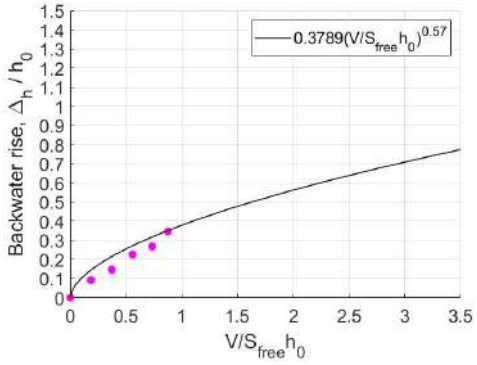

(i) $P09\_1p$

Figure 77: Comparison of the approximation of the power law with the experimental data, test with plates, 1 pier

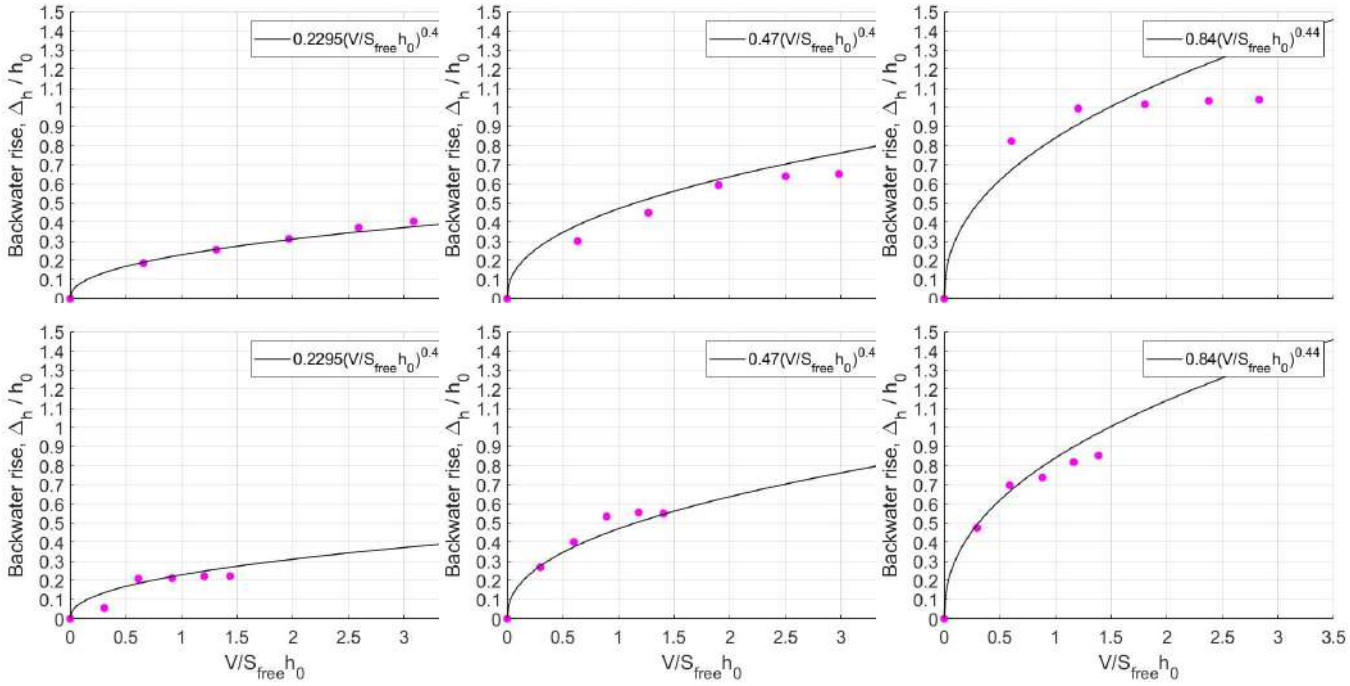

(d) $C04\_2p$ (e) $C05\_2p$ (f) $C06\_2p$

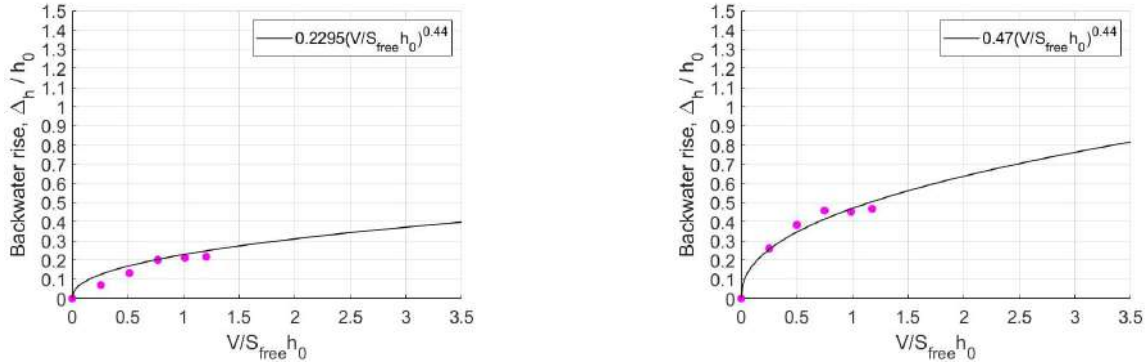

(g) $C07\_2p$ (h) $C08\_2p$

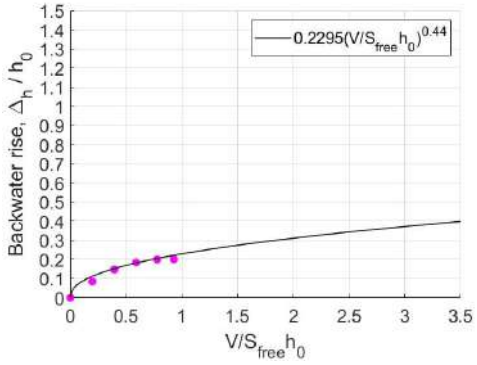

(i) $C09\_2p$

Figure 78: Comparison of the approximation of the power law with the experimental data, test with cubes, 1 pier

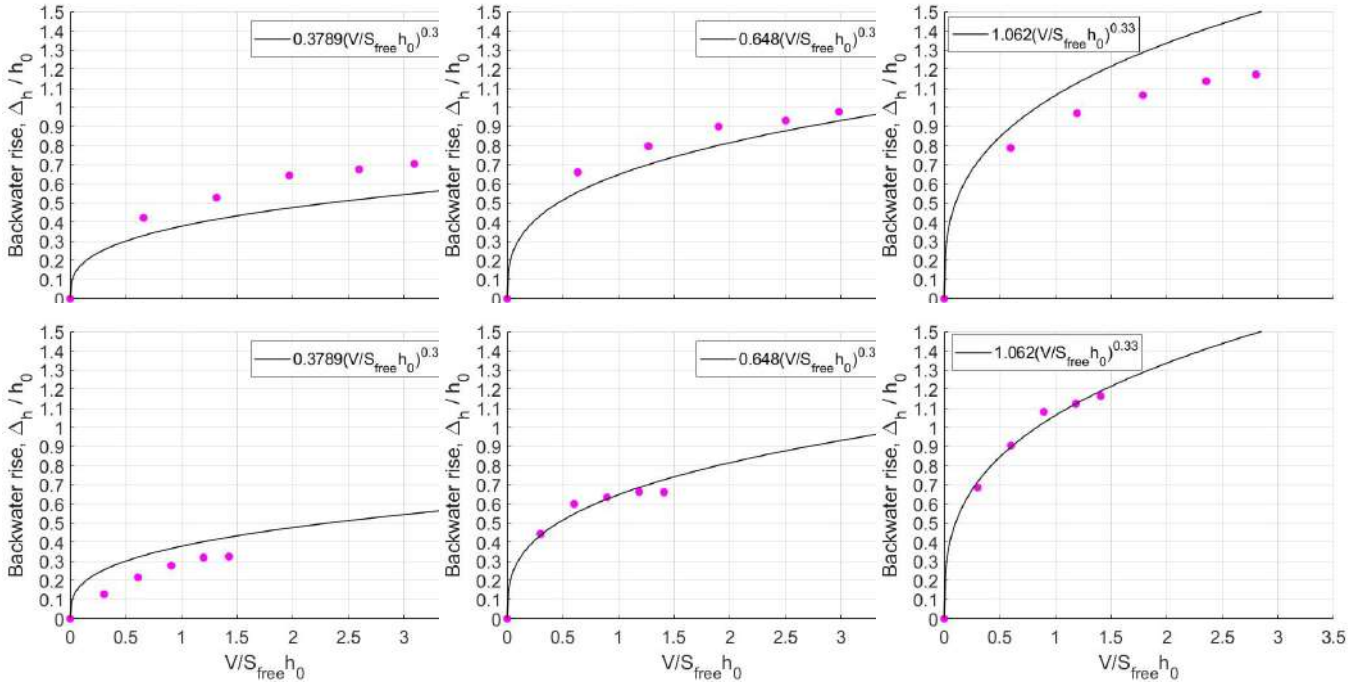

(d) $P04\_2p$ (e) $P05\_2p$ (f) $P06\_2p$

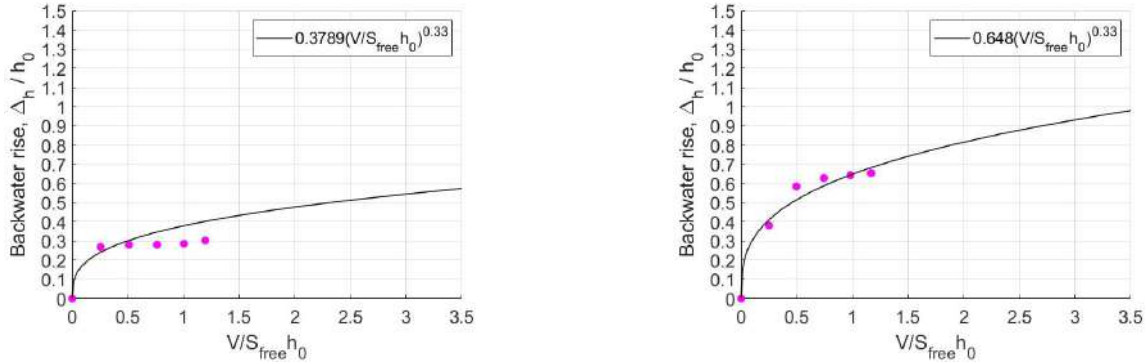

(g) $P07\_2p$ (h) $P08\_2p$

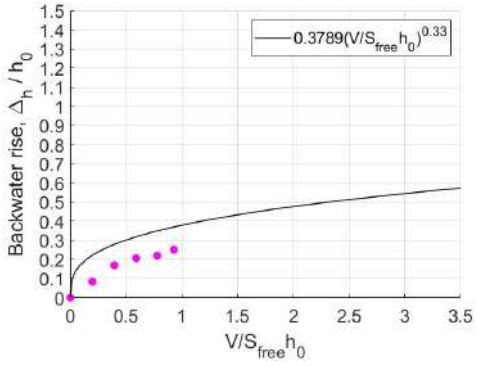

(i) $P09\_2p$

Figure 79: Comparison of the approximation of the power law with the experimental data, test with plates, 1 pier